School of Earth and Planetary Sciences

Experimental Alteration in Composite Mineral Systems: Mg-silicates, Fe-Ni-sulphides and Fe-Ti-oxides

Tobias Wengorsch

This thesis is presented for the Degree of

Doctor of Philosophy

of

Curtin University

September 2019

DECLARATION

To the best of my knowledge and belief this thesis contains no material previously published by any other person except where due acknowledgment has been made. This thesis contains no material which has been accepted for the award of any other degree or diploma in any university.

Perth, 27th September 2019

Tobias Wengorsch

Date

ABSTRACT

The importance of fluids in geochemical re-equilibration has been emphasized in many recent studies as an alternative process to solid state diffusion. Many chemical and petrographic features have been identified supporting this mechanism, yet exact reaction pathways and the controls of interaction between solid and fluid component are still poorly understood. This PhD research contributes new insight into the control of fluid driven replacement reactions with the emphasis on composite systems.

Serpentinisation of ultramafic rocks is an important process affecting the physical properties of the oceanic lithosphere on a large scale. Depending on prevailing conditions different serpentine minerals are observed, such as chrysotile and lizardite at low temperature and antigorite at high temperature, for most chemical environments. However, little is known about the influence of the reacting fluid composition on these phases. Hydrothermal experiments were performed on powders of natural harzburgite, single crystal San Carlos olivine and enstatite, with controlled grain size at 240°C and fluid saturated conditions. A systematic relation between fluid salinity and secondary serpentine morphology was observed. In addition, serpentine morphology changed with the proportion of olivine to orthopyroxene in the starting material. Olivine serpentinisation in pure H_2O resulted in the formation of lizardite with a transition into conical serpentine together with brucite. The presence of additional orthopyroxene prevented brucite formation and stabilized polyhedral serpentine together with tabular lizardite. With increasing fluid salinity the serpentine assemblage evolved from polyhedral serpentine + lizardite to lizardite, to lizardite + chrysotile fibres, to serpentine tubes, and finally to cones and fibres. Polyhedral serpentine was only observed in experiments with non-saline solutions, whereas highly saline solutions promoted the transient appearance of proto-serpentine within the first 330 hours of reaction. Reaction progress of olivine serpentinisation was increased ~16 fold in the presence of pyroxene compared to pure olivine at fixed time and reacting fluid composition. Subsequent experiments on monomineralic San Carlos olivine with aqueous Si and/or NaCl in solution led to the conclusion that the

increase in serpentinisation rate of olivine is due to the release of Si from enstatite to solution, which is dependent on fluid salinity.

Ultramafic rocks in Archean greenstone belts are important host rocks for Fe-Ni-sulphide deposits. These deposits often show extensive alteration through fluids after their magmatic emplacement. The hydrothermal alteration of the host rock has important implications for the minerals of economic interest, especially for low grade deposits, in which strongly varying high Ni tenor assemblages can be found. Although the exact mechanism is controversial, hydrothermal alteration is generally accepted as a cause. Hydrothermal experiments were conducted on primary magmatic assemblages of San Carlos olivine, harzburgite and sulphide powders in batch reactors at 240 °C with high pH fluids containing sodium chloride. An additional experiment was conducted under O_2 free conditions. The experimental sulphide assemblages were upgraded in Ni-tenor through the replacement of pyrrhotite by magnetite, by the transformation of pentlandite to millerite and heazlewoodite, and by increasing Ni-contents in residual pentlandite. In addition the produced sulphide textures resemble those found in nature perfectly. The product sulphide assemblages were dependent on redox conditions of fO_2, bulk composition of the sulphide fraction and the ratio between silicates and sulphides in the starting materials.

Ilmenite represents the most important host mineral for titanium, due to its large deposits associated with magmatic intrusions or placer deposits. The alteration of ilmenite has implications for both natural processes like weathering at earth surface conditions or alteration within the earth's crust and industrial applications. This makes ilmenite a well-suited system to investigate fluid rock interactions. Batch reactor experiments of ilmenite cubes with pre-existing hematite exsolution lamellae were conducted in acidic solutions at 150 °C to study its effect on the reaction mechanism. Formation of secondary rutile and the development of a coarse network of porosity through the volume of the cube was observed which was aided by the preceding selective dissolution of hematite. In contrast to reported results from the literature, the development of hierarchical fractures was not observed for experiments on ilmenite

in the presence of pre-existing hematite lamellae. This is expected to have major implications for rock mechanical properties as the alteration of ilmenite with hematite lamellae only affects the margin of the cubes, whereas the alteration of pure ilmenite develops a large network of fractures at low acid concentrations.

The mineral systems studied in this PhD research display the complexity of fluid driven replacement reactions which are especially important at low temperatures. Reactions with distinct fluid compositions can produce unique alteration textures which are closely coupled to the spatial distribution and composition of phases within the system. This has also important implications for reaction kinetics as concurrently reacting minerals within a system can influence each other, which highlights the importance of a comprehensive approach to understand the complex history of metamorphic/metasomatic rocks in nature.

ACKNOWLEDGMENTS

First I want to thank Andrew Putnis for this great opportunity to work in Australia on this PhD project and for fun entertaining evenings, together with Andreas Beinlich, I want to thank them for their resilience in guidance and support during the last three years. I especially want to thank Andreas for all the time he invested in me as well as for teaching me new skills such as Matlab. Also I want to thank Ben Grguric, for the extensive amount of sample material provided and evenings of discussion and insight shared. Thanks to Katy Evans who always had an open ear. Håkon Austrheim, Oliver Plümper and Helen King for the helpful discussions. I would also like to thank the staff at the Centre for Microscopy, Characterisation and Analysis, Alexandra Suvorova, Malcolm Roberts and Andrew Johnson for all their help and assistance, and especially Sarah Gain for the countless hours on the FIB-SEM. Also, I want to thank Shaun Height for all the advice and the opportunity to earn some extra money. I want to thank my family for all the support provided at a distance. Many thanks to Lars and Franziska Crede who provided me with accommodation in the first weeks of my PhD and for the great time we had together. Also, thanks to all the new friends who made this a great experience, especially Tania, Alex, Bryant, Janne, Simon and Anna.

But most importantly I want to thank my fiancée Michelle for the many exciting weekend adventures during our time in Western Australia. I am truly grateful for all her love and encouragement during these three challenging years and for her sacrifice to put her own plans and join me on this exciting path.

LIST OF PUBLICATIONS INCLUDED

This thesis compiles a collection of research papers (manuscripts) that are in preparation at the time of submission of this thesis. The individual chapters are put in context to each other in the introductory chapter. The following are the research paper comprising this thesis.

Paper 1 – Wengorsch, T., Beinlich, A., Grguric, B., Putnis, A. (2019 submitted). Fluid compositional control on serpentinisation kinetics and textural evolution.

Paper 2 – Wengorsch, T., Beinlich, A., Grguric, B., Putnis, A. (2019 in preparation). Experimental Ni-tenor modification of Fe-Ni-sulphides through hydrothermal alteration.

Paper 3 – Wengorsch, T., Beinlich, A., Grguric, B., Putnis, A. (2019 in preparation). Effect of hematite on the textural evolution during the replacement of ilmenite by rutile.

TABLE OF CONTENTS

LIST OF FIGURES

THESIS AIM

The aim of this PhD research is to provide new insight into the complex reaction pathways occurring during fluid rock interactions in systems comprised of multiple phases. This study focusses on an experimental approach in order to mimic conditions prevailing during alteration in natural systems and investigate the occurring reactions. A range of different analytical methods are employed, such as light microscopy, FESEM + EDS, Raman spectroscopy and EPMA complimented by ICP-MS, TGA and FIB tomography. This study describes three mineral systems and the effect of fluid and solid composition on the alteration texture and morphology, reaction extent and mineral assemblage.

Chapter 1

Introduction

1.1 Introduction

The chemical reactions between solid and fluid phases are of great importance in geologic systems, with implications that range from weathering at surface conditions to the formation of hydrothermal ore deposits. However, although the presence of H_2O in metamorphic rocks is easily recognised by the presence of hydrous phases, its importance for the mechanisms of chemical re-equilibration in response to changes in P, T, X -conditions is less well understood. Thermodynamic calculations can be used to calculate the stable assemblage, it is generally assumed that systems adjust to the imposed conditions and reach equilibrium on geological timescales. This approach is commonly used to decipher the metamorphic history of rocks. For many years, solid state diffusion was thought to be the main mechanism controlling these re-equilibration processes. Diffusion is effective at high temperatures, but many studies have highlighted discrepancies between observations and diffusion-based predictions of reactions at lower temperatures where a fluid phase is involved. Alternative models have been proposed to explain the re-equilibration of systems that include a fluid phase (Putnis, 2002; Putnis, 2009; Putnis and Putnis, 2007). When a fluid comes into contact with a solid that it is not in equilibrium with, it will dissolve, and an interfacial fluid that contains elevated concentrations of the elements previously hosted by the phase will form. If any phase is supersaturated in the interfacial fluid then it will precipitate onto the parent phase. This model is called the ‘coupled dissolution reprecipitation reaction’ (CDR) model (Fig. 1.1). The following features are characteristic of CDR (Putnis, 2002; Putnis, 2009; Putnis and Putnis, 2007; Ruiz-Agudo et al., 2014).

I. The absence of a diffusion profile in the host mineral and a sharp boundary on the nm-scale between the unreacted and secondary mineral.
II. Porosity development within the secondary phase, which provides access for the fluid phase to the reaction front, thus maintaining progress of the reaction.

III. Spatially close coupling between dissolution and precipitation, leading to pseudomorphic textures.

IV. Preservation of crystallographic orientation if there is an epitaxial relationship between the primary and secondary minerals.

Similarities in the crystal structures of the dissolving and precipitating mineral can favour metastable mineral pairs, such as violarite after pentlandite (Tenailleau et al., 2006; Xia et al., 2009). Pseudomorphism is characterised by the preservation of the shape of the parent mineral, and produces replacement textures that are common in nature. Proponents of the CDR model have proposed that this texture reflects a spatially close coupling between dissolution and precipitation (e.g. Putnis and Putnis, 2007). Recent studies have contributed further to our understanding of the mechanisms that control these textures (Altree-Williams et al., 2015). Xia et al. (2009) reported that reactions in which dissolution is rate limiting, produce nanoscale pseudomorphic replacement between the host and secondary minerals. In contrast, reactions in which the precipitation is rate-limiting produce a gap between parent mineral and precipitate and are spatially decoupled. The preservation of the primary texture requires the precipitating mineral to occupy the same volume as its host; otherwise material would have to be added or removed, with consequences for the generation of porosity (Putnis, 2009). This aspect of replacement reactions has attracted much attention because it bears important implications for geological systems; mass preserving replacement can lead to volume increase and reaction-induced fracturing and the generation of new reactive surface area (Farough et al., 2016; Jamtveit and Hammer, 2012; Jamtveit et al., 2008; Jamtveit et al., 2009; Malvoisin et al., 2017). A prominent example of a volume-increasing reaction is the serpentinisation of olivine, which incorporates up to ~13 wt% H_2O from the reacting fluid which leads to a stark difference in average densities of olivine and serpentinite, ~3.3 g/cm^3 vs. ~2.6 g/cm^3 (e.g. Sleep et al., 2004).

The serpentinisation reaction can be expressed as mass preserving, which involves a volume increase due to the addition of H_2O, whereas a volume conserving reaction

would require large amount of material to be transported away from the site of reaction, which would require a considerably amount of fluid. However, the exact mechanism is still of debate (e.g. Andreani et al., 2007; O'Hanley, 1992), and much evidence exists supporting volume expansion as well as mass transfer (e.g Iyer et al., 2008).

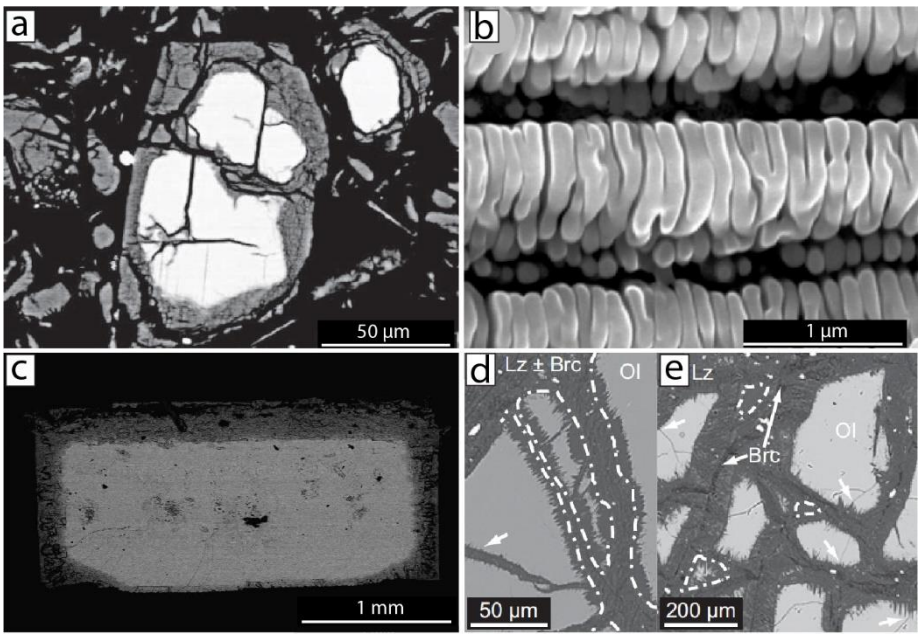

Figure 1.1: Examples of coupled dissolution reprecipitation reactions in experimental and natural samples. (a) Cross-section of leucite crystal (bright) partially replaced by analcime (grey), with obvious fracture generation, modified after Putnis 2009. (b) Scanning electron image of analcime as the reaction product of leucite alteration, exhibiting fine lamallae and porosity, modified after Xia 2009. (c) Partial replacement of KBr (grey) by porous K(Br,Cl) (dark grey). (d + e) Replacement of olivine by mesh texture lizardite and brucite, with olivine exhibiting etch pits (arrows), modified after Pluemper 2012.

The development of an interfacial fluid at the reaction interface in response to initial mineral dissolution is a critical step in the initiation of replacement reactions (Putnis, 2009; Putnis and Ruiz-Agudo, 2013). However, it is not possible to quantify the composition of this fluid directly in standard experimental setups, because the composition of the interfacial fluid is different to that of the bulk solution. An exception is provided by the work of Putnis et al. (2005), who used in-situ phase-shift interferometry to reveal a steep compositional gradient at the surface of a KBr crystal reacting with a KCl solution. Furthermore, Geisler et al. (2019) were able to measure

the fluid pH in-situ of the interfacial fluid during the alteration of glass indirectly using Raman spectroscopy.

Replacement via the CDR mechanism is proposed to be more efficient within low temperature systems (Ruiz-Agudo et al., 2014), but several studies have documented complex reaction textures that record competition/interaction between fluid-driven replacement and solid state diffusion processes at higher temperatures (Zhao et al., 2014; Zhao et al., 2013; Zhao and Pring, 2019).

Porosity generation is an important aspect of fluid-driven replacement reactions, because it facilitates contact between the fluid phase and the reaction front and is required for reactions to progress. Putnis et al. (2007) noted that porosity can still be generated, even when the molar volume of the precipitating phase is larger than that of the phase it replaces. Putnis (2009) further emphasised that the relative solubilities of the host and product provide a greater control on porosity generation than the absolute solubilities.

The CDR model is able to explain a wide range of chemical textures and reactions in environments that include surface weathering and low temperature hydrothermal alteration (e.g. Hellmann et al., 2012), and has important implications for material science applications (e.g. Lenting et al., 2018; Xia et al., 2008). Coupled dissolution reprecipitation reactions have been described in many fluid–rock systems and textures previously attributed to other processes have been reinterpreted as the products of CDR in recent years. For example, the replacement of albite ($NaAlSi_3O_8$) by sanidine ($KAlSi_3O_8$) in experiments, or by anorthite ($CaAl_2Si_2O_8$) in natural rocks, highlights the importance of this reaction mechanism; it can alter major rock forming minerals and thus potentially affect large volumes of rock. These feldspar replacement reactions exhibit many features characteristic of CDR, including sharp interfaces, the absence of a diffusion profile, and porosity generation (e.g. Cole et al., 2004; Labotka et al., 2004; Mora et al., 2009; Niedermeier et al., 2009). Other examples include the replacement of leucite ($KAlSi_2O_6$) by analcime ($NaAlSi_2O_6{\cdot}H_2O$), single crystal KBr by KCl, and chlorapatite ($Ca_{10}(PO_4)_6Cl_2$) by hydroxyapatite ($Ca_{10}(PO_4)_6(OH)_2$) (Fig.

1.1 a to c). These are only a few of the many examples from nature and experimental work reviewed by Putnis (2009); Ruiz-Agudo et al. (2014). The following paragraphs give an overview of replacement reactions and their geologic relevance in the mineral systems appropriate for the scope of this thesis.

1.1.1 Mg-Silicates

The alteration of an ultramafic rock, containing olivine (Ol) and orthopyroxene (Opx) as its major components, in the presence of an aqueous fluid phase is known as serpentinisation. It is a major process of volatile exchange between the earth's hydro- and lithosphere, resulting in large-scale changes to the physical properties of rocks and the formation of distinctive geochemical environments. This reaction occurs over a wide range of temperatures, and produces different serpentine minerals ($Mg_3Si_2O_5(OH)_4$), e.g. antigorite at high temperature vs. chrysotile and lizardite at low temperatures (e.g. Evans, 2004) (Fig. 1.2).

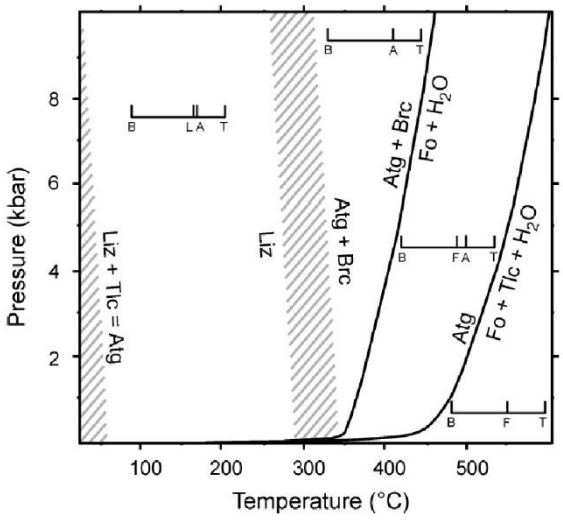

Figure 1.2: A possible stable phase diagram for the system MgO-SiO_2-H_2O. Dashed lines indicate uncertainty of the H2O conserving reaction, from Evans 2004.

Serpentinisation has consequences for many fields of geological research, e.g. magnetic properties, crustal recycling, environments of early life, carbon sequestration, and H_2 generation, so this reaction has received much attention in recent years (e.g. Bach et al., 2006; Evans, 2010; Frost and Beard, 2007; Klein et al., 2013;

Mayhew et al., 2013; Oufi et al., 2002; Plümper et al., 2014; Power et al., 2013; Russell and Hall, 1997; Sleep et al., 2004). The driving force of this reaction is the presence of a fluid phase that initiates dissolution and subsequent precipitation. The thermodynamics of the $MgO–SiO_2–FeO–H_2O$ system are relatively well known (e.g. Evans, 2004; Evans, 2008; Evans et al., 2013; Frost and Beard, 2007; Klein et al., 2013; Klein and Garrido, 2011; McCollom and Bach, 2009; O'Hanley and Wicks, 1995), but many questions regarding the reaction pathways followed even by the simplest dunitic rock infiltrated by a fluid phase. For example, some workers have observed that early-formed serpentine veins lack magnetite, and that the iron originally hosted by common mantle olivine (Fo90) is hosted instead by secondary serpentine or brucite $(Mg,Fe)OH_2$. During the later stages of serpentinisation, steep increases in the modal abundance of magnetite are accompanied by a decrease in the FeO content of serpentine (e.g. Bach et al., 2006; Beard et al., 2009; Frost et al., 2013; Miyoshi et al., 2014). This observation has been explained by a kinetically controlled return to equilibrium during the later stages of serpentinisation (Andreani et al., 2013b), but also by formation under equilibrium conditions at appropriate length scales driven by changes in a_{H2O} and a_{SiO2} (Evans et al., 2013; Frost et al., 2013; Mothersole et al., 2017). Miyoshi et al. (2014) proposed a two stage model for serpentine vein formation, and suggested that Si release from Opx controlled magnetite formation. In contrast, Beard and Frost (2017) proposed that Fe hosted by brucite is an important source for magnetite formation. A subsequent experimental study on magnetite formation provided evidence for Al-controlled reactions during the early stages of serpentinisation and Si-controlled reactions during the later stages of serpentinisation (Huang et al., 2017a). Schwarzenbach et al. (2016) argued for a continuous mineral evolution during vein formation and chemical transfer of Si form Opx domains into Ol domains. Furthermore, McCollom et al. (2016) reported experimental brucite compositions that did not match thermodynamic predictions. The co-occurrence of lizardite and chrysotile, which are both low temperature serpentine polymorphs, over a wide range of conditions, is another puzzling observation. Chrysotile is recognised as metastable and is thought to re-crystallise

eventually to form lizardite (Evans, 2004). However, the mechanisms that produce any given serpentine morphology are unclear. There are a wide range of different morphologies in addition to the commonly recognised flat lizardite and rolled chrysotile structures; these include cone in cone, polygonal, and polyhedral serpentine, and their formation has been linked to the degree of supersaturation, or the concentrations of trace elements, but are otherwise poorly constrained (Andreani et al., 2008; Andreani et al., 2007; Baronnet et al., 2007; Baronnet and Devouard, 1996; Lafay et al., 2014; Malvoisin et al., 2012; Normand et al., 2002). The rate of serpentinisation reactions is also of interest, and of particular interest in large-scale geological modelling applications (e.g. Dunn et al., 2017; Malvoisin et al., 2017). Numerous studies have identified a range of factors that influence the reaction rate; these include grain size, temperature, pressure, fluid composition, solid bulk composition (e.g. Malvoisin et al., 2012; Marcaillou et al., 2011; Martin and Fyfe, 1970; Moody, 1976; Normand et al., 2002; Seyfried Jr et al., 2007). Recent studies have highlighted the effects of fluid and bulk composition on reaction kinetics, with, for example, increases in reaction rate of up to two orders of magnitude in response to the addition of Al or NaOH (Andreani et al., 2013a; Lafay et al., 2012; Pens et al., 2016). In contrast, the addition of salts ($MgCl_2$ and NaCl) reduces reaction rate by decreasing the activity of H_2O (Lamadrid et al., 2017). Previously, it was argued that reaction kinetics were similar in dunites and peridotites (Malvoisin et al., 2012). In contrast, recent experimental studies have provided compelling evidence for a link between solid bulk composition and the overall reaction kinetics, based on the effect of the liberation of Al and Cr from pyroxene and spinel into the reacting fluid (Huang et al., 2017b). Huang et al. (2017b) argued that Si has a negligible influence on the reaction kinetics, whereas other studies have reported that olivine in direct contact with pyroxene is more highly altered than olivine elsewhere, and that this can be explained by high Si concentrations at the reaction site (Ogasawara et al., 2013; Okamoto et al., 2013; Okamoto et al., 2011). The formation of magnetite and brucite is an important component of the overall serpentinisation reaction; these phases provide a host for Fe released by the primary olivine so that the secondary serpentine

has a higher xMg than the parent olivine (e.g. Klein et al., 2013). The iron released by olivine dissolution can becomes oxidized to form magnetite ($Fe^{2+}Fe^{3+}{}_2O_4$). This iron oxidation is responsible for the highly reducing conditions associated with serpentinisation and the generation of H_2, which stabilises phases such as awaruite (Ni_3Fe) (Eckstrand, 1975). The overall degree of oxidation can be expressed as the Fe^{3+}/Fe_{tot} of a serpentinised rock; this parameter is an important indicator of the amount of H_2 that might have been generated and thermodynamic calculations can use this parameter to estimate the water:rock ratio seen by serpentinised rocks (Klein et al., 2009). Also, Fe^{3+}/Fe_{tot} might influence the precipitated serpentine polymorph, although Andreani et al. (2013b) found no relation between serpentine morphology and Fe^{3+}/Fe_{tot}. Ferric iron can also be accommodated by serpentine through vacancy generation or Tschermark's substitution to form solid solutions between the ferric-free and cronstedtite end members (e.g. Beard and Frost, 2017). The relationship between the formation of ferric serpentine, magnetite and H_2 generation is still debated (Beard and Frost, 2017; Syverson et al., 2017).

The serpentinisation reaction is a classic example of a fluid-driven replacement reaction (Putnis, 2009), and exhibits many features characteristic of CDR, such as porosity generation within the secondary phase and a sharp contact between the parent mineral and the secondary phase. Evans (2010) highlights the importance of olivine dissolution as the mechanism that drives the formation of chrysotile and lizardite; cation diffusion in olivine is extremely sluggish under low temperature conditions so the reactions are not diffusion-driven. Another possible example of a kinetically-driven process is the inhibition of magnetite formation in favour of incorporation of Fe in serpentine, in natural samples (e.g. Andreani et al., 2013b). If this explanation is correct, then the observed textures form because nucleation on a parent mineral is favoured over heterogeneous nucleation. Experimental studies of the alteration of olivine suggest that the rate limiting process is olivine dissolution when grain sizes are >5 µm and serpentine formation when the grainsizes are <5 µm, with implications for the precipitated polymorph (Malvoisin et al., 2012; Normand et al., 2002). The

increased degree of supersaturation when the olivine grain size is smaller leads to the formation of chrysotile, whereas lizardite forms at lower degrees of supersaturation.

Olivine is the most abundant mineral in ultramafic rocks but orthopyroxene is also common. Experimental studies of the serpentinisation of Opx reveal that reaction kinetics are slower than that of olivine from 200–300°C and faster than for olivine above 300°C (Martin and Fyfe, 1970; Ogasawara et al., 2013; Ohnishi and Tomeoka, 2007; Okamoto et al., 2011). Ohnishi and Tomeoka (2007) found that the solution composition has primary control on the alteration assemblage and degree of alteration. In highly alkaline conditions, the reaction rates increase and an assemblage of serpentine + saponite ($(Na,K)_{0.3}(Mg,Fe)_3(Si,Al)_4O_{10}(OH)_2 \cdot nH_2O$) is stabilised , in contrast to the stabilisation of serpentine alone at lower pH. Thermodynamic calculations predict that the stable assemblage produced by Opx alteration is serpentine + talc ($Mg_3Si_4O_{10}OH_2$). However, talc is seldom observed as a reaction product at lower temperatures (~250°C); instead, phyllosilicates such as chlorite, saponite or stevensite ($(Ca_{0.5},Na)_{0.33}(Mg,Fe^{2+})_3Si_4O_{10}(OH)_2 \cdot nH_2O$) are common experimental products of the hydration of Opx or, of the hydration of Ol in the presence of a source of Si (e.g. Oyanagi et al., 2015). Okamoto et al. (2011) argued that the pyroxene composition used in their experiments favoured chlorite precipitation.

1.1.2 Sulphides

Nickel sulphide deposits are often hosted by ultramafic rocks, and are of particular importance in the Archean greenstone belts of Western Australia. Many of the host rocks of these deposits have undergone extensive alteration by aqueous fluids, producing serpentine phases and carbonates (e.g. Barnes and Hill, 2000; Butt and Brand, 2005; Butt and Nickel, 1981; Grguric, 2003; Grguric et al., 2007; Grguric et al., 2013). Sulphide minerals are often present in the serpentinised host rock, and these are often altered to high Ni-tenor phases, such as millerite (NiS), heazlewoodite (Ni_2S_3), and even native nickel (e.g. Grguric, 2003; Grguric et al., 2013). The formation of these Ni-rich sulphides is common in rocks that contain low modal

abundance of sulphides (disseminated deposits). In contrast, deposits with large modal abundances of sulphides (massive deposits) tend to consist of a homogeneous assemblage of pentlandite ($Fe_{4.5}Ni_{4.5}S_8$) + pyrrhotite ($Fe_{(1-x)}S$) + pyrite (FeS_2) (Grguric et al., 2007). The original assemblage is retained in cases where the sulphide assemblage buffers the redox state sufficiently to prevent the formation of the strongly reducing conditions typical of olivine serpentinisation (Eckstrand, 1975). There is a paucity of experimental data at low temperatures for these systems. Filippidis (1982) and Filippidis (1985) reported the formation of fine-grained Ni-sulphides within serpentine during the reaction between Ni-olivine and an S-bearing fluid. The hydrothermal upgrade of Ni-sulphides in these deposits is generally recognised but the mechanism is poorly understood. Two contrasting models have been used to explain the alteration in disseminated Ni-sulphide deposits. The first model suggests that nickel released by olivine alteration is partitioned into existing sulphide minerals (Barnes and Hill, 2000; Donaldson, 1981; Eckstrand, 1975; Groves et al., 1974; Sciortino et al., 2015). A second model suggests that the Fe component of Ni-Fe-sulphide is oxidised, leading to an increase in nickel in the residual sulphides (Gole, 2014; Grguric, 2003; Grguric et al., 2007; Grguric et al., 2013; Konnunaho et al., 2013). Further constraints on this process could provide insights into the genesis of these type of deposits, with implications for mineral exploration and processing.

Pentlandite is the most important economic Ni-bearing mineral in sulphide-hosted Ni-deposits. Many studies focussed on phase relations in the system Fe–Ni–S, mainly using the fused silica tube method (e.g. Craig, 1973; Misra and Fleet, 1973; Naldrett et al., 1967). Recent experiments investigated the alteration of pentlandite by a fluid phase, with a focus on the controlling mechanisms. Tenailleau et al. (2006); Xia et al. (2009) found that replacement of pentlandite by violarite ($FeNi_2S_4$) occurs in preference to replacement by the thermodynamically stable phases vaesite (NiS_2) and polydymite (Ni_3S_4); this was attributed to similarities between the crystal structures of pentlandite and violarite. Another example of the importance of surface nucleation is sulphidation of hematite (Fe_2O_3) in the presence of S and Cu. Chalcocite (Cu_2S) and bornite (Cu_5FeS_4) are the thermodynamically stable phases and expected products

but hematite was replaced by chalcopyrite ($CuFeS_2$) instead (Li et al., 2015; Zhao et al., 2014). Furthermore, Xia et al. (2009) showed that the length scale of pseudomorphic replacement depends on whether the rate limiting process is dissolution of the host or precipitation of the secondary mineral. In these experiments, solutions with $1 < pH < 6$ induced pseudomorphic replacement whereas solutions with pH 1 produced spatially decoupled relationship between dissolution and precipitation. Xia et al. (2008) investigated the viability of fast formation of a range of sulphides with low thermal stability, testing the hypothesis that CDR is much faster than conventional solid state reactions that rely on diffusion as the reaction-driving process. Qian et al. (2011) showed that hydrothermal replacement of pyrrhotite by marcasite (FeS_2) or pyrite proceeds via a dissolution-reprecipitation mechanism and found that the chemistry of the solution determined the identity of the product. Hydrothermal replacement of chalcopyrite by bornite produces a sharp reaction front without a gap between parent and precipitating, characteristic of CDR where the dissolution of the parent mineral is the rate limiting step. However the replacement is not pseudomorphic in this case, because the original grain boundary is overgrown by the secondary phase; this is consistent with the positive volume change associated with the reaction. The products were calculated to require twice the volume of the reactants, if Fe is conserved (Zhao et al., 2014). Furthermore bornite produced by replacement of chalcopyrite is homogeneous and lacks porosity, these features were interpreted as a record of interactions between fluid-driven replacement and solid-state diffusion mechanisms. Such features and processes are typical of mineral systems where the phases show a high ionic conductivity, such as certain sulphides and alloys (Zhao et al., 2014; Zhao et al., 2013; Zhao and Pring, 2019).

1.1.3 Oxides

Oxides are commonly accessory minerals and present in low modes in rocks, but localities enriched in these minerals are an important source of certain metals, e.g. iron, titanium, chromium, and vanadium. An understanding of their chemical behaviour is important for ore processing, but also because they record some aspects

of a rock's metamorphic history that are not recorded in any other way. The replacement of magnetite was the focus of hydrothermal experiments by Qian et al. (2010) at 90–300°C and a wide range of pH conditions. They inferred that the governing mechanism was dissolution-reprecipitation and that the solution composition and temperature controlled the secondary formation of marcasite and pyrite. Zhao et al. (2019) reported pseudomorphic replacement of magnetite by hematite via an interface coupled dissolution-reprecipitation reaction, and found that the factors controlling magnetite dissolution, such as temperature and solution parameters, have a strong effect on the reaction kinetics. Magnetite and chromite ($FeCr_2O_4$) are common in ultramafic rocks and alteration of these minerals produces a range of secondary phases with a variety of textures and porosity (Colás et al., 2017). The secondary phase assemblage in altered ultramafic rocks highlights the importance of fluid composition involved in replacement reactions; for example iowaite ($Mg_6Fe_2(OH)_{16}Cl_2 \cdot 4H_2O$) and woodalite ($Mg_6Cr_2(OH)_{16}Cl_2 \cdot 4H_2O$) record different conditions to pyroaurite ($Mg_6Fe_2(OH)_{16}[CO_3] \cdot 4H_2O$) and stichtite ($Mg_6Cr_2(OH)_{16}[CO_3] \cdot 4H_2O$) (e.g. Gole, 2014; Grguric et al., 2001). Ilmenite alteration under earth surface conditions produces a range of different products from hydrated rutile to pseudorutile to leucoxene (Pownceby, 2010), although the exact mechanisms are not well understood (Grey and Reid, 1975; Janssen et al., 2010). Ilmenite is the most important titanium ore used in the production of TiO_2 particles, because of the availability of large reserves. Ground ilmenite is reacted with either sulphuric acid or hydrochloric acid, depending on the subsequent processing route. The reaction with the latter aims to produce a feedstock "synthetic rutile" for the chlorination process of TiO_2 production, by hydrothermally replacing ilmenite with synthetic rutile. Impurities that are commonly found in natural ilmenite ore, such as Si, Mn, Mg, V, and Cr have a negative impact on the final product and can cause problems in the processing equipment. Thus, it is important to understand the behaviour of ilmenite and its impurities to maintain and optimize the system output. Previous work focussed on reaction kinetics and chemical compositions of the reaction products and found solid/acid ratio, acid concentration, temperature, grain

size and mechanical or thermal activation to be important factors controlling the reaction of ilmenite in hydrochloric acid (El-Hazek et al., 2007; Janssen and Putnis, 2011; Ping et al., 2011; Van Dyk et al., 2002). Janssen et al. (2010) used Raman spectroscopy to map the reaction products of ilmenite that had been reacted with an ^{18}O-enriched solution, and concluded that the reaction proceeded through complete dissolution and reprecipitation of the ilmenite/synthetic rutile, rather than by cation leaching with preservation of the oxygen lattice. Angiboust and Harlov (2017) demonstrated that replacement of ilmenite by pseudomorphic rutile/titanate at 0.7–1.6 GPa and 450–650°C in the presence of fluid depends on pressure and the system bulk composition, particularly the activity of Ca.

1.2 Single phase vs. composite system

Geological systems are rarely monomineralic, but rather consist of a mixture of different minerals that depend on the geological setting as well as the bulk composition of the system. During hydrothermal rock alteration, dissolved species within the fluid phase must be considered, because they contribute to the element budget of the system. Many hydrothermal experimental studies have been performed on systems consisting of a monomineralic solid phase and systems consisting of multiple solid phases. The aim of such experiments is constrain reaction paths, kinetics, and reaction mechanisms. Recent studies have highlighted the complex reaction paths followed by hydrothermal alteration reactions that lead to unexpected changes in the reaction rate, chemical composition, or mineral assemblage (de Ruiter and Austrheim, 2018; De Ruiter et al., 2019; McCollom et al., 2016; Ruiz-Agudo et al., 2016). This complicates the extrapolation of experimental results produced by studies of single phases to more complex geological systems. For example monomineralic olivine alteration is faster at some conditions than alteration of monomineralic enstatite (Ogasawara et al., 2013; Okamoto et al., 2011). However, when the two minerals are brought together as two separate domains, the reaction rate is higher proximal to contacts between the olivine and enstatite domains (Ogasawara et al., 2013; Okamoto et al., 2013). This serpentinisation reaction has also been

reported to be faster than in the individual systems for experiments on peridotite powders (Huang et al., 2017b). Significant discrepancies exist between different experiments on the same system (Malvoisin et al., 2012; Marcaillou et al., 2011; Seyfried Jr et al., 2007), but it is clear that a given phase can affect the reaction kinetics another phase. Furthermore, the chemical evolution of a hydrothermal system depends on the relative dissolution rates of the individual minerals. In low temperature hydrothermal systems, it is argued that reaction only proceeds by CDR without any influence of chemical exchange by solid state diffusion (e.g. Evans, 2010; Putnis, 2009). In this case, only a quantity of material that can dissolve can react. If the relative dissolution rates of two minerals within a system are different, then the composition of the fluid is dominated by the composition of the faster dissolving mineral and metastable assemblages might precipitate or the precipitation of some minerals might be suppressed; these consequences would not be predicted by thermodynamic calculations on the bulk system. The different characteristic length scales of alteration reactions account for links between the alteration of one phase and the reaction of a second phase. If CDR occurs, then the precipitating phase depends on the composition of the interfacial fluid, which is different to the composition of the bulk fluid that is measured in conventional experimental setups (e.g. Geisler et al., 2019; Putnis et al., 2005; Ruiz-Agudo et al., 2016). Recent studies have shown that the dissolution rates of silicate minerals are strongly influenced by dissolution reprecipitation reactions, with consequences that include the formation of inhibiting silica-rich layers or the formation of Mg-silicate phases, and dissolution rates in nature that are much higher than experimentally obtained data (de Ruiter and Austrheim, 2018; De Ruiter et al., 2019; Emmanuel et al., 2010; Ruiz-Agudo et al., 2016).

If two mineral grains of different compositions are in close proximity to each other and reacting with a fluid phase, then the chemical species released to the bulk fluid by the reaction of the fluid with one mineral will eventually influence the reaction of the fluid with the other mineral, and vice versa, which limits the applicability of experiments on monomineralic systems to more complex geologic systems. Detailed investigations of reaction mechanisms within composite mineral systems are

necessary determine the reaction path of complex hydrothermal alteration reactions. Understanding the effect of the alteration of a single phase alteration on the other minerals within a composite system is especially important in geological systems, because these are almost always polymineralic, so insights into these systems have implications for ore genesis and mineral processing. The coupled dissolution reprecipitation mechanism provides a good framework for the understanding and description of such reactions, yet further research is necessary to establish a robust model to predict reaction pathways for these complex natural mineral systems.

1.3 Objectives

1. Provide new insight into the serpentinisation of olivine at low temperature conditions. The objective was to calculate reaction rates and document the morphology of secondary minerals, and derive functional relationships between these parameters, fluid composition, and the amount of added enstatite (Chapter 2).
2. The hydrothermal alteration of a primary Fe–Ni–sulphide assemblage hosted by an ultramafic rock was investigated. The objective was to document the alteration assemblage and textural features, and investigate the effects of changes in the initial bulk composition (Chapter 3).
3. The hydrothermal treatment of natural hematite-bearing ilmenite in acidic solutions. The objective was to investigate the textural evolution of the secondary phases and the comparison to results from the literature (Chapter 4).

1.4 Thesis structure

This thesis starts with an introductory chapter to give an overview of the mechanism of fluid rock interaction and a review on replacement reactions in the mineral systems relevant for this study. The main body of this thesis is comprised of Chapter 2 – 4. Each chapter constitutes the significant findings of their respective topic. Preliminary experiments were performed for each mineral system in order to find adequate experimental conditions to be able to investigate the reactions.

The first mineral system investigated in this study (Chapter 2) is the serpentinisation of ultramafic rock (olivine ± enstatite). The dependence of serpentine morphology was explored as a function of salinity and chemical composition of the parent material, therefore different ratios of olivine and enstatite were used. In addition this chapter encompasses the influence of chemical composition of solid and fluid phase on the kinetics of the serpentinisation reaction with respect to the influence of Si liberated by the dissolution of primary enstatite. A range of preliminary experiments, using different starting materials, reacting fluid compositions and fluid rock ratios, were employed to achieve the optimal conditions, which are applicable to nature, and generate a sufficient reaction extent, to allow robust data generation as well as mitigating challenges encountered with experimental setups.

The third chapter of this thesis deals with the hydrothermal overprinting of Fe-Ni-sulphides as response to concurrent serpentinisation of a host rock simulating Fe-Ni-sulphide deposits. Knowledge obtained from pure serpentinisation experiments (Chapter 1) was employed to adjust optimal conditions for this study. Preliminary experiments were conducted mainly with different fluid compositions. A high fluid pH with the addition of NaCl was chosen as fluid composition for this subject as this composition reflects the natural fluid compositions associated with serpentinisation of ultramafic rocks. The hydrothermal overprinting of primary sulphides was studied as a function of sulphide composition, sulphide to silicate ratio and time. An additional

experimental setup (reactor) was used to investigate the effect of oxygen free conditions on the resulting sulphide assemblages.

The fourth chapter explores the effect of concurrently reacting ilmenite and hematite, in the form of pre-existing exsolution lamellae on the reaction mechanism of this fluid driven replacement reaction. Preliminary experiments for this study focussed on different reacting fluid compositions and additional reactants, which resulted in only limited reaction extent. Experimental conditions were adopted from previous studies reported in literature to allow direct comparison of the results. In addition, FIB-tomography was employed as a method to obtain a better spatial understanding of this reaction.

1.5 References

Altree-Williams, A., Pring, A., Ngothai, Y., Brugger, J., 2015. Textural and compositional complexities resulting from coupled dissolution–reprecipitation reactions in geomaterials. Earth-Science Reviews, 150: 628-651.

Andreani, M., Daniel, I., Pollet-Villard, M., 2013a. Aluminum speeds up the hydrothermal alteration of olivine. American Mineralogist, 98(10): 1738-1744.

Andreani, M., Grauby, O., Baronnet, A., Muñoz, M., 2008. Occurrence, composition and growth of polyhedral serpentine. European Journal of Mineralogy, 20(2): 159-171.

Andreani, M., Mével, C., Boullier, A.M., Escartin, J., 2007. Dynamic control on serpentine crystallization in veins: Constraints on hydration processes in oceanic peridotites. Geochemistry, Geophysics, Geosystems, 8(2).

Andreani, M., Munoz, M., Marcaillou, C., Delacour, A., 2013b. μXANES study of iron redox state in serpentine during oceanic serpentinization. Lithos, 178: 70-83.

Angiboust, S., Harlov, D., 2017. Ilmenite breakdown and rutile-titanite stability in metagranitoids: Natural observations and experimental results. American Mineralogist, 102(8): 1696-1708.

Bach, W., Paulick, H., Garrido, C.J., Ildefonse, B., Meurer, W.P. and Humphris, S.E. 2006. Unraveling the sequence of serpentinization reactions: petrography, mineral chemistry, and petrophysics of serpentinites from MAR 15 N (ODP Leg 209, Site 1274). Geophysical research letters 33.

Barnes, S.J., Hill, R.E., 2000. Metamorphism of komatiite-hosted nickel sulfide deposits.

Baronnet, A., Andréani, M., Grauby, O., Devouard, B., Nitsche, S. and Chaudanson, D. 2007. Onion morphology and microstructure of polyhedral serpentine. American Mineralogist 92, 687-690.

Baronnet, A., Devouard, B., 1996. Topology and crystal growth of natural chrysotile and polygonal serpentine. Journal of Crystal Growth, 166(1-4): 952-960.

Beard, J.S., Frost, B.R., 2017. The stoichiometric effects of ferric iron substitutions in serpentine from microprobe data. International Geology Review, 59(5-6): 541-547.

Beard, J.S., Frost, B.R., Fryer, P., McCaig, A., Searle, R., Ildefonse, B., Zinin, P. and Sharma, S.K. 2009. Onset and progression of serpentinization and magnetite formation in olivine-rich troctolite from IODP Hole U1309D. Journal of Petrology 50, 387-403.

Butt, C., Brand, N., 2005. Mt. Keith nickel sulphide deposit, Western Australia. Regolith Expression of Australian Ore Systems: 112-114.

Butt, C., Nickel, E., 1981. Mineralogy and geochemistry of the weathering of the disseminated nickel sulfide deposit at Mt. Keith, Western Australia. Economic Geology, 76(6): 1736-1751.

Colás, V., Padrón-Navarta, J.A., González-Jiménez, J.M., Fanlo, I., Sánchez-Vizcaíno, V.L., Gervilla, F. and Castroviejo, R. 2017. The role of silica in the hydrous metamorphism of chromite. Ore Geology Reviews 90, 274-286.

Cole, D.R., Larson, P.B., Riciputi, L.R., Mora, C.I., 2004. Oxygen isotope zoning profiles in hydrothermally altered feldspars: Estimating the duration of water-rock interaction. Geology, 32(1): 29-32.

Craig, J.R., 1973. Pyrite-pentlandite assemblages and other low temperature relations in the Fe-Ni-S system. American Journal of Science, 273(A): 496-510.

de Ruiter, L., Austrheim, H., 2018. Formation of magnesium silicate hydrate cement in nature. Journal of the Geological Society, 175(2): 308-320.

De Ruiter, L., Putnis, C.V., Hövelmann, J.r., King, H.E., Austrheim, H., 2019. Direct observations of the coupling between quartz dissolution and Mg-silicate formation. ACS Earth and Space Chemistry, 3(4): 617-625.

Donaldson, M., 1981. Redistribution of ore elements during serpentinization and talc-carbonate alteration of some Archean dunites, Western Australia. Economic Geology, 76(6): 1698-1713.

Dunn, R.A., Arai, R., Eason, D.E., Canales, J.P., Sohn, R.A., 2017. Three-Dimensional Seismic Structure of the Mid-Atlantic Ridge: An Investigation of Tectonic, Magmatic, and Hydrothermal Processes in the Rainbow Area. Journal of Geophysical Research: Solid Earth, 122(12): 9580-9602.

Eckstrand, O., 1975. The Dumont serpentinite; a model for control of nickeliferous opaque mineral assemblages by alteration reactions in ultramafic rocks. Economic Geology, 70(1): 183-201.

El-Hazek, N., Lasheen, T., El-Sheikh, R., Zaki, S.A., 2007. Hydrometallurgical criteria for TiO_2 leaching from Rosetta ilmenite by hydrochloric acid. Hydrometallurgy, 87(1-2): 45-50.

Emmanuel, S., Ague, J.J., Walderhaug, O., 2010. Interfacial energy effects and the evolution of pore size distributions during quartz precipitation in sandstone. Geochimica et Cosmochimica Acta, 74(12): 3539-3552.

Evans, B.W., 2004. The serpentinite multisystem revisited: chrysotile is metastable. International Geology Review, 46(6): 479-506.

Evans, B.W., 2008. Control of the products of serpentinization by the Fe2+ Mg− 1 exchange potential of olivine and orthopyroxene. Journal of Petrology, 49(10): 1873-1887.

Evans, B.W., 2010. Lizardite versus antigorite serpentinite: Magnetite, hydrogen, and life (?). Geology, 38(10): 879-882.

Evans, K., Powell, R., Frost, B., 2013. Using equilibrium thermodynamics in the study of metasomatic alteration, illustrated by an application to serpentinites. Lithos, 168: 67-84.

Farough, A., Moore, D.E., Lockner, D.A., Lowell, R., 2016. Evolution of fracture permeability of ultramafic rocks undergoing serpentinization at hydrothermal conditions: An experimental study. Geochemistry, Geophysics, Geosystems, 17(1): 44-55.

Filippidis, A., 1982. Experimental study of the serpentinization of Mg-Fe-Ni olivine in the presence of sulfur. The Canadian Mineralogist, 20(4): 567-574.

Filippidis, A., 1985. Formation of awaruite in the system Ni-Fe-Mg-Si-OHS and olivine hydration with NaOH solution, an experimental study. Economic Geology, 80(7): 1974-1980.

Frost, B.R., Beard, J.S., 2007. On silica activity and serpentinization. Journal of petrology, 48(7): 1351-1368.

Frost, B.R., Evans, K.A., Swapp, S.M., Beard, J.S., Mothersole, F.E., 2013. The process of serpentinization in dunite from New Caledonia. Lithos, 178: 24-39.

Geisler, T., Dohmen, L., Lenting, C., Fritzsche, M.B., 2019. Real-time in situ observations of reaction and transport phenomena during silicate glass corrosion by fluid-cell Raman spectroscopy. Nature materials: 1.

Gole, M.J., 2014. Leaching of S, Cu, and Fe from disseminated Ni-(Fe)-(Cu) sulphide ore during serpentinization of dunite host rocks at Mount Keith, Agnew-Wiluna Belt, Western Australia. Mineralium Deposita, 49(7): 821-842.

Grey, I.E., Reid, A.F., 1975. The structure of pseudorutile and its role in the natural alteration of ilmenite. American Mineralogist: Journal of Earth and Planetary Materials, 60(9-10): 898-906.

Grguric, B., 2003. Minerals of the MKD5 nickel deposit, Mount Keith, Western Australia. Australian Journal of Mineralogy, 9: 55-71.

Grguric, B., Madsen, I., Pring, A., 2001. Woodallite, a new chromium analogue of iowaite from the Mount Keith nickel deposit, Western Australia. Mineralogical Magazine, 65(3): 427-435.

Grguric, B., Rosengren, N., Fletcher, C., Hronsky, J., 2007. Type 2 deposits: Geology, mineralogy, and processing of the Mount Keith and Yakabindie orebodies, Western Australia. Special Publication-Society of Economic Geologists, 13: 119.

Grguric, B.A., Seat, Z., Karpuzov, A.A., Simonov, O.N., 2013. The West Jordan deposit, a newly-discovered type 2 dunite-hosted nickel sulphide system in the northern Agnew–Wiluna belt, Western Australia. Ore Geology Reviews, 51: 79-92.

Groves, D., Hudson, D., Hack, T., 1974. Modification of iron-nickel sulfides during serpentinization and talc-carbonate alteration at Black Swan, Western Australia. Economic Geology, 69(8): 1265-1281.

Hellmann, R., Wirth, R., Daval, D., Barnes, J.-P., Penisson, J.-M., Tisserand, D., Epicier, T., Florin, B. and Hervig, R.L. 2012. Unifying natural and laboratory chemical weathering with interfacial dissolution–reprecipitation: a study based on the nanometer-scale chemistry of fluid–silicate interfaces. Chemical Geology 294, 203-216.

Huang, R., Lin, C.-T., Sun, W., Ding, X., Zhan, W. and Zhu, J. 2017a. The production of iron oxide during peridotite serpentinization: Influence of pyroxene. Geoscience Frontiers 8, 1311-1321.

Huang, R., Song, M., Ding, X., Zhu, S., Zhan, W. and Sun, W. 2017b. Influence of pyroxene and spinel on the kinetics of peridotite serpentinization. Journal of Geophysical Research: Solid Earth 122, 7111-7126.

Iyer, K., Austrheim, H., John, T., Jamtveit, B., 2008. Serpentinization of the oceanic lithosphere and some geochemical consequences: constraints from the Leka Ophiolite Complex, Norway. Chemical Geology, 249(1-2): 66-90.

Jamtveit, B., Hammer, Ø., 2012. Sculpting of rocks by reactive fluids. Geochemical Perspectives, 1(3): 341-342.

Jamtveit, B., Malthe-Sørenssen, A., Kostenko, O., 2008. Reaction enhanced permeability during retrogressive metamorphism. Earth and Planetary Science Letters, 267(3-4): 620-627.

Jamtveit, B., Putnis, C.V., Malthe-Sørenssen, A., 2009. Reaction induced fracturing during replacement processes. Contributions to Mineralogy and Petrology, 157(1): 127-133.

Janssen, A., Putnis, A., 2011. Processes of oxidation and HCl-leaching of Tellnes ilmenite. Hydrometallurgy, 109(3-4): 194-201.

Janssen, A., Putnis, A., Geisler, T., Putnis, C., 2010. The experimental replacement of ilmenite by rutile in HCl solutions. Mineralogical Magazine, 74(4): 633-644.

Klein, F., Bach, W., Jöns, N., McCollom, T., Moskowitz, B. and Berquó, T. 2009. Iron partitioning and hydrogen generation during serpentinization of abyssal peridotites from 15 N on the Mid-Atlantic Ridge. Geochimica et Cosmochimica Acta 73, 6868-6893.

Klein, F., Bach, W., McCollom, T.M., 2013. Compositional controls on hydrogen generation during serpentinization of ultramafic rocks. Lithos, 178: 55-69.

Klein, F., Garrido, C.J., 2011. Thermodynamic constraints on mineral carbonation of serpentinized peridotite. Lithos, 126(3-4): 147-160.

Konnunaho, J., Hanski, E., Bekker, A., Halkoaho, T., Hiebert, R. and Wing, B. 2013. The Archean komatiite-hosted, PGE-bearing Ni–Cu sulfide deposit at Vaara, eastern Finland: evidence for assimilation of external sulfur and post-depositional desulfurization. Mineralium Deposita, 48(8), 967-989.

Labotka, T.C., Cole, D.R., Fayek, M., Riciputi, L.R., Stadermann, F.J., 2004. Coupled cation and oxygen-isotope exchange between alkali feldspar and aqueous chloride solution. American Mineralogist, 89(11-12): 1822-1825.

Lafay, R., Montes-Hernandez, G., Janots, E., Auzende, A.-L., Chiriac, R., Lemarchand, D. and Toche, F. 2014. Influence of trace elements on the textural properties of synthetic chrysotile: Complementary insights from macroscopic and nanoscopic measurements. Microporous and Mesoporous Materials 183, 81-90.

Lafay, R., Montes-Hernandez, G., Janots, E., Chiriac, R., Findling, N. and Toche, F. 2012. Mineral replacement rate of olivine by chrysotile and brucite under high alkaline conditions. Journal of Crystal Growth, 347(1), 62-72.

Lamadrid, H.M., Rimstidt, J.D., Schwarzenbach, E.M., Klein, F., Ulrich, S., Dolocan, A. and Bodnar, R.J. 2017. Effect of water activity on rates of serpentinization of olivine. Nature communications 8, 16107.

Lenting, C., Plümper, O., Kilburn, M., Guagliardo, P., Klinkenberg, M. and Geisler, T. 2018. Towards a unifying mechanistic model for silicate glass corrosion. npj Materials Degradation 2, 28.

Li, K., Pring, A., Etschmann, B., Macmillan, E., Ngothai, Y., O'Neill, B., Hooker, A., Mosselmans, F. and Brugger, J. 2015. Uranium scavenging during mineral replacement reactions. American Mineralogist 100, 1728-1735.

Malvoisin, B., Brantut, N., Kaczmarek, M.-A., 2017. Control of serpentinisation rate by reaction-induced cracking. Earth and Planetary Science Letters, 476: 143-152.

Malvoisin, B., Brunet, F., Carlut, J., Rouméjon, S., Cannat, M., 2012. Serpentinization of oceanic peridotites: 2. Kinetics and processes of San Carlos olivine hydrothermal alteration. Journal of Geophysical Research: Solid Earth, 117(B4).

Marcaillou, C., Munoz, M., Vidal, O., Parra, T., Harfouche, M., 2011. Mineralogical evidence for H2 degassing during serpentinization at 300 C/300 bar. Earth and Planetary Science Letters, 303(3-4): 281-290.

Martin, B., Fyfe, W., 1970. Some experimental and theoretical observations on the kinetics of hydration reactions with particular reference to serpentinization. Chemical geology, 6: 185-202.

Mayhew, L.E., Ellison, E., McCollom, T., Trainor, T., Templeton, A., 2013. Hydrogen generation from low-temperature water–rock reactions. Nature Geoscience, 6(6): 478.

McCollom, T.M., Bach, W., 2009. Thermodynamic constraints on hydrogen generation during serpentinization of ultramafic rocks. Geochimica et Cosmochimica Acta, 73(3): 856-875.

McCollom, T.M., Klein, F., Robbins, M., Moskowitz, B., Berquó, T.S., Jöns, N., Bach, W. and Templeton, A. 2016. Temperature trends for reaction rates, hydrogen generation, and partitioning of iron during experimental serpentinization of olivine. Geochimica et Cosmochimica Acta 181, 175-200.

Misra, K., Fleet, M., 1973. The chemical compositions of synthetic and natural pentlandite assemblages. Economic Geology, 68(4): 518-539.

Miyoshi, A., Kogiso, T., Ishikawa, N., Mibe, K., 2014. Role of silica for the progress of serpentinization reactions: Constraints from successive changes in mineralogical textures of serpentinites from Iwanaidake ultramafic body, Japan. American Mineralogist, 99(5-6): 1035-1044.

Moody, J., 1976. An experimental study on the serpentinization of iron-bearing olivines. The Canadian Mineralogist, 14(4): 462-478.

Mora, C.I., Riciputi, L.R., Cole, D.R., Walker, K.D., 2009. High-temperature hydrothermal alteration of the Boehls Butte anorthosite: origin of a bimodal plagioclase assemblage. Contributions to Mineralogy and Petrology, 157(6): 781.

Mothersole, F.E., Evans, K., Frost, B.R., 2017. Abyssal and hydrated mantle wedge serpentinised peridotites: a comparison of the 15°20′ N fracture zone and New Caledonia serpentinites. Contributions to Mineralogy and Petrology, 172(8): 69.

Naldrett, A., Craig, J., Kullerud, G., 1967. The central portion of the Fe-Ni-S system and its bearing on pentlandite exsolution in iron-nickel sulfide ores. Economic Geology, 62(6): 826-847.

Niedermeier, D.R., Putnis, A., Geisler, T., Golla-Schindler, U., Putnis, C.V., 2009. The mechanism of cation and oxygen isotope exchange in alkali feldspars under hydrothermal conditions. Contributions to Mineralogy and Petrology, 157(1): 65.

Normand, C., Williams-Jones, A.E., Martin, R.F., Vali, H., 2002. Hydrothermal alteration of olivine in a flow-through autoclave: Nucleation and growth of serpentine phases. American Mineralogist, 87(11-12): 1699-1709.

O'Hanley, D.S., 1992. Solution to the volume problem in serpentinization. Geology, 20(8): 705-708.

O'Hanley, D.S., Wicks, F.J., 1995. Conditions of formation of lizardite, chrysotile and antigorite, Cassiar, British Columbia. The Canadian Mineralogist, 33(4): 753-773.

Ogasawara, Y., Okamoto, A., Hirano, N., Tsuchiya, N., 2013. Coupled reactions and silica diffusion during serpentinization. Geochimica et Cosmochimica Acta, 119: 212-230.

Ohnishi, I., Tomeoka, K., 2007. Hydrothermal alteration experiments of enstatite: implications for aqueous alteration of carbonaceous chondrites. Meteoritics & Planetary Science, 42(1): 49-61.

Okamoto, A., Ogasawara, Y., Hirano, N., Tsushiya, N., 2013. Effect of silica transport on serpentinization in the Ol-Opx-H_2O system. Procedia Earth and Planetary Science, 7: 628-631.

Okamoto, A., Ogasawara, Y., Ogawa, Y., Tsuchiya, N., 2011. Progress of hydration reactions in olivine–H_2O and orthopyroxenite–H_2O systems at 250 C and vapor-saturated pressure. Chemical geology, 289(3-4): 245-255.

Oufi, O., Cannat, M., Horen, H., 2002. Magnetic properties of variably serpentinized abyssal peridotites. Journal of Geophysical Research: Solid Earth, 107(B5): EPM 3-1-EPM 3-19.

Oyanagi, R., Okamoto, A., Hirano, N., Tsuchiya, N., 2015. Competitive hydration and dehydration at olivine–quartz boundary revealed by hydrothermal experiments: Implications for silica metasomatism at the crust–mantle boundary. Earth and Planetary Science Letters, 425: 44-54.

Pens, M., Andreani, M., Daniel, I., Perrillat, J.-P., Cardon, H., 2016. Contrasted effect of aluminum on the serpentinization rate of olivine and orthopyroxene under hydrothermal conditions. Chemical Geology, 441: 256-264.

Ping, T., Hu, H.-P., Zhang, L., 2011. Effects of mechanical activation and oxidation-reduction on hydrochloric acid leaching of Panxi ilmenite concentration. Transactions of Nonferrous Metals Society of China, 21(6): 1414-1421.

Plümper, O., Beinlich, A., Bach, W., Janots, E., Austrheim, H., 2014. Garnets within geode-like serpentinite veins: Implications for element transport, hydrogen production and life-supporting environment formation. Geochimica et Cosmochimica Acta, 141: 454-471.

Power, I.M., Wilson, S.A., Dipple, G.M., 2013. Serpentinite carbonation for CO_2 sequestration. Elements, 9(2): 115-121.

Pownceby, M., 2010. Alteration and associated impurity element enrichment in detrital ilmenites from the Murray Basin, southeast Australia: a product of multistage alteration. Australian Journal of Earth Sciences, 57(2): 243-258.

Putnis, A., 2002. Mineral replacement reactions: from macroscopic observations to microscopic mechanisms. Mineralogical Magazine, 66(5): 689-708.

Putnis, A., 2009. Mineral replacement reactions. Reviews in mineralogy and geochemistry, 70(1): 87-124.

Putnis, A., Hinrichs, R., Putnis, C.V., Golla-Schindler, U., Collins, L.G., 2007. Hematite in porous red-clouded feldspars: evidence of large-scale crustal fluid–rock interaction. Lithos, 95(1-2): 10-18.

Putnis, A., Putnis, C.V., 2007. The mechanism of reequilibration of solids in the presence of a fluid phase. Journal of Solid State Chemistry, 180(5): 1783-1786.

Putnis, C.V., Ruiz-Agudo, E., 2013. The mineral–water interface: where minerals react with the environment. Elements, 9(3): 177-182.

Putnis, C.V., Tsukamoto, K., Nishimura, Y., 2005. Direct observations of pseudomorphism: compositional and textural evolution at a fluid-solid interface. American Mineralogist, 90(11-12): 1909-1912.

Qian, G., Brugger, J., Skinner, W.M., Chen, G., Pring, A., 2010. An experimental study of the mechanism of the replacement of magnetite by pyrite up to 300 C. Geochimica et Cosmochimica Acta, 74(19): 5610-5630.

Qian, G., Xia, F., Brugger, J., Skinner, W. M., Bei, J., Chen, G. and Pring, A. 2011. Replacement of pyrrhotite by pyrite and marcasite under hydrothermal conditions up to 220 C: An experimental study of reaction textures and mechanisms. American Mineralogist, 96(11-12), 1878-1893.

Ruiz-Agudo, E., King, H.E., Patiño-López, L.D., Putnis, C.V., Geisler, T., Rodriguez-Navarro, C. and Putnis, A. 2016. Control of silicate weathering by interface-coupled dissolution-precipitation processes at the mineral-solution interface. Geology 44, 567-570.

Ruiz-Agudo, E., Putnis, C., Putnis, A., 2014. Coupled dissolution and precipitation at mineral–fluid interfaces. Chemical Geology, 383: 132-146.

Russell, M.J., Hall, A., 1997. The emergence of life from iron monosulphide bubbles at a submarine hydrothermal redox and pH front. Journal of the Geological Society, 154(3): 377-402.

Schwarzenbach, E.M., Caddick, M.J., Beard, J.S., Bodnar, R.J., 2016. Serpentinization, element transfer, and the progressive development of zoning in veins: evidence from a partially serpentinized harzburgite. Contributions to Mineralogy and Petrology, 171(1): 5.

Sciortino, M., Mungall, J.E., Muinonen, J., 2015. Generation of High-Ni sulfide and alloy phases during serpentinization of dunite in the Dumont sill, Quebec. Economic Geology, 110(3): 733-761.

Seyfried Jr, W., Foustoukos, D., Fu, Q., 2007. Redox evolution and mass transfer during serpentinization: An experimental and theoretical study at 200 C, 500 bar with implications for ultramafic-hosted hydrothermal systems at Mid-Ocean Ridges. Geochimica et Cosmochimica Acta, 71(15): 3872-3886.

Sleep, N., Meibom, A., Fridriksson, T., Coleman, R., Bird, D., 2004. H2-rich fluids from serpentinization: geochemical and biotic implications. Proceedings of the National Academy of Sciences, 101(35): 12818-12823.

Syverson, D.D., Tutolo, B.M., Borrok, D.M., Seyfried Jr, W.E., 2017. Serpentinization of olivine at 300° C and 500 bars: an experimental study examining the role of silica on the reaction path and oxidation state of iron. Chemical Geology, 475: 122-134.

Tenailleau, C., Pring, A., Etschmann, B., Brugger, J., Grguric, B. and Putnis, A. 2006. Transformation of pentlandite to violarite under mild hydrothermal conditions. American Mineralogist 91, 706-709.

Van Dyk, J.P., Vegter, N.M., Pistorius, P.C., 2002. Kinetics of ilmenite dissolution in hydrochloric acid. Hydrometallurgy, 65(1): 31-36.

Xia, F., Brugger, J., Chen, G., Ngothai, Y., O'Neill, B., Putnis, A. and Pring, A. 2009. Mechanism and kinetics of pseudomorphic mineral replacement reactions: A case study of the replacement of pentlandite by violarite. Geochimica et Cosmochimica Acta, 73(7), 1945-1969.

Xia, F., Zhou, J., Brugger, J., Ngothai, Y., O'Neill, B., Chen, G. and Pring, A. 2008. Novel route to synthesize complex metal sulfides: Hydrothermal coupled dissolution− reprecipitation replacement reactions. Chemistry of Materials 20, 2809-2817.

Zhao, J., Brugger, J., Ngothai, Y., Pring, A., 2014. The replacement of chalcopyrite by bornite under hydrothermal conditions. American Mineralogist, 99(11-12): 2389-2397.

Zhao, J., Brugger, J., Pring, A., 2019. Mechanism and kinetics of hydrothermal replacement of magnetite by hematite. Geoscience Frontiers, 10(1): 29-41.

Zhao, J., Brugger, J., Xia, F., Ngothai, Y., Chen, G. and Pring, A. 2013. Dissolution-reprecipitation vs. solid-state diffusion: Mechanism of mineral transformations in sylvanite,(AuAg) 2Te4, under hydrothermal conditions. American Mineralogist 98, 19-32.

Zhao, J., Pring, A., 2019. Mineral Transformations in Gold–(Silver) Tellurides in the Presence of Fluids: Nature and Experiment. Minerals, 9(3): 167.

Chapter 2

Fluid compositional control on serpentinisation kinetics and textural evolution

A modified version of this manuscript was submitted for publication to a scientific journal.

Tobias Wengorsch, Andreas Beinlich, Ben Grguric, Andrew Putnis

2.1 Abstract

Hydration of the oceanic lithosphere results in large-scale ultramafic rock serpentinisation with major consequences for rock physical properties, element cycling and generation of distinct geochemical environments. Specific secondary serpentine minerals form in response to the alteration conditions with antigorite generally being the high temperature phase while chrysotile and lizardite form at lower temperature. However, relatively little is known about the influence of fluid composition on the serpentine morphology and its evolution with time during the progress of the serpentinisation reactions. Here we present the results of hydrothermal experiments on the alteration of natural harzburgite and single crystal olivine and enstatite under fluid saturated conditions at 240 °C and autogenous vapor pressure. Textural analyses of our reaction products indicate a systematic relation between fluid salinity and serpentine morphology and/or assemblages of morphologically distinct serpentine phases. Furthermore, the serpentine morphology also varies with the proportion of olivine and orthopyroxene in the starting material. Olivine serpentinisation in pure H_2O results in the formation of lizardite with a transition into conical serpentine together with brucite. The presence of additional orthopyroxene prevents brucite formation and stabilizes polyhedral serpentine together with tabular lizardite. With increasing fluid salinity the serpentine assemblage evolves from polyhedral serpentine + lizardite to lizardite, to lizardite + chrysotile fibres, to serpentine tubes, and finally to cones and fibres. In our experiments, polyhedral serpentine only formed from non-saline solutions, whereas highly saline solutions promoted the transient appearance of proto-serpentine within the first 330 hours of reaction. Furthermore, our results indicate that olivine serpentinisation is enhanced by a factor of ~16 in the presence of pyroxene compared to a monomineralic olivine starting material at fixed reaction time and initial fluid composition. This increase in serpentinisation rate can be linked to the release of Si from pyroxene dissolution as confirmed by additional serpentinisation experiments of monomineralic San Carlos olivine in Si-bearing ± NaCl solutions. This observation highlights a feedback of the

overall phase assemblage on the reactivity of its individual components in composite rocks. The results of our experiments highlight the potential of serpentine morphology to provide insight into the alteration fluid composition and its evolution during serpentinisation. The presence of enstatite increases olivine hydration efficiency and thus implies enhanced serpentinisation of harzburgite compared to dunite and in systems where aqueous silica activity is increased by concomitantly occurring mineral carbonation or at contact zones with mafic and/or felsic rocks.

2.2 Introduction

Fluid–rock interactions in ultramafic systems drive large–scale element cycling, geophysical property changes and rock alteration including serpentinisation, carbonation and weathering of oceanic lithosphere and alpine peridotite (e.g. Beinlich et al., 2018; Beinlich et al., 2012; Klein and McCollom, 2013; Plümper et al., 2014; Plümper et al., 2017; Tominaga et al., 2017; Ulven et al., 2017). Serpentinisation is particularly important for the Earth's hydrosphere–lithosphere water exchange and volatile transport into the mantle through subduction of hydrated oceanic slabs (Rüpke et al., 2004). These processes are unique to Earth and hence of considerable interest for our understanding of the Earth's geodynamic evolution. This is reflected by a vast number of field-based and experimental studies focused on the rates and mechanisms of ultramafic rock hydration. These include, for example, experimental studies on the reactions of H_2O with olivine (e.g. Lafay et al., 2012; Lamadrid et al., 2017; Martin and Fyfe, 1970; McCollom et al., 2016; Wegner and Ernst, 1983) and peridotite (e.g. Allen and Seyfried Jr, 2003; Janecky and Seyfried Jr, 1986; Marcaillou et al., 2011; Ogasawara et al., 2013; Okamoto et al., 2013; Seyfried Jr et al., 2007). For a better understanding of how fast the physicochemical properties of rock change during natural fluid-rock interactions, serpentinisation rates are of particular importance. These are predominantly extrapolated from laboratory experiments and were shown to depend on temperature and grain size of the magmatic precursor (Malvoisin et al., 2012). However, the effect of fluid composition on the serpentinisation rate is less well constrained. Generally, olivine serpentinisation is enhanced in highly alkaline

solutions (Lafay et al., 2012) and may further accelerate in the presence of dissolved Al (Andreani et al., 2013a). These observations are directly applicable to natural serpentinisation systems that are often characterized by elevated pH and the presence of Al-bearing spinel and orthopyroxene. Furthermore, also the fluid salinity is likely to be high during seawater circulation through the ultramafic oceanic lithosphere. According to Malvoisin et al. (2012) the olivine serpentinisation rate is independent of fluid NaCl concentration, whereas Lamadrid et al. (2017) reported an inverse correlation with fluid salinity consistent with low temperature (25 °C) experimental results at low pH (Olsen et al., 2015). In contrast, enstatite dissolution rates increase with fluid salinity (Phillips-Lander et al., 2016). Oelkers and Schott (2001) report that the rate of enstatite dissolution decreases with increasing aMg,aq but is independent of aSi,aq In contrast, forsterite dissolution is unaffected by aSi,aq, but decreases with aMg,aq at above pH of 8.8 (Olsen et al., 2015; Pokrovsky and Schott, 2000). In addition to experiments on monomineralic reactants, few studies have investigated the feedback between concomitantly dissolving minerals in composite starting materials. For example, Ogasawara et al. (2013) and Okamoto et al. (2013) report enhanced reaction kinetics for spatially close olivine and enstatite compared to the pure phases during hydrothermal experiments. In a similar study using a composite olivine-enstatite starting material, Huang et al. (2017b) found that the release of Cr and Al from spinel and pyroxene increases the serpentinisation rate of the olivine. They further concluded that the release of silica from the pyroxene has only negligible effect on the olivine serpentinisation rate, while the presence of quartz seems to inhibit serpentinisation of olivine in alkaline solutions compared to the pure olivine starting material (Oyanagi et al., 2015). Dissolution experiments on serpentine-bearing natural peridotite found dissolution rates that are between two times and two orders of magnitude faster than that of olivine (Van Noort et al., 2013), indicating that serpentine facilitates fluid access into the samples as has also been found in carbonation experiments of similar rocks (Hövelmann et al., 2011). Furthermore, Martin and Fyfe (1970) suggested an additional dependence of reaction progress on

the fluid–rock ratio, which could not be confirmed by later studies (Wegner and Ernst, 1983).

Serpentinisation of ultramafic rock proceeds as a dissolution–precipitation reaction and secondary serpentine ± brucite ± talc ± magnetite form according to their saturation in the fluid and depending on the bulk composition of the system. At low temperature, serpentinisation commonly results in the formation of chrysotile, with rolled up layers, and lizardite, with flat layers. Additional serpentine phases comprise polygonal, polyhedral, and conical serpentine (e.g. Andreani et al., 2007; Baronnet et al., 2007; Normand et al., 2002). The different serpentine habits reflect the misfit between the tetrahedral and octahedral layer due to cation substitution and/or the presence of foreign ions in solution (e.g. Roy and Roy, 1954). Yada and Iishi (1974) studied serpentine morphology after olivine and found morphological changes at high pH controlled by NaOH, but no effect of NaCl. Normand et al. (2002) related the appearance of lizardite, chrysotile, polygonal serpentine and conical serpentine in a single flow-through experiment with water at 300 °C to saturation gradients along the flow path. Malvoisin et al. (2012) reported a change from lizardite as the primary alteration phase to chrysotile for experiments with grain sizes below 5 µm at 300 °C. Polyhedral serpentine has so far only been reported for natural rocks (Andreani et al., 2008; Baronnet et al., 2007; Plümper et al., 2014; Zega et al., 2006), with one unconfirmed observation in experiments by McCollom et al. (2016). The occurrence and composition of natural polyhedral serpentine suggest that it forms during the waning stage of serpentinisation and in the presence of pyroxene, facilitated by the presence of trivalent cations.

Here we present new insight into the effects of alteration fluid composition on serpentinisation kinetics and on the morphology of secondary serpentine phases. We investigated the serpentinisation of natural harzburgite, single crystal olivine and olivine-enstatite mixtures by hydrothermal batch reactor experiments. This approach allowed us to quantify the rates and resulting serpentine morphologies for different fluid and solid compositions.

2.3 Methods

2.3.1 Preparation of solid and fluid reactants

A harzburgite hand specimen sample from Twin Sisters Mountain, Washington State, USA (TS) and single crystals of San Carlos olivine (SC) and enstatite (En) from Tanzania were selected as starting materials for this study. All starting materials were crushed in a tungsten carbide disc mill followed by sieving to obtain powders with the grain size of 50 µm to 100 µm. The powder was then washed in Milli–Q water and dried at 100 °C. The fluid reactants were prepared using Milli–Q water and sodium chloride 99.9 % (AnalaR NORMAPUR). Fluid NaCl concentrations were 0.3 M, 0.6 M and 1.7 M. For experiments with dissolved silica, a 0.04 M Si stock solution was prepared using diluted Na-Silicate solution (Sigma Aldrich, reagent grade) that was titrated neutral pH with diluted hydrochloric acid under constant stirring. No precipitate was observed. The Si-bearing stock solution was further diluted with Milli-Q water to obtain Si concentrations of 4 mM and 0.4 mM. An additional 1.7 M NaCl solution was prepared using the 4 mM Si-bearing solution.

2.3.2 Experimental methods

Thirty eight hydrothermal batch experiments were conducted in stainless steel reactors with 10 ml PTFE liners in a multi stage oven at 240 °C. All sample charges consisted of 100 mg powder and 5 ml fluid and were sealed under air atmosphere. Therefore, the fluid–rock weight ratio was ~50 for all experiments. Duplicate experiments were conducted for the experiments with the Si-bearing starting solution. Fluid saturated conditions were maintained for all experiments. Experiment durations were one to twelve weeks. Reactions were terminated by cooling the reactors in air to ambient temperature within 1.5 hours. Fluids were sampled using a 0.45 µm syringe filter and acidified with 2% nitric acid at a ratio of 1:10. Solid reaction products were removed from the liner, washed in Milli–Q water and dried at 100 °C for 1 hour. Experimental conditions and durations are summarized in Table 2.1.

Table 2.1: Experimental conditions, serpentine morphology and reaction progress

exp. No.	Starting assemblage	Initial fluid composition	Time (h)	Secondary minerals / Serp-morphology	TG_{serp} weight loss (%)	reaction progress (%)
Twin Sisters peridotite						
S-44	TS	H_2O	164	Serpentine / Lz, Phs	0.8	6.2
S-35	TS	H_2O	329	Serpentine / Lz, Phs	2.0	15
S-56	TS	H_2O	475	Serpentine / Lz, Phs	2.6	20
S-33	TS	H_2O	810	Serpentine / Lz, Phs	3.4	26
S-51	TS	H_2O	857	Serpentine / Lz, Phs	*NA*	*NA*
S-46	TS	H_2O	1505	Serpentine / Lz, Phs	4.1	31
S-57	TS	H_2O	1888	Serpentine / Lz, Phs	4.3	33
S-88	TS	0.3 M NaCl	169	Serpentine / Lz	*NA*	*NA*
S-36	TS	0.3 M NaCl	329	Serpentine / Lz	*NA*	*NA*
S-24	TS	0.3 M NaCl	810	Serpentine / Lz	4.1	32
S-29	TS	0.3 M NaCl	1508	Serpentine / Lz	5.2	40
S-58	TS	0.3 M NaCl	1888	Serpentine / Ctl	*NA*	*NA*
S-87	TS	0.6 M NaCl	169	Serpentine / Lz	1.1	8.5
S-37	TS	0.6 M NaCl	329	Serpentine / Lz	1.8	14
S-39	TS	0.6 M NaCl	665	Serpentine / Lz	4.4	34
S-42	TS	0.6 M NaCl	857	Serpentine / Lz	5.1	39
S-47	TS	0.6 M NaCl	1505	Serpentine / Ctl	6.4	49
S-45	TS	1.7 M NaCl	164	Serpentine / Ctl, Pts	0.5	3.8
S-38	TS	1.7 M NaCl	329	Serpentine / Ctl, Pts	1.3	10
S-40	TS	1.7 M NaCl	665	Serpentine / Ctl	4.3	33
S-43	TS	1.7 M NaCl	857	Serpentine / Ctl	6.3	48
S-48	TS	1.7 M NaCl	1505	Serpentine / Ctl	6.7	52
S-94	TS	1.7 M NaCl	2010	Serpentine, Brucite / Ctl	6.5	50
San Carlos olivine						
SC-6	SC	H_2O	857	Serpentine, Brucite / Ctl	1.1	8.5
SC-8	SC	0.3 M NaCl	857	Serpentine, Brucite / Ctl	*NA*	*NA*
SC-9	SC	1.7 M NaCl	857	Serpentine, Brucite / Ctl	0.4	3.1
SE-3	SC	4 mM Si - 3 mM NaCl	836	Serpentine /*NA*	2.2	17
SE-4	SC	4 mM Si - 3 mM NaCl	836	Serpentine /*NA*	2.1	16
SE-5	SC	0.4 mM Si - 0.3 mM NaCl	836	Serpentine /*NA*	0.3	2.3
SE-6	SC	0.4 mM Si - 0.3 mM NaCl	836	Serpentine /*NA*	0.5	3.8
SE-7	SC	4 mM Si -1.7 M NaCl	836	Serpentine /*NA*	1.8	14
SE-8	SC	4 mM Si -1.7 M NaCl	836	Serpentine /*NA*	2.1	16
San Carlos olivine + Enstatite						
M-1	SC/En 80/20	H_2O	832	Serpentine / Lz, Phs	3.2	25
M-2	SC/En 90/10	H_2O	832	Serpentine / Lz, Phs	*NA*	*NA*
M-3	SC/En 95/5	H_2O	832	Serpentine / Ctl	3.2	25
M-4	SC/En 80/20	0.3 M NaCl	832	Serpentine / Lz	3.9	30
M-5	SC/En 90/10	0.3 M NaCl	832	Serpentine / Lz	*NA*	*NA*
M-6	SC/En 95/5	0.3 M NaCl	832	Serpentine / Ctl	3.7	28

TG_{serp} weight loss: % weight loss on the serpentine peak, 400 °C to 700 °
TS: Twin Sisters Dunite
SC: San Carlos olivine
En: Enstatite

Even though all reactors and PTFE liners were carefully closed prior to the experiments, we observe an inverse linear relationship between experiment duration and reactor weight. Long term monitoring indicates that the weight loss is approximately 0.048 g day^{-1}.We attribute this weight loss to H_2O permeation through the PTFE liners, facilitated by the relatively high temperature of our experimental runs.

2.3.3 Analytical methods

TESCAN Integrated Mineral Analyser (TIMA)

The mineral phase map of Twin Sister harzburgite was obtained using the TIMA high resolution Field Emission Scanning Electron Microscope (FESEM), in full liberation mode with 5 µm spatial resolution at the John de Laeter Centre, Curtin University, Australia. The instrument is equipped with four Energy Dispersive Spectrometers (EDS) allowing for rapid data acquisition. Operating conditions were 15 kV acceleration voltage and a beam current of 0.8 nA. The uncertainty of the relative proportions is estimated at 5%.

Raman spectroscopy

Raman spectra of solid reactants and product phases were obtained using a WITec alpha 300RA+ microscope at the Centre for Microscopy, Characterisation and Analysis (CMCA), The University of Western Australia. For serpentine analysis, a 532 nm laser with 50 mW in reflected light geometry with a 2400 grooves mm^{-1} grating was used. Raman spectra were obtained for the low and high wavenumber regions 130–830 cm^{-1} and 3530–3850 cm^{-1}, respectively. Iron oxides were analysed using a 675 nm laser with 1 min acquisition time. Measurements were performed on polished resin mounts. The spectrometer was calibrated using the silica peak at 520.7 cm^{-1}. Cosmic rays were removed with the WITec software Project Four, and spectra were fitted and smoothed using MATLABTM.

Solid phase textural analysis

The surface morphology of run products was characterized by FESEM using a FEI Verios XHR at CMCA. Representative surface images were obtained from grains prepared on SEM stubs with copper tape and platinum coating. Images were acquired using secondary (SE) and backscattered electrons (BSE) at an acceleration voltage of 5 kV and a beam current of 0.1 nA. Additional sections across reaction interfaces were prepared by polishing epoxy mounted solid phases. Mineral abbreviations follow the suggestions made by Whitney and Evans (2010). In addition, we abbreviate polyhedral serpentine as Phs and proto–serpentine as Pts.

Thermogravimetric analysis

Simultaneous Differential Thermal Analysis–Thermogravimetric Analyses (DTA–TGA) of reacted samples were performed on a TA Instruments SDT Q600 at the Department of Chemistry, Curtin University, Australia. Approximately 30 mg of sample was placed in a 110 µl platinum crucible and heated from ambient to 1000 °C at 10 °C min-1 in an air atmosphere flowing at 100 ml min-1. A second empty crucible was used as reference. The temperature scale of the instrument was calibrated using the melting points of indium, tin, zinc, silver and gold. The balance was calibrated over the temperature range and used with alumina mass standards provided by the instrument manufacturer. The heat flow between the pans was calibrated using a sapphire disk provided by the manufacturer. Data is presented as both TGA and DTG (derivative thermogravimetric) curves, the latter of which is the first derivate of the TGA curve. Only one TGA measurement was performed per sample, however duplicate experiments show good reproducibility.

Quantitative solid phase compositional analysis

The chemical composition of solid starting materials and run product phases was determined by Electron Probe Micro Analysis (EPMA) on carbon–coated epoxy mounts using a JEOL JXA 8530F at the University of Münster, Germany and at CMCA. Olivine and pyroxene starting materials were analysed using a spot size of 1

µm and with an acceleration voltage of 20 keV, a 15 nA beam current, and 30 s peak counting time and 5 s for background. The standard materials used were periclase (Mg), corundum (Al), wollastonite (Ca), Durango fluorapatite (P), rutile, Mn-metal (Mn), magnetite (Fe), orthoclase (K) and jadeite (Na). Serpentine was analysed using a spot size of 3 µm, an acceleration voltage of 15 keV, 15 nA beam current, and 10 s peak counting time and 5 s for background. Element maps were acquired at 15 keV and beam current of 40 nA, 0.5 µm step size and 200 ms dwell time. Jadeite, San Carlos olivine, kyanite, hypersthene, rhodonite, fayalite, Cr_2O_3, Co-metal, NiO, sanidine and diopside were used as standard materials for serpentine analysis.

Reactive surface area quantification

The initial surface area of the crushed solid reactant was determined by BET N_2 adsorption on ~1.7 g of TS harzburgite powder (grain size of 50–100 µm) using a TriStar 3000 automated gas adsorption analyser at CSIRO Waterford, Perth, Australia.

Fluid analysis

Fluid sample compositions were analysed by Inductively Coupled Plasma–Optical Emission Spectrometry (ICP–OES) for Al, Ca, Fe, Ni, Mg, Na and Si at LabWest (Perth, Australia). An uncertainty of 15% is estimated for the measurement of Na due to dilution of 1:1000 in experiments with 1.7 M NaCl. In addition, F concentrations were measured by ion–selective electrode analysis as a proxy for PTFE decomposition that may result in HF production and affect reaction kinetics. Fluid pH of TS harzburgite and SC-olivine + En enstatite experiments was determined with litmus paper at ambient temperature and is subject to uncertainty. Fluid pH of experiments with SC-olivine + aqueous silica was measured using Thermo Scientific Orion Star A211 pH meter.

2.4 Results

2.4.1 Solid phases

Composition of the starting material

TIMA phase mapping shows that the Twin Sisters harzburgite starting material is composed of ~83 vol.% olivine and ~15 vol.% enstatite, with additional diopside, tremolite, lizardite, and chromite all accounting to less than 1 vol.% (Fig. 2.1). Both olivine and orthopyroxene in the harzburgite are Mg-rich (xMg = Mg/(Mg + Fe) = 0.92), consistent with their composition in typical mantle peridotite. Orthopyroxene contains diopside lamellae. The crushed TS harzburgite starting material has a BET surface area of 0.44 m^2 g^{-1}.

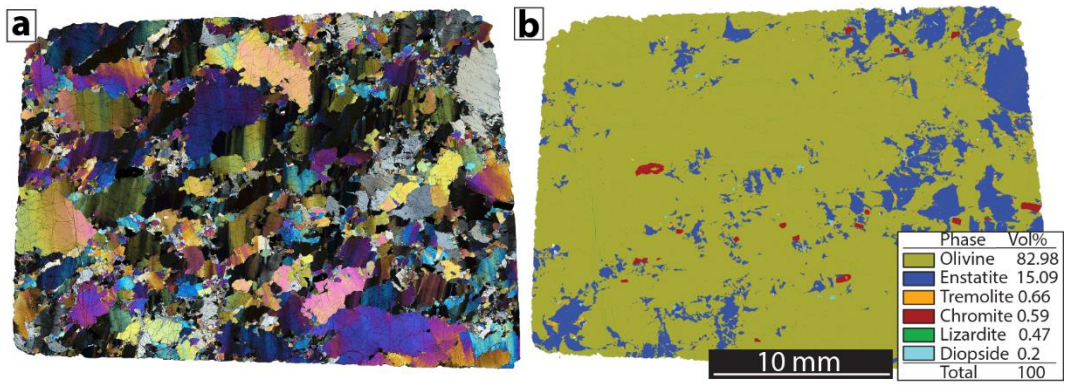

Figure 2.1: (a) Cross polarized map and (b) TIMA phase map of Twin Sisters harzburgite hand specimen.

The chemically homogeneous enstatite (En) starting material is near its endmember composition (xMg = 0.98) and the measured composition of San Carlos olivine is Fo89, consistent with the accepted composition (Jarosewich et al., 1980). All starting materials were free of detectable serpentine, indicating that crushing and cleaning of TS harzburgite effectively removed trace quantities of serpentine that were present in the bulk rock sample prior to the experiments (Table 2.2).

Table 2.2: Chemical composition of starting materials

Sample	Olivine (TS)		Enstatite (TS)		Enstatite (En)		San Carlos	
n	6		4		16		6	
	Mean	SD	Mean	SD	Mean	SD	Mean	SD
SiO_2 wt%	40.81	0.17	57.44	0.19	59.00	0.37	40.33	0.23
Al_2O_3 wt%	0.00	0.00	0.54	0.10	0.64	0.02	0.00	0.00
TiO_2 wt%	0.00	0.00	0.01	0.01	0.02	0.01	0.00	0.01
MgO wt%	50.15	0.34	34.41	0.39	38.48	0.20	47.33	0.86
FeO wt%	7.85	0.26	5.43	0.20	1.41	0.05	10.72	0.93
CaO wt%	0.00	0.00	1.05	0.45	0.08	0.01	0.06	0.01
Na_2O wt%	0.00	0.00	0.00	0.01	0.02	0.01	0.00	0.01
K_2O wt%	0.01	0.01	0.00	0.00	0.00	0.01	0.00	0.00
MnO wt%	0.10	0.02	0.14	0.07	0.04	0.20	0.16	0.05
Total	98.92	0.04	99.03	0.23	99.69	0.51	98.61	0.24
xMg	0.92	0.00	0.92	0.00	0.98	0.00	0.89	0.01
Si	1.00	0.00	1.99	0.00	1.99	0.00	1.01	0.00
Al	0.00	0.00	0.02	0.00	0.03	0.00	0.00	0.00
Ti	0.00	0.00	0.00	0.00	0.00	0.00	0.00	0.00
Mg	1.83	0.01	1.78	0.02	1.94	0.01	1.76	0.02
Fe	0.16	0.01	0.16	0.01	0.04	0.00	0.22	0.02
Ca	0.00	0.00	0.04	0.02	0.00	0.00	0.00	0.00
Na	0.00	0.00	0.00	0.00	0.00	0.00	0.00	0.00
K	0.00	0.00	0.00	0.00	0.00	0.00	0.00	0.00
Mn	0.00	0.00	0.00	0.00	0.00	0.00	0.00	0.00
Total	3.00	0.00	4.00	0.00	4.00	0.00	2.99	0.00
Oxygen	4.00		6.00		6.00		4.00	

Reaction product characterization

Serpentine was confirmed as the dominant reaction product of all experiments (Fig. 2.2). Cross sections through reaction products that were mounted in epoxy indicate an average rim thickness of serpentine around olivine of ~5 µm and ~10 µm around enstatite for experiment durations of ~ 850 hours. Raman spectra of serpentine phases show distinct peaks near ~230 cm^{-1}, ~385 cm^{-1} and ~690 cm^{-1} that are consistent with the reported positions for serpentine minerals (e.g. Petriglieri et al., 2015; Wang et al., 2015). However, the exact positions of Raman peaks in the low and high wavenumber regions systematically shift with reactive fluid composition and morphology. Serpentine peak positions from experiments with 0.6 M NaCl matched those reported for lizardite (Petriglieri et al., 2015) (Fig. 2.2c).

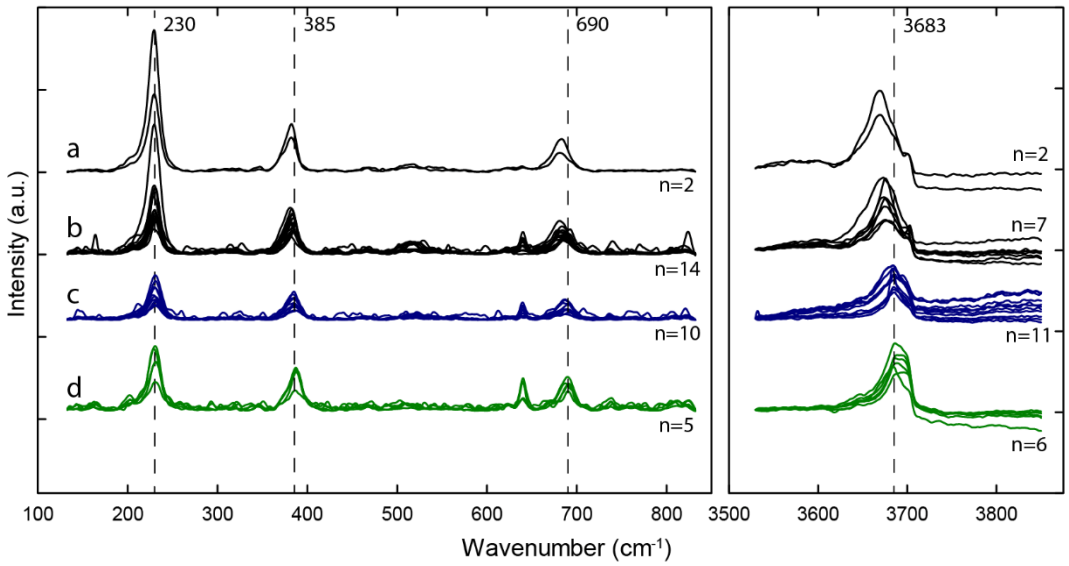

Figure 2.2: Raman spectra for TS harzburgite experiments arranged by observed surface morphology. (a and b) Lizardite and polyhedral morphology. (c) Lizardite. (d) Serpentine cones and tubes. Peak positions for lizardite are marked at 230, 385, 690, 3683 cm-1. The epoxy resin contributes the peak at 640 cm-1.

In comparison, experiments in H_2O resulted in a slight shift to lower values for the 385 cm^{-1} and 690 cm^{-1} peaks (Fig. 2.2a and b), whereas experiments at 1.7 M NaCl produced a peak shift towards higher values of the 385 cm^{-1} peak, consistent with peak position for chrysotile (Fig. 2.2d). OH–stretching vibrations of serpentine formed in H_2O show the strongest peak at ~3675 cm^{-1} with a shoulder at ~3683 cm^{-1} and a weak additional peak at ~3703 cm^{-1}. Some spectra of serpentine from H_2O experiments showed a shift of the strongest peak to ~3668 cm^{-1} (Fig. 2.2a). For serpentinite formed from 0.6 M NaCl solution, the peaks shifted to ~3684 cm^{-1} and ~3704 cm^{-1}, respectively (Fig. 2.2c). Serpentine formed in the 1.7 M NaCl solution formed a broad peak from ~3684 cm^{-1} to 3703 cm^{-1} (Fig. 2.2d). The characteristic Raman peak for lizardite at 3983 cm^{-1} is most pronounced for tabular serpentine (Fig. 2.7a), whereas the assemblage polygonal serpentine, cones and chrysotile is characterized by peak broadening (3683 cm^{-1} to 3698 cm^{-1}) (Petriglieri et al., 2015). Conversely, tabular and polyhedral serpentine formed in H_2O show a Raman peak shift to ~3668 cm^{-1} and 3675 cm^{-1}. In contrast, Andreani et al. (2008) reported that polyhedral serpentine cannot easily distinguished from lizardite on the basis of its Raman spectrum. Additional brucite formed only in experiments with olivine and Si-free solutions, with

one exception for the most reacted TS harzburgite sample in 1.7 M NaCl after ~2000 hours. The Raman spectra of oxides phases (n = 50) formed in experiments between ~330 and ~1900 hours are consistent with hematite (Fig. 2.3). Hematite is present in serpentine rims around olivine but is absent from serpentine rims around enstatite.

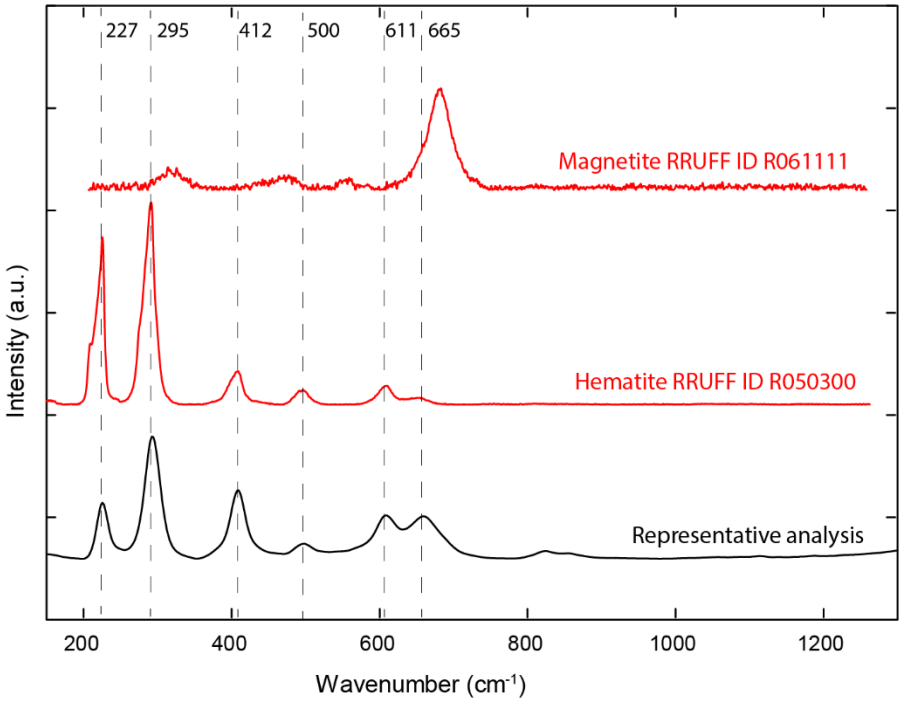

Figure 2.3: Representative Raman spectra of ~50 analysis for iron oxides in Twin Sisters experiments for experimental durations from 329 h to 1888 h (black) showing good agreement with reported spectra for hematite (red, bottom). Magnetite spectra is given for comparison (red, top).

2.4.2 Serpentine morphology

Serpentinisation in H_2O

Serpentinisation experiments in H_2O were conducted using TS harzburgite, SC olivine and SC olivine together with different proportions of orthopyroxene to systematically investigate the influence of starting material composition on reaction progress and serpentine morphology. Serpentinisation of TS harzburgite formed stacks of tabular lizardite (<500 nm thickness) together with polyhedral serpentine (Fig. 2.4). Polyhedral serpentine formed in dissolution cavities of partly reacted orthopyroxene (Fig. 2.5) and ranges in diameter between 0.5 µm and 3 µm. The grain size of polyhedral serpentine correlates with experiment duration (Fig. 2.4).

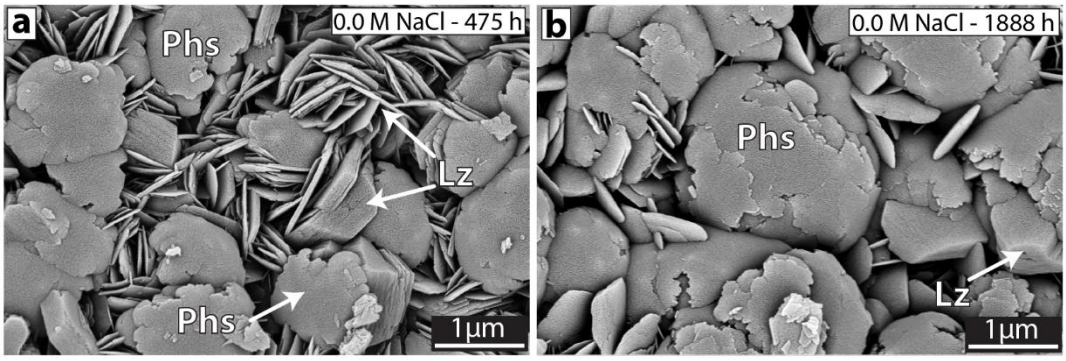

Figure 2.4: Morphology of serpentine formed from TS harzburgite during reaction in NaCl free H_2O. (a) BSE image showing thin stacked sheets of tabular lizardite (Lz) together with polyhedral serpentine (Phs) after reaction for 475 hours. (b) Same experiment as shown in (a) after 1888 hours reaction time. Polyhedral serpentine exhibits increased grain size. Listed NaCl concentration was measured at the completion of the respective experiment.

In contrast, serpentinisation of pure SC olivine resulted in the formation of brucite and lizardite, the latter displaying a transition into conical serpentine (chrysotile) exhibiting triangular shaped layers (Fig. 2.6a). Addition of 5 wt.% enstatite to the SC olivine resulted also in the formation of conical serpentine but suppressed brucite formation. Serpentinisation of SC olivine with 10 wt.% enstatite resulted in tabular and polyhedral serpentine similar to the serpentine formed from TS harzburgite (Fig. 2.6b). Serpentine formed from SC olivine with 20 wt.% enstatite consists of ~10 nm thin sheets (Fig. 2.6c).

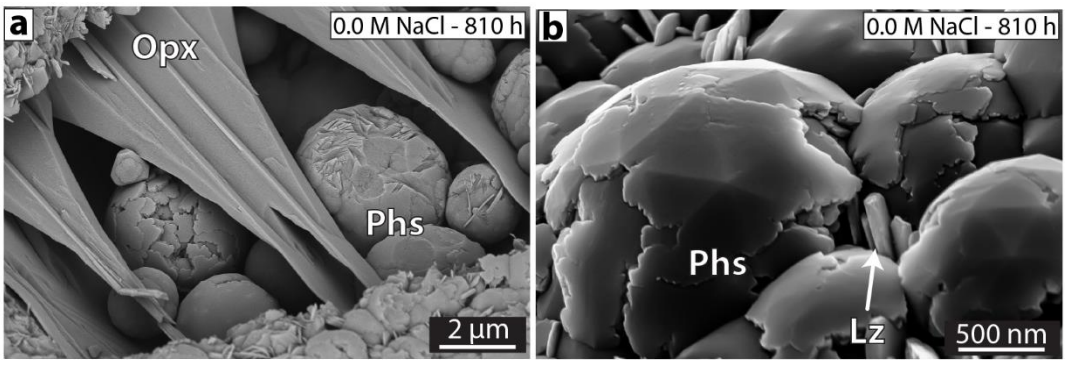

Figure 2.5: Morphology of serpentine formed from TS harzburgite during reaction in NaCl free H_2O. (a) Polyhedral serpentine in dissolution cavities of enstatite, exposed due to broken-off reaction rim during sample preparation. (b) High magnification SE image of a typical intergrowth of polyhedral serpentine and tabular lizardite, exhibiting characteristic facets for polyhedral serpentine. Listed NaCl concentration was measured at the completion of the respective experiment.

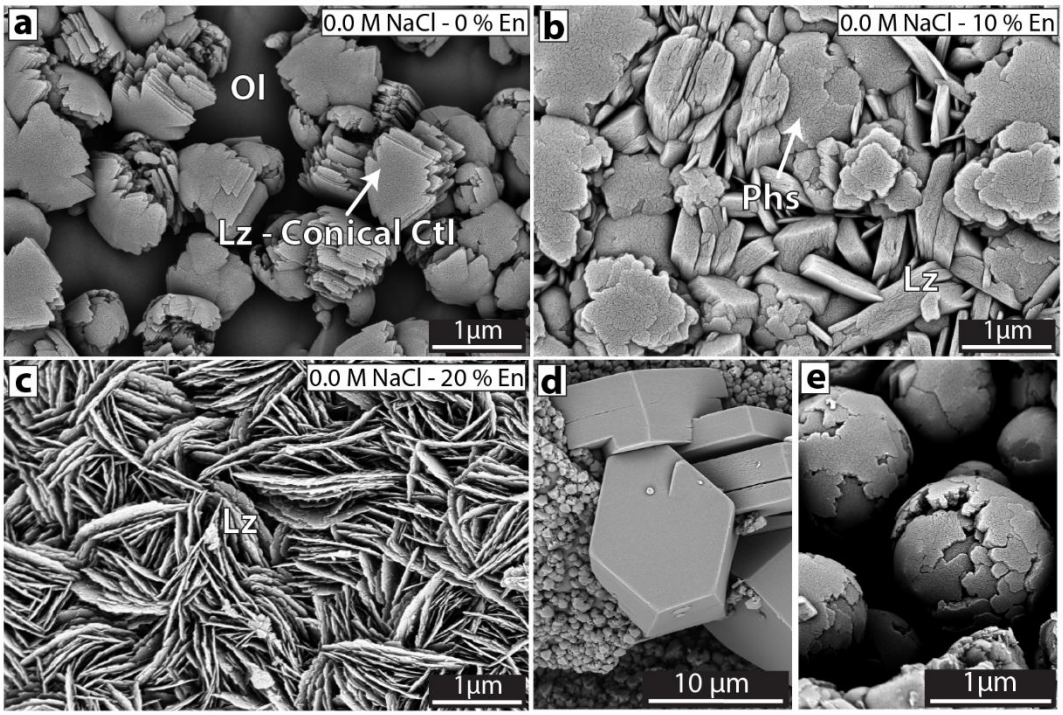

Figure 2.6: (a – c) Representative surface morphology of serpentine formed in NaCl free H_2O after reaction for 832 hours with SC olivine and different proportions of additional enstatite. (a) Experiments on pure SC olivine formed a thin coating of serpentine with transitioning morphology from lizardite to conical serpentine and large crystals of brucite (d). (b) Formation of lizardite and spheres of polyhedral serpentine in cavities (e) from SC olivine together with 10 wt.% enstatite. (c) Thin sheets of lizardite formed from SC olivine together with 20 wt.% enstatite. Listed NaCl concentration was measured at the completion of the respective experiment.

Serpentinisation in NaCl solution

Serpentinisation experiments in NaCl solution were done with initial concentrations of 0.3 M, 0.6 M and 1.7 M and with TS harzburgite, SC olivine and SC olivine–enstatite composite starting materials. Experiments on TS harzburgite with initial concentrations of 0.3 M and 0.6 M NaCl resulted in relatively similar serpentine morphology but at different reaction durations. Generally, serpentine in these experiments is dominated by tabular lizardite together with isolated chrysotile fibres of approximately 10 nm in diameter (Fig. 2.7a). Individual serpentine stacks are thicker (~300 nm) than those formed in experiments in H_2O. In longer runs we observe the formation of additional serpentine tubes (~75 nm in diameter), commencing at ~1900 hours in experiments with final Na concentrations of 1.1 M (0.3 M NaCl starting solution) (Fig. 2.4b and c) and ~1500 hours in experiments with final Na concentrations of 1.4 (0.6 M NaCl starting solution) that also formed additional serpentine cones (Fig. 2.7d).

Serpentinisation of SC olivine in 0.3 M NaCl solution precipitated small serpentine cones and tubes of ~0.3 µm length together with brucite (Fig. 2.8a). Serpentine cones develop from the curved ends of conical chrysotile (Figs 2.6a and 2.8b). Addition of 5 wt.% enstatite resulted in the same serpentine morphology as the experiments on pure SC olivine but brucite was absent. Lizardite formed from SC olivine with 10 wt.% and 20 wt.% enstatite and shows a tabular morphology similar to that formed from TS harzburgite. Individual lizardite sheets become increasingly irregular for higher enstatite concentrations (Fig. 2.8c and d).

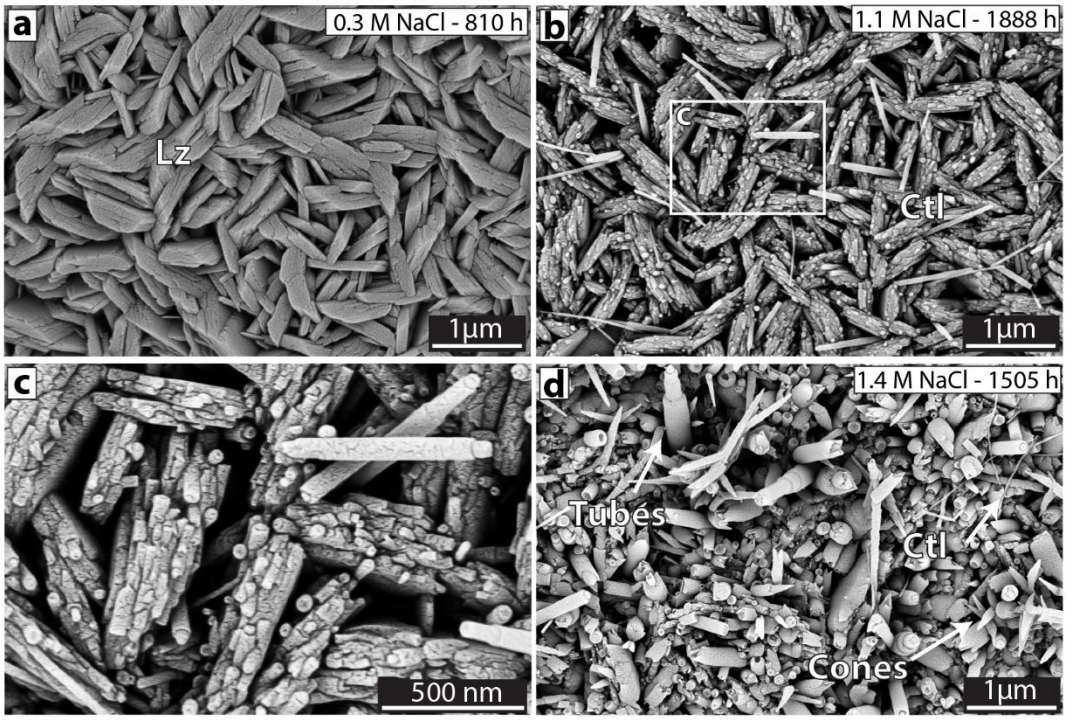

Figure 2.7: BSE images showing the morphology of serpentine formed from TS harzburgite during reaction with initial 0.3 M and 0.6 M NaCl solution. (a) Lizardite as observed after 810 hours in 0.3 M NaCl solution. Note that chrysotile fibres were present, but scarce, for this morphology and not shown in this image; (b and c) Same experiment as shown in (a) after 1888 hours showing the formation of cylindrical chrysotile with preservation of the former lizardite crystal shape. (c) Zoom-in on morphological details from (b). (d) Formation of chrysotile tubes, cones and fibres in 0.6 M NaCl solution after 1505 h reaction time. Note that experiments with durations < 1505 h in 0.6 M initial NaCl yielded lizardite with a similar morphology as shown in (a). Listed NaCl concentration was measured at the completion of the respective experiment.

The reaction of TS harzburgite in 1.7 M NaCl solution formed polygonal serpentine and serpentine tubes (~200 nm in diameter). Furthermore, experiments terminated after ~170 and ~330 hours (final Na concentrations: 1.4 M and 1.5 M) show an additional fine-grained phase resembling proto-serpentine (Fig. 2.9a) (Andreani et al., 2008; Lafay et al., 2016). These short-term experiments also indicate that the serpentine tubes grew ~2 µm between ~170 and ~330 hours. Run products recovered at ~1500 hours (final Na concentration: 2.5 M) are dominated by serpentine cones and tubes (~100 nm in diameter) together with isolated fibres but without proto-serpentine (Fig. 2.9b).

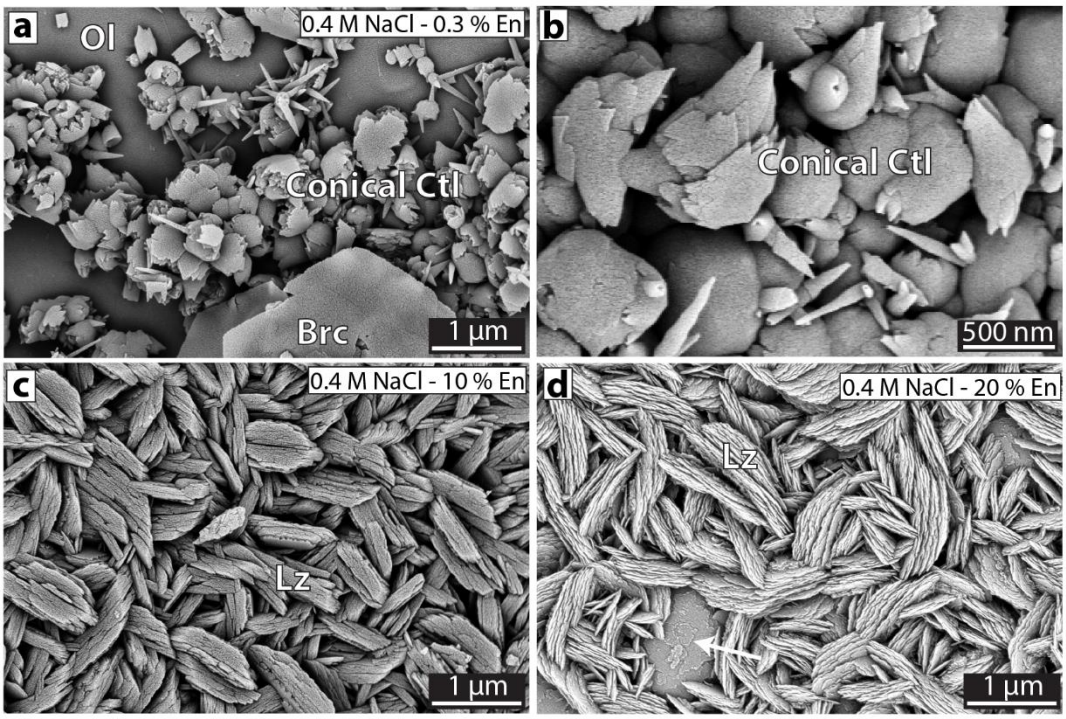

Figure 2.8: BSE images showing representative surface morphologies of serpentine precipitated from a 0.3 M NaCl starting solution after 832 hours reaction time using SC olivine together with different enstatite proportions. (a) Experiments on pure SC olivine form a thin layer of conical serpentine and large but thin crystals of brucite. (b) Same experiment as in (a) showing triangular sheets of conical serpentine that develop into cones. (c) Lizardite formed in experiments with 10 wt.% enstatite in the starting material. (d) Experiments with 20 wt.% enstatite produce a lizardite morphology similar to that shown in (c) but with larger spacing between individual sheets. The arrow points at the olivine surface. Listed NaCl concentration was measured at the completion of the respective experiment.

The analysis of cross sections through epoxy mounted run products indicates complete replacement of enstatite from the starting material after ~2000 hours reaction duration, which coincides with the appearance of brucite. (Fig. 2.10). Reaction of pure SC olivine in 1.7 M NaCl solution resulted in the same serpentine morphologies as the experiments with 0.3 M NaCl solution (final Na concentrations: 0.4 and 1.7 M) but with a higher proportion of serpentine cones and short tubes and additional brucite. Furthermore, experiment durations longer than ~330 h in 1.7 M NaCl solution resulted in strong curvature and delamination of the serpentine rims from the primary mineral substrate (Fig. 2.11a and b) for experiments on TS harzburgite. In contrast, run products from experiments with lower salinity resulted in serpentine formation directly on reaction surfaces (e.g., Fig. 2.11c and d).

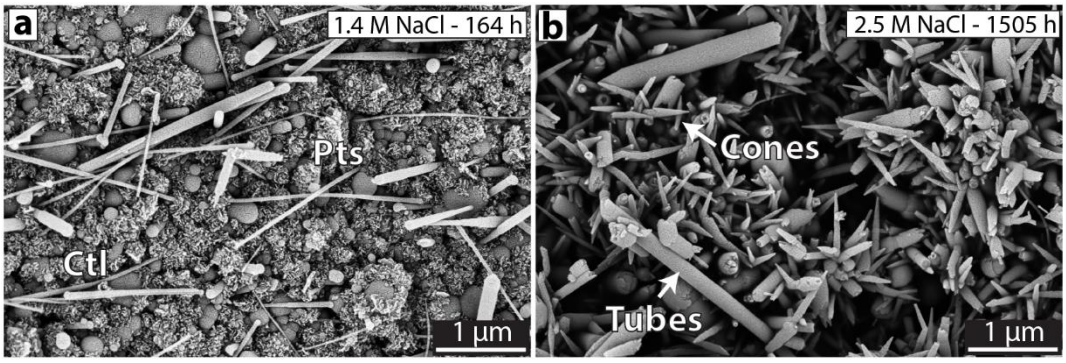

Figure 2.9: BSE images showing the morphology of serpentine formed from TS harzburgite reacted with 1.7 M NaCl starting solution. (a) Chrysotile tubes and fibres, polygonal serpentine and proto–serpentine (Pts) after 164 hours of reaction. (b) After 1505 hours of reaction, serpentine cones and tubes dominate the assemblage with minor chrysotile fibres. Listed NaCl concentration was measured at the completion of the respective experiment.

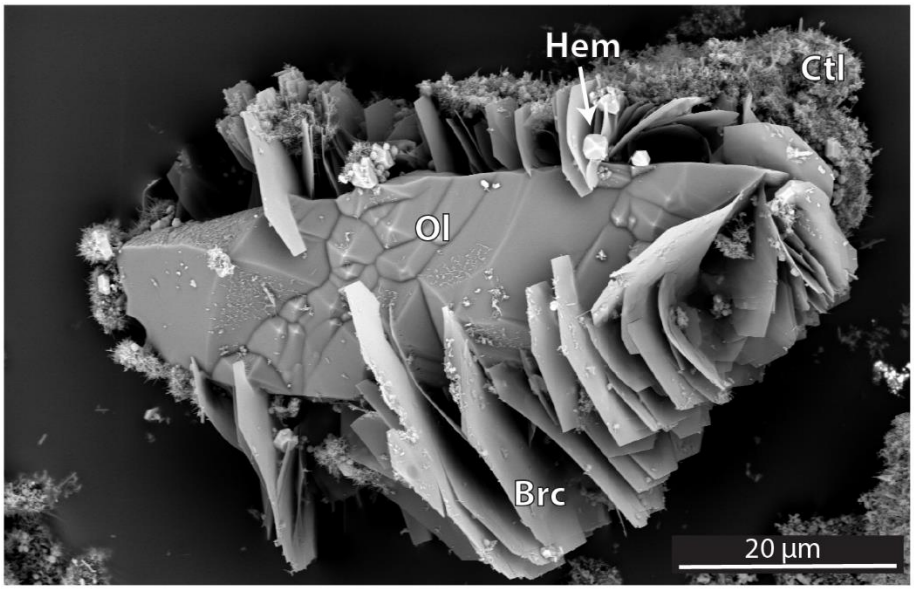

Figure 2.10: BSE image of brucite formed from TS harzburgite after 2010 hours in 1.7 M NaCl starting solution. Olivine is replaced by an assemblage consisting of thin flakes of brucite, hematite and chrysotile.

2.4.3 Serpentine composition

The composition of secondary serpentine was investigated by EPMA on polished epoxy mounts exposing sections across the interface between the precursor olivine/enstatite and the serpentine rim. Within these cross sections, BSE contrast variations correlate with concentrations of Al_2O_3 and FeO, thus defining compositionally distinct zones that are more strongly developed in serpentine after enstatite (Fig. 2.12). These different zones can be described as an inner zone, an outer zone and a thin rim between the outer zone and the epoxy. The inner zone shows gradually increasing FeO and decreasing in Al_2O_3 concentrations from the interface with the precursor silicate toward the outer serpentine zone. The transition from the inner to the outer zone is marked by a sharp decrease in FeO and a slight increase in Al_2O_3 concentrations. The rim between the outer zone and the epoxy is too thin to obtain reliable quantitative compositional data but shows a similar BSE contrast as the inner zone. The apparently low concentrations of the rim shown in the EPMA element maps (Fig. 2.12b) may be due to the presence of epoxy filled porosity. In contrast to FeO and Al_2O_3, the concentrations of SiO_2 and MgO remain invariant across the two serpentine zones.

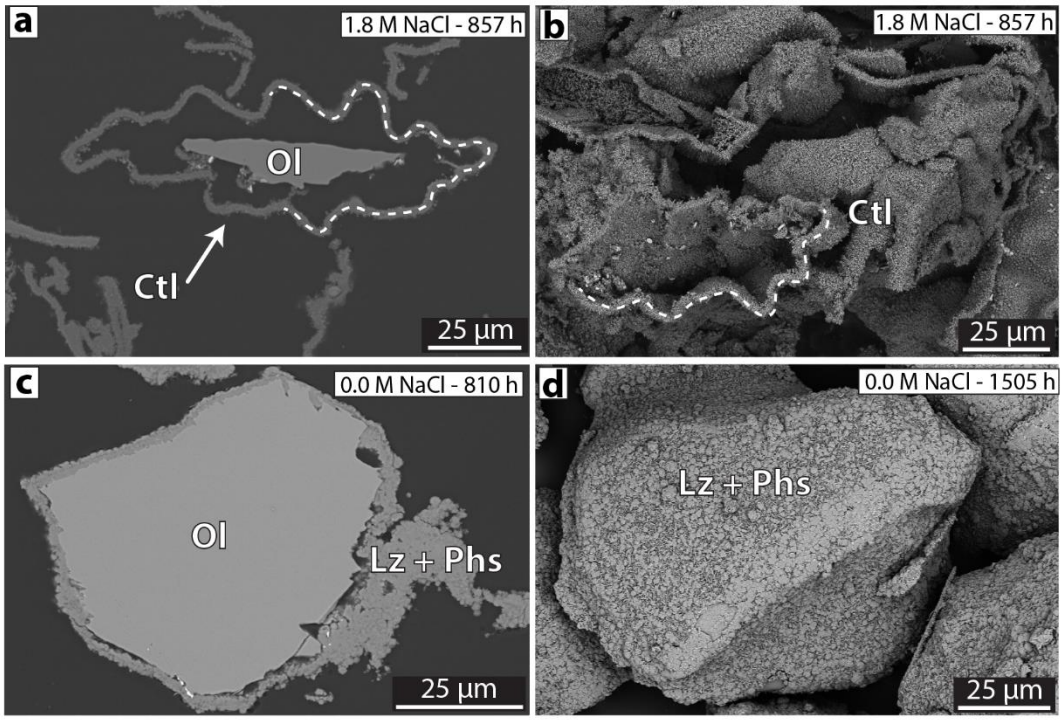

Figure 2.11: BSE images of serpentine morphology with 1.7 M NaCl starting solution (a and b) and NaCl free runs (c and d) formed from TS harzburgite. (a) Cross section and (b) surface morphology of serpentine after 857 h (also see Fig. 2.9b for higher magnification). Serpentine exhibits a distinctive curvature (dashed line) and delaminates from the primary olivine at experiment durations > 329 hours. (c) Cross section and (d) surface morphology of serpentine in NaCl free runs, after 810 h and 1505 h, respectively. Lizardite and polyhedral (see also Fig. 2.4 for higher magnification) form a coherent layer of variable thickness on the olivine surface. Listed NaCl concentration was measured at the completion of the respective experiment.

Single spot compositions from the inner and outer layers are consistent with the stoichiometry of serpentine but show a tendency to lower totals (Table 2.3, 2.4 and 2.5). Within the analytical uncertainty, serpentine composition is independent of experiment duration and fluid salinity. However, the serpentine composition reflects the composition of the starting assemblage. For example, Si concentration increases with enstatite content in the starting assemblage. Additionally, the serpentine xMg is higher in experiments using SC olivine + En compared to experiments using the TS harzburgite (Table 2.3, 2.4 and 2.5).

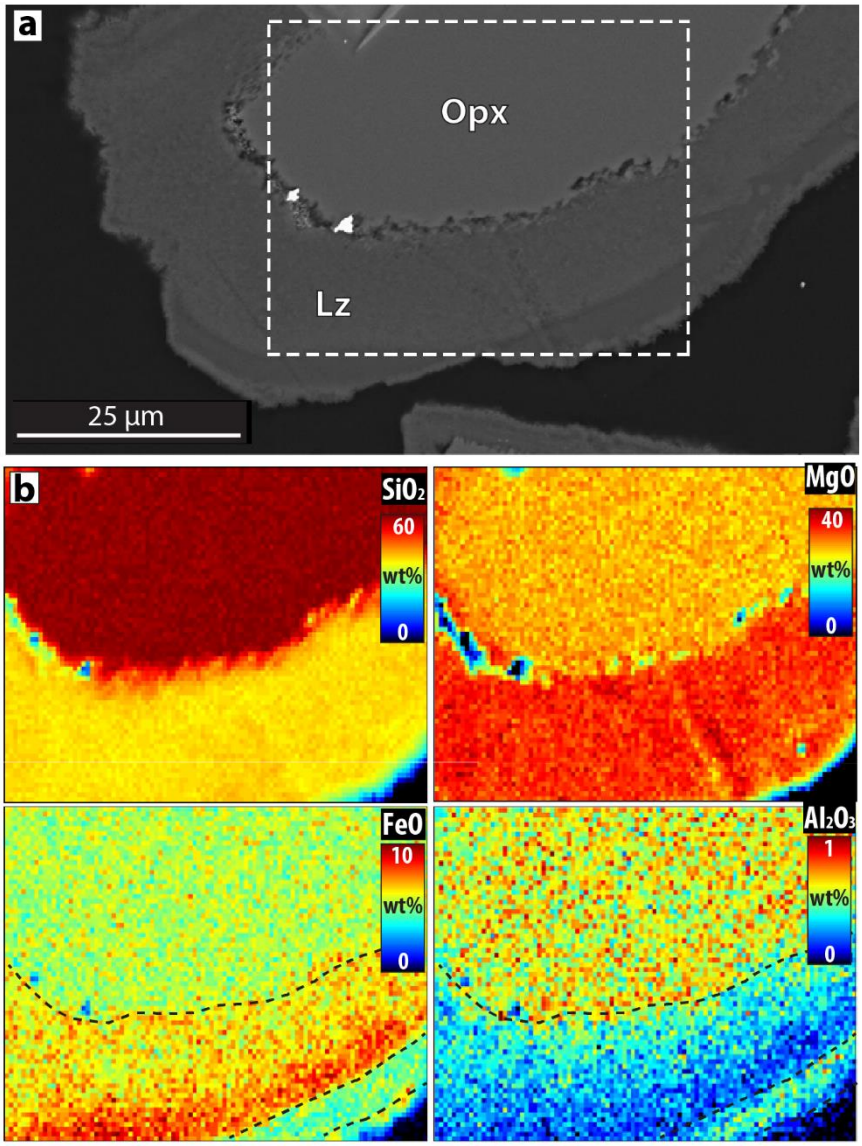

Figure 2.12: BSE image and quantitative element distribution maps of a serpentine reaction rim (lizardite morphology) around enstatite that reacted in 0.6 M NaCl starting solution for ~665 h hours. (a) The z–contrast variation in the serpentine rim defines three compositionally distinct zones. The dashed rectangle outlines the area used for element distribution mapping in (b). The bright spots are gold residues of a previous coating. (b) Element distribution maps for Si, Mg, Fe and Al. The dashed lines in the Fe and Al maps highlight the boundaries between different zones.

Table 2.3: Chemical composition of serpentine after olivine in experiments with Twin Sisters harzburgite

	Serpentine after olivine								Serpentine after olivine						Serpentine after olivine					
Solution	*0 M NaCl initial*								*0.6 M NaCl initial*						*1.7 M NaCl initial*					
Time (h)	*475*		*857*		*1505*		*1888*		*665*		*857*		*1505*		*665*		*857*		*1505*	
n	1		2		7		8		8		12		5		9		4		6	
	Mean	SD	Mean	SD	Mean	SD	Mean	SD	Mean	SD	Mean	SD	Mean	SD	Mean	SD	Mean	SD	Mean	SD
SiO_2 wt%	39.27	-	41.36	2.12	39.92	1.15	39.01	0.19	38.90	0.51	38.99	0.45	39.58	1.95	39.55	1.73	32.50	2.92	32.81	1.56
Al_2O_3 wt%	0.06	-	0.07	0.04	0.06	0.02	0.06	0.00	0.10	0.03	0.09	0.01	0.09	0.01	0.29	0.53	0.11	0.03	0.12	0.02
TiO_2 wt%	0.01	-	0.00	0.00	0.01	0.01	0.00	0.00	0.01	0.01	0.00	0.01	0.01	0.01	0.01	0.01	0.01	0.01	0.01	0.01
MgO wt%	38.33	-	38.12	2.31	38.53	0.98	39.78	0.70	37.29	0.55	37.69	0.99	36.48	2.41	35.50	2.42	30.29	2.63	30.07	2.06
FeO wt%	6.30	-	5.01	1.98	6.97	1.55	7.44	0.74	5.87	0.75	6.07	0.75	5.84	1.89	4.97	1.40	4.58	0.69	4.46	0.97
CaO wt%	0.04	-	0.07	0.03	0.06	0.01	0.05	0.00	0.06	0.02	0.05	0.01	0.05	0.01	0.04	0.02	0.04	0.01	0.04	0.01
Na_2O wt%	0.03	-	0.00	0.00	0.00	0.01	0.00	0.00	0.01	0.01	0.00	0.01	0.01	0.01	0.01	0.01	0.02	0.01	0.01	0.01
K_2O wt%	0.01	-	0.00	0.00	0.01	0.00	0.00	0.00	0.00	0.00	0.00	0.00	0.00	0.00	0.00	0.00	0.00	0.00	0.00	0.00
MnO wt%	0.12	-	0.09	0.04	0.09	0.05	0.10	0.01	0.08	0.03	0.08	0.02	0.05	0.03	0.13	0.06	0.08	0.03	0.06	0.02
Total	84.63	-	85.03	2.57	86.09	1.18	86.83	0.19	82.68	1.32	83.42	1.00	82.50	2.64	80.71	3.24	67.85	5.76	67.87	4.40
xMg	0.92	-	0.92	0.03	0.91	0.02	0.91	0.01	0.92	0.01	0.92	0.01	0.92	0.03	0.93	0.02	0.92	0.01	0.92	0.01
Si	1.94	-	1.94	0.04	1.95	0.03	1.90	0.00	1.96	0.02	1.95	0.03	1.99	0.03	2.02	0.06	1.99	0.04	2.00	0.03
Al	0.00	-	0.00	0.00	0.00	0.00	0.00	0.00	0.00	0.00	0.00	0.00	0.00	0.00	0.01	0.01	0.00	0.00	0.00	0.00
Ti	0.00	-	0.00	0.00	0.00	0.00	0.00	0.00	0.00	0.00	0.00	0.00	0.00	0.00	0.00	0.00	0.00	0.00	0.00	0.00
Mg	2.83	-	2.76	0.07	2.80	0.03	2.88	0.03	2.80	0.03	2.81	0.05	2.74	0.06	2.71	0.09	2.76	0.09	2.74	0.06
Fe	0.26	-	0.21	0.09	0.28	0.07	0.30	0.03	0.25	0.03	0.26	0.03	0.25	0.08	0.21	0.06	0.23	0.03	0.23	0.04
Ca	0.00	-	0.00	0.00	0.00	0.00	0.00	0.00	0.00	0.00	0.00	0.00	0.00	0.00	0.00	0.00	0.00	0.00	0.00	0.00
Na	0.00	-	0.00	0.00	0.00	0.00	0.00	0.00	0.00	0.00	0.00	0.00	0.00	0.00	0.00	0.00	0.00	0.00	0.00	0.00
K	0.00	-	0.00	0.00	0.00	0.00	0.00	0.00	0.00	0.00	0.00	0.00	0.00	0.00	0.00	0.00	0.00	0.00	0.00	0.00
Mn	0.01	-	0.00	0.00	0.00	0.00	0.00	0.00	0.00	0.00	0.00	0.00	0.00	0.00	0.01	0.00	0.00	0.00	0.00	0.00
Total	5.06	-	4.99	0.04	5.05	0.03	5.10	0.00	5.04	0.02	5.05	0.03	5.00	0.03	4.97	0.06	5.01	0.04	4.99	0.03
Oxygen	7		7		7		7		7		7		7		7		7		7	

Table 2.4: Chemical composition of serpentine after pyroxene in experiments with Twin Sisters harzburgite

	Serpentine after pyroxene								Serpentine after pyroxene						Serpentine after pyroxene					
Solution	*0 M NaCl initial*								*0.6 M NaCl initial*						*1.7 M NaCl initial*					
Time (h)	*475*		*857*		*1505*		*1888*		*665*		*857*		*1505*		*665*		*857*		*1505*	
n	5		9		10		11		3		5		9		8		8		8	
	Mean	SD	Mean	SD	Mean	SD	Mean	SD	Mean	SD	Mean	SD	Mean	SD	Mean	SD	Mean	SD	Mean	SD
SiO_2 wt%	39.29	1.11	39.02	0.80	39.53	1.21	38.78	1.11	38.40	0.43	38.44	0.37	38.66	0.72	38.17	0.72	33.88	2.98	37.46	1.13
Al_2O_3 wt%	0.19	0.06	0.19	0.07	0.27	0.14	0.31	0.15	0.27	0.07	0.27	0.07	0.19	0.05	0.19	0.06	0.16	0.04	0.15	0.03
TiO_2 wt%	0.01	0.01	0.01	0.01	0.01	0.01	0.02	0.01	0.02	0.01	0.02	0.00	0.01	0.01	0.01	0.01	0.00	0.01	0.01	0.01
MgO wt%	38.11	1.48	38.49	1.27	37.52	1.61	38.29	0.93	37.62	0.37	37.41	0.40	37.55	0.94	36.19	1.31	30.77	4.67	35.73	2.47
FeO wt%	7.12	1.57	7.60	1.31	6.82	1.37	7.31	1.36	6.87	0.43	6.72	0.21	6.94	1.39	6.15	0.82	6.39	1.93	5.73	0.46
CaO wt%	0.05	0.02	0.03	0.01	0.16	0.21	0.11	0.07	0.06	0.01	0.07	0.01	0.05	0.02	0.06	0.03	0.05	0.02	0.04	0.01
Na_2O wt%	0.00	0.00	0.00	0.00	0.00	0.00	0.00	0.01	0.00	0.00	0.02	0.01	0.02	0.02	0.01	0.01	0.03	0.02	0.01	0.01
K_2O wt%	0.01	0.00	0.00	0.00	0.01	0.01	0.00	0.00	0.00	0.01	0.00	0.00	0.00	0.00	0.00	0.00	0.00	0.00	0.00	0.00
MnO wt%	0.19	0.03	0.15	0.03	0.14	0.04	0.16	0.03	0.15	0.04	0.15	0.03	0.14	0.03	0.11	0.04	0.12	0.08	0.11	0.04
Total	85.09	0.46	85.83	1.73	84.69	2.08	85.49	1.14	83.56	0.79	83.29	0.89	83.78	1.40	81.17	1.57	71.63	6.47	79.46	3.90
xMg	0.91	0.02	0.90	0.02	0.91	0.02	0.90	0.02	0.91	0.01	0.91	0.00	0.91	0.02	0.91	0.01	0.89	0.04	0.92	0.00
Si	1.94	0.05	1.92	0.04	1.96	0.04	1.92	0.04	1.93	0.01	1.94	0.00	1.94	0.04	1.97	0.05	1.99	0.05	1.97	0.04
Al	0.01	0.00	0.01	0.00	0.01	0.00	0.01	0.00	0.01	0.00	0.01	0.00	0.01	0.00	0.01	0.00	0.01	0.00	0.00	0.00
Ti	0.00	0.00	0.00	0.00	0.00	0.00	0.00	0.00	0.00	0.00	0.00	0.00	0.00	0.00	0.00	0.00	0.00	0.00	0.00	0.00
Mg	2.80	0.10	2.82	0.05	2.77	0.06	2.82	0.05	2.82	0.01	2.81	0.00	2.81	0.05	2.78	0.07	2.68	0.15	2.79	0.07
Fe	0.29	0.07	0.31	0.05	0.28	0.06	0.30	0.06	0.29	0.02	0.28	0.01	0.29	0.06	0.26	0.03	0.32	0.12	0.25	0.01
Ca	0.00	0.00	0.00	0.00	0.01	0.01	0.01	0.00	0.00	0.00	0.00	0.00	0.00	0.00	0.00	0.00	0.00	0.00	0.00	0.00
Na	0.00	0.00	0.00	0.00	0.00	0.00	0.00	0.00	0.00	0.00	0.00	0.00	0.00	0.00	0.00	0.00	0.00	0.00	0.00	0.00
K	0.00	0.00	0.00	0.00	0.00	0.00	0.00	0.00	0.00	0.00	0.00	0.00	0.00	0.00	0.00	0.00	0.00	0.00	0.00	0.00
Mn	0.01	0.00	0.01	0.00	0.01	0.00	0.01	0.00	0.01	0.00	0.01	0.00	0.01	0.00	0.00	0.00	0.01	0.00	0.00	0.00
Total	5.06	0.05	5.08	0.04	5.04	0.04	5.08	0.04	5.06	0.01	0.00	0.00	5.06	0.04	5.03	0.05	5.01	0.05	5.03	0.04
Oxygen	7		7		7		7		7		7		7		7		7		7	

Table 2.5: Chemical composition of serpentine after 832 h from mixtures of San Carlos olivine and enstatite (En)

	Serpentine						Serpentine					
Solution	*0 M NaCl initial*						*0.3 M NaCl initial*					
Enstatite	*5 wt%*		*10 wt%*		*20 wt%*		*5 wt%*		*10 wt%*		*20 wt%*	
n	4		6		7		6		4		2	
	Mean	SD	Mean	SD	Mean	SD	Mean	SD	Mean	SD	Mean	SD
SiO_2 wt%	38.49	1.45	41.10	1.03	42.45	0.62	36.24	1.75	39.88	0.92	40.71	1.70
Al_2O_3 wt%	0.29	0.17	0.32	0.08	0.76	0.21	0.18	0.05	0.29	0.12	0.29	0.04
TiO_2 wt%	n.a.	n.a.	n.a.	n.a.	n.a.	n.a.	n.a.	n.a.	n.a.	n.a.	n.a.	n.a.
MgO wt%	38.66	1.10	39.37	0.58	35.44	3.38	35.53	1.77	37.68	0.78	37.72	1.40
FeO wt%	5.36	2.74	2.61	0.53	4.05	3.39	5.65	1.63	3.80	2.09	3.01	0.15
CaO wt%	0.03	0.00	0.08	0.02	0.07	0.07	0.02	0.01	0.04	0.04	0.03	0.00
Na_2O wt%	n.a.	n.a.	n.a.	n.a.	n.a.	n.a.	n.a.	n.a.	n.a.	n.a.	n.a.	n.a.
K_2O wt%	n.a.	n.a.	n.a.	n.a.	n.a.	n.a.	n.a.	n.a.	n.a.	n.a.	n.a.	n.a.
MnO wt%	0.08	0.01	0.05	0.01	0.06	0.06	0.05	0.02	0.08	0.08	0.07	0.01
Total	82.92	0.65	83.53	1.42	82.81	0.91	77.68	3.50	81.77	1.05	81.82	2.85
xMg	0.93	0.04	0.96	0.01	0.94	0.05	0.92	0.02	0.95	0.03	0.96	0.00
Si	1.93	0.05	2.00	0.02	2.09	0.02	1.94	0.06	2.00	0.04	2.03	0.01
Al	0.01	0.01	0.01	0.00	0.02	0.01	0.01	0.00	0.01	0.00	0.01	0.00
Ti	n.a.	n.a.	n.a.	n.a.	n.a.	n.a.	n.a.	n.a.	n.a.	n.a.	n.a.	n.a.
Mg	2.89	0.04	2.86	0.03	2.60	0.19	2.84	0.05	2.82	0.05	2.80	0.00
Fe	0.23	0.12	0.11	0.02	0.17	0.15	0.25	0.07	0.16	0.09	0.13	0.01
Ca	0.00	0.00	0.00	0.00	0.00	0.00	0.00	0.00	0.00	0.00	0.00	0.00
Na	n.a.	n.a.	n.a.	n.a.	n.a.	n.a.	n.a.	n.a.	n.a.	n.a.	n.a.	n.a.
K	n.a.	n.a.	n.a.	n.a.	n.a.	n.a.	n.a.	n.a.	n.a.	n.a.	n.a.	n.a.
Mn	0.00	0.00	0.00	0.00	0.00	0.00	0.00	0.00	0.00	0.00	0.00	0.00
Total	5.06	0.05	4.99	0.02	4.89	0.02	5.04	0.06	4.99	0.04	4.97	0.01
Oxygen	7		7		7		7		7		7	

2.4.4 Reaction progress

Thermogravimetric analyses (DTA–TGA) were performed on the reaction products to constrain the amount of serpentine formed per experiment and thus reaction progress. The reaction progress (ζ) of each experiment is given in Table 2.1 and was calculated following the approach described in Lafay et al. (2012):

$$\zeta = \frac{(\text{-OH})_{measured}}{(\text{-OH})_{theoretical}} \times 100\% \qquad (2.1)$$

where the subscripts measured and theoretical denote measured mass loss between 400 °C and 700 °C, and the OH content of stoichiometric lizardite ($Mg_3Si_2O_5(OH)_4$; OH = 13 wt.%), respectively. The serpentine decomposition temperature between 500 °C and 700 °C and the exothermic peak at 820 °C are in agreement with reported values (Fig. 2.13) (e.g. Lafay et al., 2012). The DTA endothermic peak temperature for serpentine increases with experiment duration. This effect is more pronounced for samples reacted in H_2O (Fig. 2.4). The DTG curve of samples reacted with H_2O shows three weak peaks at ~603 °C, 653 °C and 684 °C (sample S–57). Serpentine formed from NaCl solutions shows one major peak at ~610 °C and a weak shoulder at 526 °C (e.g., sample S–48; Fig. 2.13).

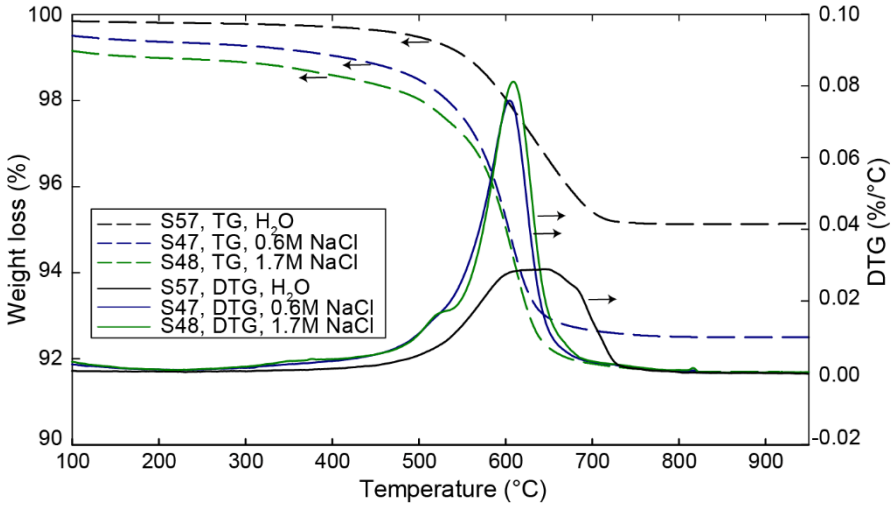

Figure 2.13: TG–DTG curves of selected samples reacted with 0 M, 0.6 M and 1.7 M NaCl solution experiments. Reaction progress of all samples that were analysed by TG is shown in Fig. 2.16. Arrows indicate axis.

The serpentinisation progress of TS harzburgite increased with NaCl concentration in the starting solution and experiment duration (Table 2.1). For example, the reaction progress reached ~50% at ~ 850 hours in 1.7 M NaCl solution and at ~1500 hours in 0.6 M NaCl solution. The reaction progress after ~1500 hours in H_2O and 0.3 M NaCl solution was 31% and 40%, respectively. The reaction progress of the SC olivine + En reactant is consistent with that obtained from TS harzburgite. For example, the reaction progress after ~832 hours was 25% in H_2O and 29% in 0.3 M NaCl starting solution (Table 2.1).

In contrast, serpentinisation reaction progress of SC olivine alone in 1.7 M NaCl solution was 3.1% after ~850 hours. Furthermore, we observe that higher NaCl-concentrations in the starting solution resulted in a slower reaction progress, which is opposite to the effect of fluid salinity on the pyroxene-bearing starting material (Table 2.1).

We also measured the serpentinisation progress of SC olivine in the presence of aqueous silica with Si concentrations of 0.4 mM and 4 mM. These experiments were run in duplicates and resulted in reproducible reaction progress of ~3% (0.4 mM) and ~16.5% (4 mM). A complementary experiment in 4 mM Na-Silicate solution with an additional 1.7 M NaCl yielded a reaction progress of ~15%, suggesting that the slowing effect of salinity is small relative to the accelerating effect of aqueous silica (Table 2.1).

Recorded TGA curves for all samples are given in appendix Figures 1 to 7.

2.4.5 Fluid composition

Compositions of the final solutions were analysed to complement textural observations (Table 2.6). The fluid pH increased to a maximum of ~11 in NaCl–bearing starting solutions, whereas experiments in H_2O did not result in a measurable pH change. Mg concentrations are in most samples below the detection limit (0.21 mmol L^{-1}). Ca concentrations correlate positively with reaction duration, particularly for experiments with NaCl–bearing starting solutions. Si concentrations show a steady decrease with reaction duration and are higher in NaCl–free experiments with S-94 being an outlier. F was measured at a maximum concentration of 0.25 mmol L^{-1} and Na concentrations consistently increased with experiment duration.

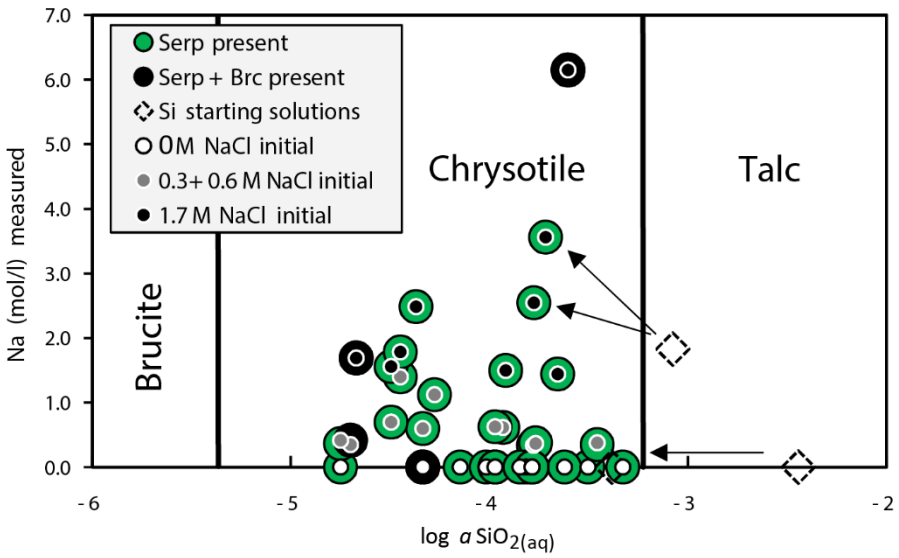

Figure 2.14: Observed phases plotted in T – log $aSiO_2$,aq diagram calculated by SUPCRT (Johnson et al., 1992) at experimental conditions, T fixed at 240. °C and P = 33.54 bar.

Table 2.6 Measured fluid composition after the experiment

exp. No.	Initial fluid composition	Time (h)	pH 25°C	Al	Ca	Fe	Mg	Na	Ni	Si	F
				(mmol / kg)							
Twin Sisters peridotite											
S-44	H_2O	164	8	< 0.019	0.10	0.027	< 0.206	3.61	0.0020	0.31	0.06
S-35	H_2O	329	n.a.	0.022	0.16	0.011	< 0.206	2.65	0.0014	0.24	0.04
S-56	H_2O	475	7	0.033	0.12	0.018	< 0.206	0.78	0.0007	0.07	0.07
S-33	H_2O	810	n.a.	n.a.	n.a.	n.a.	n.a.	n.a.	n.a.	n.a.	n.a.
S-51	H_2O	857	6	0.019	0.19	< 0.002	< 0.206	4.09	0.0049	0.10	0.05
S-46	H_2O	1505	7	< 0.019	0.30	0.040	< 0.206	5.22	0.0079	0.11	0.11
S-57	H_2O	1888	n.a.	n.a.	n.a.	n.a.	n.a.	n.a.	n.a.	n.a.	n.a.
S-88	0.3 M NaCl	169	6	n.a.	n.a.	n.a.	n.a.	n.a.	n.a.	n.a.	n.a.
S-36	0.3 M NaCl	329	n.a.	0.033	0.26	0.016	< 0.206	340	0.0038	0.17	0.05
S-24	0.3 M NaCl	810	n.a.	n.a.	n.a.	n.a.	n.a.	n.a.	n.a.	n.a.	n.a.
S-29	0.3 M NaCl	1508	n.a.	n.a.	n.a.	n.a.	n.a.	n.a.	n.a.	n.a.	n.a.
S-58	0.3 M NaCl	1888	9	< 0.019	1.09	0.011	< 0.206	1125	0.0020	0.05	n.a.
S-87	0.6 M NaCl	169	6	< 0.0019	0.16	< 0.002	< 0.206	618	0.0000	0.12	n.a.
S-37	0.6 M NaCl	329	n.a.	0.026	0.26	0.036	< 0.206	626	0.0101	0.11	0.06
S-39	0.6 M NaCl	665	8	< 0.019	0.35	0.018	< 0.206	600	0.0027	0.05	0.09
S-42	0.6 M NaCl	857	10	0.019	0.49	0.025	< 0.206	696	0.0077	0.03	0.10
S-47	0.6 M NaCl	1505	9	0.037	1.30	0.075	< 0.206	1401	0.0041	0.04	0.25
S-45	1.7 M NaCl	164	7	0.030	0.15	0.025	0.2468	1444	0.0089	0.22	0.06
S-38	1.7 M NaCl	329	n.a.	0.041	0.27	0.014	< 0.206	1501	0.0060	0.12	0.08
S-40	1.7 M NaCl	665	9	0.019	0.39	0.018	< 0.206	1557	0.0092	0.03	0.10
S-43	1.7 M NaCl	857	11	< 0.019	0.87	0.029	< 0.206	1788	0.0029	0.04	0.06
S-48	1.7 M NaCl	1505	11	< 0.019	1.30	0.067	< 0.206	2486	0.0003	0.04	0.21
S-94	1.7 M NaCl	2010	10	< 0.019	1.32	0.007	< 0.206	6151	0.0011	0.25	n.a.

Table 2.6 continued

exp. No.	Initial fluid composition	Time (h)	pH 25°C	Al	Ca	Fe	Mg	Na	Ni	Si	F
				(mmol / kg)							
San Carlos olivine											
SC-6	H_2O	857	7	0.026	0.08	0.029	< 0.206	0.70	0.0034	0.05	0.10
SC-8	0.3 M NaCl	857	9	0.022	0.10	0.023	< 0.206	414	0.0049	< 0.018	0.08
SC-9	1.7 M NaCl	857	9	0.022	0.07	0.020	< 0.206	1692	0.0027	0.02	0.11
San Carlos olivine + Enstatite											
M-1	H_2O	832	6	< 0.019	0.04	< 0.002	< 0.206	0.22	0.0024	0.47	n.a.
M-2	H_2O	832	6	< 0.019	0.06	< 0.002	< 0.206	0.22	0.0010	0.11	n.a.
M-3	H_2O	832	6	< 0.019	0.09	0.004	< 0.206	0.22	0.0007	0.02	n.a.
M-4	0.3 M NaCl	832	6	< 0.019	0.14	0.004	< 0.206	351	0.0009	0.35	n.a.
M-5	0.3 M NaCl	832	7	< 0.019	0.11	< 0.002	< 0.206	377	0.0012	0.17	n.a.
M-6	0.3 M NaCl	832	8	< 0.019	0.14	< 0.002	< 0.206	365	0.0007	0.02	n.a.
San Carlos olivine + aqueous silica											
SE-3	4 mM Si - 3 mM NaCl	836	10.1	< 0.019	0.08	0.002	< 0.021	5.2	0.3408	0.15	n.a.
SE-4	4 mM Si - 3 mM NaCl	836	10.6	< 0.019	0.06	< 0.002	< 0.021	3.8	< 0.0341	0.14	n.a.
SE-5	0.4 mM Si - 0.3 mM NaCl	836	n.a.	< 0.019	0.09	0.002	< 0.021	0.7	< 0.0341	0.16	n.a.
SE-6	0.4 mM Si - 0.3 mM NaCl	836	9.5	< 0.019	0.07	0.002	< 0.021	0.4	< 0.0341	0.16	n.a.
SE-7	4 mM Si -1.7 M NaCl	836	10.1	< 0.019	0.11	< 0.002	< 0.021	2549	< 0.0341	0.17	n.a.
SE-8	4 mM Si -1.7 M NaCl	836	n.a.	< 0.019	0.12	0.002	< 0.021	3562	< 0.0341	0.19	n.a.
4 mM Si - 3 mM NaCl	Starting solution	-	7.2	0.003	< 0.001	0.0005	< 0.002	3.2	< 0.0034	3.60	n.a.
0.4 mM Si - 0.3 mM NaCl	Starting solution	-	6.5	< 0.0019	< 0.001	0.0002	< 0.002	0.3	0.0511	0.41	n.a.
4 mM Si -1.7 M NaCl	Starting solution	-	6.7	< 0.0019	0.00	< 0.0002	< 0.002	1827	0.0852	0.84	n.a.

2.5 Discussion

2.5.1 Reaction product assemblages and fluid composition

All experiments resulted in the formation of serpentine and hematite regardless of the starting fluid composition and experiment duration. Furthermore, some experiments precipitated brucite (discussed below), while e.g. talc or any other secondary silicate, hydroxide and oxide phases were not found. The final fluid Mg concentrations in all but one experiment were below the detection limit. This is consistent with the measured composition of discharge fluids from seafloor hydrothermal vents implying that serpentinisation represents a sink for Mg (James et al., 2014). Also the activity of aqueous silica ($aSiO_2$,aq) is consistent with its thermodynamically predicted concentration in equilibrium with serpentine (Fig. 2.14) (Klein et al., 2013). However, $aSiO_2$,aq in fluid samples from experiments that produced the serpentine + brucite assemblage are within the same range as those from the serpentine forming experiments and thus higher than predicted by thermodynamic models. This apparent inconsistency may indicate that the measured composition of the bulk fluid is not representative of the interfacial fluid which is controlled by the replacement reaction and transport of elements from the bulk fluid to the site of reaction.

Brucite formed in experiments without enstatite in the starting material with the exception of one long-term experiment (~2000 hours) with TS harzburgite that resulted in complete enstatite dissolution as revealed by the reaction product analysis. This observation agrees with the presence of generally thicker serpentine rims around enstatite than around olivine from the same experiment, indicating that enstatite dissolved faster than olivine in our experiments. Thus, we infer that the presence of enstatite maintains $aSiO_2$,aq of the interfacial fluid at a level inhibiting brucite formation until enstatite has completely dissolved, at which point continued serpentine precipitation from the remaining olivine reduces $aSiO_2$,aq to stabilize brucite (see also e.g., Bach et al., 2004; Seyfried Jr et al., 2007). For the TS harzburgite

starting material, containing ~15 vol.% enstatite, this point is reached after ~2000 hours in 6.2 M Na (1.7 M NaCl initial solution) at 240 °C. Similar observations were made in earlier experimental studies (e.g., Marcaillou et al., 2011; Okamoto et al., 2013).

Olivine serpentinisation is known to produce reducing conditions leading to the formation of H_2 through the oxidation of the Fe2+ of the fayalite component and the formation of magnetite (e.g. Andreani et al., 2013b; Plümper et al., 2014). However, the oxide phase formed in our experiments is hematite, indicating a fO_2 higher than in natural serpentinisation systems and experiments that produced magnetite instead (e.g. Huang et al., 2017a; Malvoisin et al., 2012; Marcaillou et al., 2011). Even though the headspace of our reactors contains sufficient O_2,g for the oxidation of olivine-derived Fe^{2+} to hematite, we cannot rule out that external O_2,g diffused into through the reactor walls. Indeed, the documented weight loss of our reactors indicates open system conditions for O_2,g and H_2,g, which explains the formation of hematite instead of magnetite and also the only weak increase in fluid pH.

2.5.2 Serpentine composition

Serpentine composition changes systematically with starting material composition. Serpentine Si concentrations correlate with the proportion of enstatite in the starting assemblage. Furthermore, serpentine formed in experiments with SC olivine and En enstatite has a higher xMg than serpentine formed from TS harzburgite. This is consistent with the near Mg-endmember composition of the En enstatite (xMg = 0.98) compared with enstatite in TS harzburgite (xMg = 0.92).

A similar compositional zonation as shown for enstatite in Figure 2.12 was previously observed in serpentine rims around olivine (Oyanagi et al., 2018). Oyanagi et al. (2018) argue that the outer zone of the replacement rim represents the former location of the original grain boundary and that the inner zone resulted from progressive replacement of the original grain, whereas the rim in contact with the epoxy represents an overgrowth. Adopting this interpretation, the changing Al_2O_3 and

FeO concentrations in the different zones can be related to the composition of the interfacial fluid during replacement front propagation. Enstatite is the only Al-bearing reactant in our experiments and the increase in Al_2O_3 towards the replacement interface may reflect decreased buffering of the interfacial fluid by the bulk fluid due to the increase in transport length through the serpentine rim. In contrast, FeO is provided by both enstatite and olivine, which causes a relatively higher concentration in the bulk fluid relative to the interfacial fluid. Upon propagation of the serpentinisation front into the enstatite, the interfacial fluid FeO concentration will be more strongly controlled by FeO availability from the enstatite.

2.5.3 Evolution of serpentine morphology

A range of distinct serpentine phases and morphologies has been described in the literature for natural and experimental samples. Generally, antigorite represents the high temperature serpentine phase, whereas the polymorphs lizardite and chrysotile form at lower temperature. Lizardite exhibits a planar, tabular morphology, whereas chrysotile consists of curved layers and can also form thin fibres, tubes or cones, thus developing peculiar “cone in cone” or “tube in tube” morphologies. Furthermore, polyhedral serpentine has been described as a transitional morphology from chrysotile to lizardite due to the curved sheet in the center of the tube that evolves into planar layers on the outside (Andreani et al., 2008; Evans, 2004). On fully developed spheres, polyhedral serpentine shows an onion-shape growth morphology and distinct triangular facets (Andreani et al., 2008; Baronnet et al., 2007; Zega et al., 2006). In addition, poorly crystalline serpentine is referred to as proto-serpentine and is interpreted to form from a gel-like precursor (Andreani et al., 2008; Lafay et al., 2016; Lafay et al., 2012).

The surface morphology of secondary serpentine in our experiments changes systematically with fluid salinity (Fig. 2.15). This is apparent from short runs with distinct starting fluid salinity and longer runs that are accompanied by increasing fluid salinity due to H_2O loss from the reactors. For example, the assemblage lizardite and polyhedral serpentine exclusively formed during serpentinisation of enstatite-bearing

starting solid in non-saline solution (Fig. 2.4 and 2.6b), whereas scarce fibres form instead of polyhedral serpentine at higher salinities but below ~1.1 M NaCl (Fig. 2.7a).

Polyhedral spheres formed on enstatite surfaces together with tabular serpentine, in dissolution cavities of partly reacted enstatite, and between adjacent grains (Fig. 2.5 and 2.6e), consistent with previously inferred conditions for polyhedral serpentine formation in nature (Andreani et al., 2008; Baronnet et al., 2007).

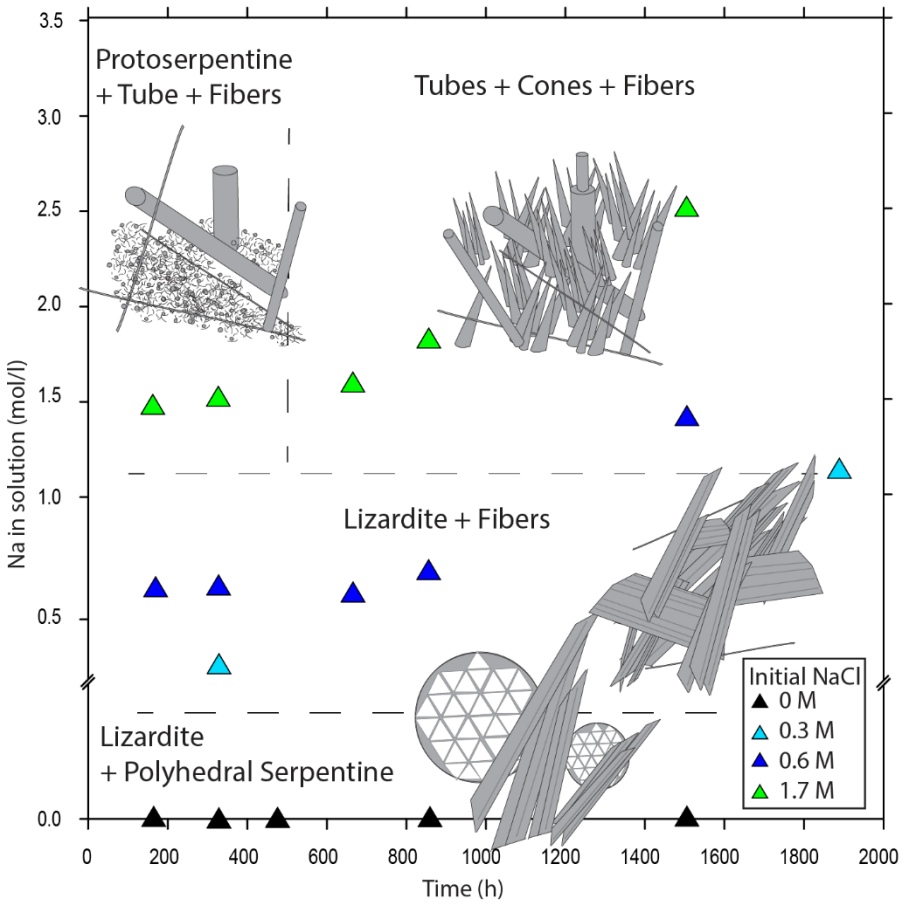

Figure 2.15: Qualitative phase diagram showing an overview of the different serpentine morphologies as a function of fluid Na concentration and reaction duration. Data points indicate analysed fluid compositions that correspond to the different morphologies. The diagram is based on experiments using TS harzburgite. One experiment (S-94) is excluded for visibility, see Table 2.1 for details. The data point at ~1900 hours refers to the assemblage depicted in Fig. 2.7b and c showing the formation of chrysotile tubes from tabular lizardite.

Serpentinisation in highly saline fluid (> 1.1 M NaCl) results in the formation of tubes and fibres together with fine grained protoserpentine at durations <330 hours (Fig. 2.9a) and together with cones at longer run times (Fig. 2.9b). This morphology evolution is most pronounced in experiments with intermediate salinity and long durations. The transition from tabular lizardite + fibres to tubes + cones + fibres (Fig. 2.7a and d) indicates that the serpentine morphology readily adjusts to changes in fluid salinity over time. The transformation commences with the curling of layer edges to form tubes, similar to nano–tube formation by selective etching techniques (Schmidt and Eberl, 2001). At higher salinity (≥ 0.6 M NaCl) this transformation went to completion already after ~1500 hours (Fig. 2.15). Hence, we infer that the assemblage tubes + cones + fibres must have always evolved from either a protoserpentine or lizardite precursor depending on the starting fluid salinity (Fig. 2.15).

The formation of distinct serpentine morphologies has previously been linked to the fluid saturation, grain size, the fluid/solid ratio, and the presence and concentration of foreign ions in (e.g. Lafay et al., 2012; Malvoisin et al., 2012; Normand et al., 2002; Ogasawara et al., 2013; Roy and Roy, 1954; Yada and Iishi, 1974, 1977). The degree of supersaturation controls the growth mechanism, which controls the crystal morphology (Otálora and García-Ruiz, 2014; Sunagawa, 1999). In addition, Lafay et al. (2014) argue that impurities and dissolved minor elements promote growth perturbations, which may result in the precipitation of morphologically distinct serpentine from fluids with different composition. Similar observations were made by Normand et al. (2002) in flow through experiments. However, Na contents, of measured serpentines show consistently low values for both, NaCl-bearing and NaCl-free experiments. The effect of chlorine as impurity was not investigated. Besides the influence of fluid salinity, serpentine morphologies may also be affected by incorporation of ferric instead of ferrous iron via ferri-Tschermark substitution or vacancy formation on the serpentine M-site (e.g. Evans, 2008). Since our reactors are essentially open systems for oxygen it is likely that most of the iron is oxidized. Natural serpentine can host high concentrations of ferric iron with Fe^{3+}/Fe_{Tot}(serp)

close to 1 in late stage veins (Andreani et al., 2013b). However, the influence of ferric iron content on serpentine morphology remains unexplored.

2.5.4 Effect of fluid and solid compositions on reaction progress

Our experiments show a systematic variation of reaction progress with the initial compositions of fluid and solid reactants (Fig. 2.16). Furthermore, reaction progress was likely influenced by the increasing fluid salinity during the course of the experiments due to the gradual loss of H_2O from our reactors. Consequently, the reaction progress at each time step will be representative of a fluid salinity higher than the starting salinity. Yet, the relative reaction progress between different experiments at given time is comparable as all experiments are subject to the same amount of H_2O loss. The reaction progress of the enstatite-bearing starting materials (TS harzburgite and SC olivine + En) increased strongly within the first ~800 hours and remained almost constant at longer durations. The final reaction progress shows a positive correlation with the starting fluid salinity and the results are consistent for TS harzburgite and SC olivine + En irrespective of the olivine/enstatite ratio. In contrast, the serpentinisation progress of SC olivine alone (8.5%) was significantly lower than that of the enstatite-bearing reactants and was even lower in 1.7 M NaCl starting solution (3.1%) (Fig. 2.16).

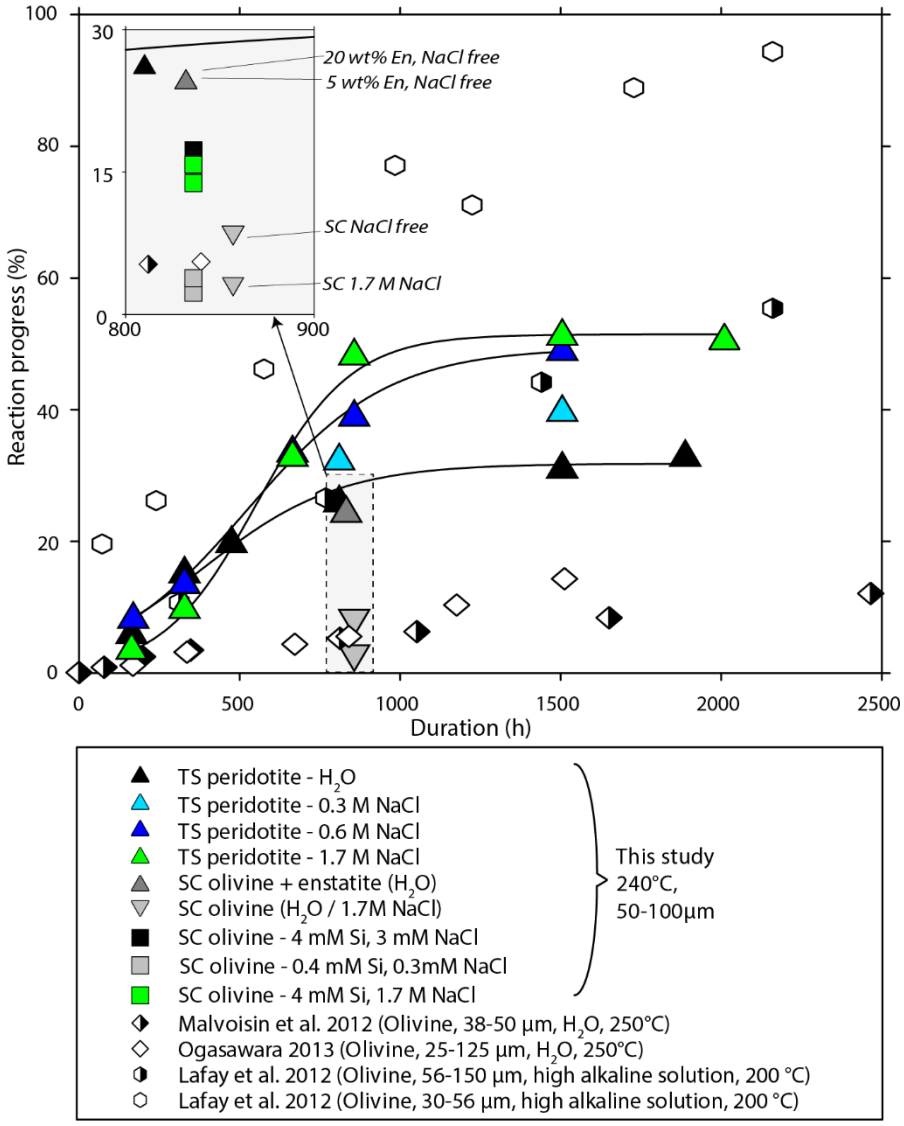

Figure 2.16 Reaction progress of the different serpentinisation experiments plotted against experiment duration. Data from Lafay et al. (2012), Malvoisin et al. (2012) and Ogasawara et al. (2013) are shown for comparison. Solid lines are added to guide the reader. Results from Si experiments are shown in insert.

This difference in reaction progress between the enstatite-bearing and enstatite-absent starting materials was somewhat unexpected. Considering that dissolution is considered as the rate limiting step of serpentinisation (Malvoisin et al., 2012), one explanation may be, theoretically, that the overall reaction progress of the enstatite-bearing starting material is controlled by enstatite dissolution with only negligible

contribution from olivine dissolution. This could be reconciled with the difference in serpentine rim thickness around enstatite and olivine from the same experimental runs. However, the interpretation is inconsistent with the relative amounts of enstatite and olivine in the composite solid starting materials. For example, after ~850 hours in 1.7 M NaCl starting solution, the serpentinisation reaction progress of SC olivine was 3.1%, whereas the reaction progress of TS harzburgite was 48% (Fig. 2.16; Table 2.1). TS harzburgite contains ~15 vol.% enstatite, which can only account for 14% reaction progress at complete replacement (assuming conservation of Mg) and requires about ~2000 hours of reaction in our experimental setup. Thus, even if enstatite reacted more than twice as fast as indicated by our experiments, the total reaction progress of TS harzburgite should not exceed ~17%, i.e. less than half of the measured reaction progress.

A similar increase in olivine serpentinisation rate was previously observed and explained by the catalytic effect of Al and Cr released from enstatite and spinel (Andreani et al., 2013a; Huang et al., 2017b; Pens et al., 2016). However, Al concentrations in our reactants are significantly lower (Al_2O_3 < 0.64 wt.%; Table 2.2) compared to the previous studies (Al_2O_3 = 4.14 wt.%; Huang et al., 2017b) and run product analyses indicate that spinel did not react at the conditions employed in our experiments. Since our experimental setup allows us to rule out that the difference in reaction progress is related to grain size, duration, and starting fluid composition, we infer that olivine serpentinisation is enhanced by the increase in Si,aq due to the higher Si/Mg in enstatite (Si/Mg = 1) compared to olivine (Si/Mg = 0.5):

$$\underset{\text{enstatite}}{3\ Mg_2Si_2O_6} + 4\ H_2O \rightarrow \underset{\text{serpentine}}{2\ Mg_3Si_2O_5(OH)_4} + 2\ SiO_2,aq \qquad (2.2)$$

$$\underset{\text{olivine}}{3\ Mg_2SiO_4} + SiO_2,aq + 4\ H_2O \rightarrow \underset{\text{serpentine}}{2\ Mg_3Si_2O_5(OH)_4} \qquad (2.3)$$

To investigate further the effect of Si,aq on olivine serpentinisation with a reduced number of unknowns, we conducted additional experiments with SC olivine in silica

bearing starting solutions in the absence of enstatite under otherwise identical temperature (240 °C) and run duration (850 hours), and with comparable starting fluid salinity. The resulting reaction progress is ~3% and ~16% in 0.4 mM and 4 mM Si,aq solution, respectively. Increasing the starting fluid NaCl concentration lowers the reaction progress insignificantly see Lamadrid et al. (2017). These results unequivocally show that the olivine serpentinisation rate increases with silica concentration in the reactive fluid, implying that olivine serpentinisation is fast during concomitant serpentinisation of enstatite. Duplicate experiments resulted in reproducible results (Table 2.1).

For the dissolution step of enstatite, Phillips-Lander et al. (2016) already established the positive correlation with fluid salinity, opposite to the effect of NaCl on olivine dissolution as shown by our results (Fig. 2.16) and previously by Lamadrid et al. (2017). The correlation of starting fluid composition and reaction progress of enstatite-bearing starting materials thus shows that the salinity-enhanced dissolution of enstatite and the resulting increase in olivine serpentinisation due to the higher Si,aq outweighs the slowing effect of salinity on olivine dissolution. Slowing of the reaction progress at experiment durations longer than ~1000 hours (Fig. 2.16) may be related to increased passivation of enstatite reactive surfaces by serpentine. Based on our results, peridotite starting materials (i.e. pyroxene bearing) can be expected to react faster than dunite (low or no enstatite), which has not been observed in earlier studies (Malvoisin et al., 2012; Marcaillou et al., 2011; Ogasawara et al., 2013; Seyfried Jr et al., 2007). This may be related to different experimental conditions and/or setup, the fact that dissolution is no longer the rate-limiting step in experiments employing very fine grained starting materials (Malvoisin et al., 2012; Marcaillou et al., 2011), and the presence of additional electrolytes in the reactive fluid (Seyfried Jr et al., 2007).

2.6 Implications and conclusions

The results of our experiments at 240 °C and vapor pressure provide new insight into the morphology evolution of serpentine formed during hydrothermal alteration of

olivine in the presence and absence of orthopyroxene. With increasing fluid salinity, the serpentine morphology evolved from fine-grained proto–serpentine, polyhedral serpentine and lizardite, to lizardite and chrysotile fibres, to serpentine tubes, cones and fibres. This allows for the qualitative reconstruction of fluid composition from the serpentine phase assemblage and morphology. Furthermore, the presence of polyhedral serpentine can be linked to ultramafic rock alteration by non–saline solutions, which may explain its relatively rare occurrence in natural alteration systems. The increase in serpentinisation rate with fluid salinity in our experiments is enhanced further by delamination of the product phases from the reactant surfaces at the highest fluid salinity. This may indicate that serpentine precipitation at high salinity is spatially decoupled from olivine/enstatite dissolution, whereas serpentinisation at lower salinity may proceed as an interface-coupled replacement reaction (Xia et al., 2009).

Moreover, our data shows that the rate of olivine serpentinisation significantly increases in the presence of dissolved silica. This observation is directly relevant for the interpretation of natural systems (e.g., Plümper et al., 2014; Tominaga et al., 2017). During natural hydrothermal alteration of ultramafic rock, the aqueous silica concentration can be expected to be higher than the equilibrium concentration with olivine if: 1.) the ultramafic rock contains additional pyroxene; 2.) the ultramafic rock is in contact with mafic, felsic and/or sedimentary rocks (Beinlich et al., 2010); and 3.) the ultramafic rock is subject to concomitant carbonation as attested by the common occurrence of secondary talc and quartz. In our experiments, the overall reaction progress of enstatite-bearing starting material was higher by a factor of ~16 compared to the pure olivine starting material.

2.7 References

Allen, D.E., Seyfried Jr, W., 2003. Compositional controls on vent fluids from ultramafic-hosted hydrothermal systems at mid-ocean ridges: An experimental study at 400 C, 500 bars. Geochim. Cosmochim. Acta , 67(8): 1531-1542.

Andreani, M., Mével, C., Boullier, A.M., Escartin, J., 2007. Dynamic control on serpentine crystallization in veins: Constraints on hydration processes in oceanic peridotites. Geochemistry, Geophysics, Geosystems, 8(2).

Andreani, M., Grauby, O., Baronnet, A., Muñoz, M., 2008. Occurrence, composition and growth of polyhedral serpentine. European Journal of Mineralogy, 20(2): 159-171.

Andreani, M., Daniel, I., Pollet-Villard, M., 2013a. Aluminum speeds up the hydrothermal alteration of olivine. Am. Mineral., 98(10): 1738-1744.

Andreani, M., Munoz, M., Marcaillou, C., Delacour, A., 2013b. μXANES study of iron redox state in serpentine during oceanic serpentinization. Lithos, 178: 70-83.

Bach, W., Garrido, C.J., Paulick, H., Harvey, J., Rosner, M., 2004. Seawater-peridotite interactions: First insights from ODP Leg 209, MAR 15 N. Geochemistry, Geophysics, Geosystems, 5(9).

Baronnet, A., Andréani, M., Grauby, O., Devouard, B., Nitsche, S. and Chaudanson, D. 2007. Onion morphology and microstructure of polyhedral serpentine. American Mineralogist 92, 687-690.

Beinlich, A., Austrheim, H., Glodny, J., Erambert, M., Andersen, T.B., 2010. CO_2 sequestration and extreme Mg depletion in serpentinized peridotite clasts from the Devonian Solund basin, SW-Norway. Geochim. Cosmochim. Acta , 74(24): 6935-6964.

Beinlich, A., Plümper, O., Hövelmann, J., Austrheim, H., Jamtveit, B., 2012. Massive serpentinite carbonation at Linnajavri, N–Norway. Terra Nova, 24(6): 446-455.

Beinlich, A., Austrheim, H., Mavromatis, V., Grguric, B., Putnis, C. V. and Putnis, A. 2018. Peridotite weathering is the missing ingredient of Earth's continental crust composition. Nat. Commun., 9(1): 634.

Evans, B.W., 2004. The serpentinite multisystem revisited: chrysotile is metastable. International Geology Review, 46(6): 479-506.

Evans, B.W., 2008. Control of the products of serpentinization by the Fe2+ Mg− 1 exchange potential of olivine and orthopyroxene. Journal of Petrology, 49(10): 1873-1887.

Hövelmann, J., Austrheim, H., Beinlich, A., Anne Munz, I., 2011. Experimental study of the carbonation of partially serpentinized and weathered peridotites. Geochim. Cosmochim. Acta , 75(22): 6760-6779.

Huang, R., Lin, C.-T., Sun, W., Ding, X., Zhan, W. and Zhu, J. 2017a. The production of iron oxide during peridotite serpentinization: Influence of pyroxene. Geoscience Frontiers 8, 1311-1321.

Huang, R., Song, M., Ding, X., Zhu, S., Zhan, W. and Sun, W. 2017b. Influence of pyroxene and spinel on the kinetics of peridotite serpentinization. Journal of Geophysical Research: Solid Earth 122, 7111-7126.

James, R.H., Green, D.R., Stock, M.J., Alker, B.J., Banerjee, N.R., Cole, C., German, C.R., Huvenne, V.A., Powell, A.M. and Connelly, D.P., 2014. Composition of hydrothermal fluids and mineralogy of associated chimney material on the East Scotia Ridge back-arc spreading centre. Geochim. Cosmochim. Acta , 139: 47-71.

Janecky, D., Seyfried Jr, W., 1986. Hydrothermal serpentinization of peridotite within the oceanic crust: experimental investigations of mineralogy and major element chemistry. Geochim. Cosmochim. Acta , 50(7): 1357-1378.

Jarosewich, E., Nelen, J.A., Norberg, J.A., 1980. Reference Samples for Electron Microprobe Analysis. Geostandards Newsletter, 4(1): 43-47.

Johnson, J.W., Oelkers, E.H., Helgeson, H.C., 1992. SUPCRT92: A software package for calculating the standard molal thermodynamic properties of minerals, gases, aqueous species, and reactions from 1 to 5000 bar and 0 to 1000 C. Computers & Geosciences, 18(7): 899-947.

Klein, F., McCollom, T.M., 2013. From serpentinization to carbonation: New insights from a CO_2 injection experiment. Earth Planet. Sci. Lett. , 379: 137-145.

Lafay, R., Montes-Hernandez, G., Janots, E., Auzende, A.-L., Chiriac, R., Lemarchand, D. and Toche, F. 2014. Influence of trace elements on the textural properties of synthetic chrysotile: Complementary insights from macroscopic and nanoscopic measurements. Microporous and Mesoporous Materials 183, 81-90.

Lafay, R., Montes-Hernandez, G., Janots, E., Chiriac, R., Findling, N. and Toche, F. 2012. Mineral replacement rate of olivine by chrysotile and brucite under high alkaline conditions. Journal of Crystal Growth, 347(1), 62-72.

Lafay, R., Fernandez-Martinez, A., Montes-Hernandez, G., Auzende, A.L., Poulain, A., 2016. Dissolution-reprecipitation and self-assembly of serpentine nanoparticles preceding chrysotile formation: Insights into the structure of proto-serpentine. Am. Mineral., 101(12): 2666-2676.

Lamadrid, H.M., Rimstidt, J.D., Schwarzenbach, E.M., Klein, F., Ulrich, S., Dolocan, A. and Bodnar, R.J. 2017. Effect of water activity on rates of serpentinization of olivine. Nature communications 8, 16107.

Malvoisin, B., Brunet, F., Carlut, J., Rouméjon, S., Cannat, M., 2012. Serpentinization of oceanic peridotites: 2. Kinetics and processes of San Carlos olivine hydrothermal alteration. J. Geophys. Res.: Solid Earth, 117(B4).

Marcaillou, C., Munoz, M., Vidal, O., Parra, T., Harfouche, M., 2011. Mineralogical evidence for H2 degassing during serpentinization at 300 C/300 bar. Earth Planet. Sci. Lett. , 303(3-4): 281-290.

Martin, B., Fyfe, W., 1970. Some experimental and theoretical observations on the kinetics of hydration reactions with particular reference to serpentinization. Chem. Geol., 6: 185-202.

McCollom, T.M., Klein, F., Robbins, M., Moskowitz, B., Berquó, T.S., Jöns, N., Bach, W. and Templeton, A. 2016. Temperature trends for reaction rates, hydrogen generation, and partitioning of iron during experimental serpentinization of olivine. Geochimica et Cosmochimica Acta 181, 175-200.

Normand, C., Williams-Jones, A.E., Martin, R.F., Vali, H., 2002. Hydrothermal alteration of olivine in a flow-through autoclave: Nucleation and growth of serpentine phases. Am. Mineral., 87(11-12): 1699-1709.

Oelkers, E.H., Schott, J., 2001. An experimental study of enstatite dissolution rates as a function of pH, temperature, and aqueous Mg and Si concentration, and the mechanism of pyroxene/pyroxenoid dissolution. Geochim. Cosmochim. Acta, 65(8): 1219-1231.

Ogasawara, Y., Okamoto, A., Hirano, N., Tsuchiya, N., 2013. Coupled reactions and silica diffusion during serpentinization. Geochim. Cosmochim. Acta , 119: 212-230.

Okamoto, A., Ogasawara, Y., Hirano, N., Tsushiya, N., 2013. Effect of silica transport on serpentinization in the Ol-Opx-H_2O system. Procedia Earth and Planetary Science, 7: 628-631.

Olsen, A.A., Hausrath, E.M., Rimstidt, J.D., 2015. Forsterite dissolution rates in Mg-sulfate-rich Mars-analog brines and implications of the aqueous history of Mars. Journal of Geophysical Research: Planets, 120(3): 388-400.

Otálora, F., García-Ruiz, J., 2014. Nucleation and growth of the Naica giant gypsum crystals. Chemical Society Reviews, 43(7): 2013-2026.

Oyanagi, R., Okamoto, A., Harigane, Y., Tsuchiya, N., 2018. Al-zoning of serpentine aggregates in mesh texture induced by metasomatic replacement reactions. Journal of Petrology.

Oyanagi, R., Okamoto, A., Hirano, N., Tsuchiya, N., 2015. Competitive hydration and dehydration at olivine–quartz boundary revealed by hydrothermal experiments: Implications for silica metasomatism at the crust–mantle boundary. Earth Planet. Sci. Lett. , 425: 44-54.

Pens, M., Andreani, M., Daniel, I., Perrillat, J.-P., Cardon, H., 2016. Contrasted effect of aluminum on the serpentinization rate of olivine and orthopyroxene under hydrothermal conditions. Chem. Geol., 441: 256-264.

Petriglieri, J. R., Salvioli-Mariani, E., Mantovani, L., Tribaudino, M., Lottici, P. P., Laporte-Magoni, C. and Bersani, D., 2015. Micro-Raman mapping of the polymorphs of serpentine. Journal of Raman Spectroscopy, 46(10): 953-958.

Phillips-Lander, C., Legett, C., Parnell, S., Elwood Madden, A., Elwood Madden, M., 2016. Pyroxene dissolution rates in high salinity brines: Implications for post-Noachian aqueous alteration on Mars, Lunar and Planetary Science Conference, pp. 1313.

Plümper, O., Beinlich, A., Bach, W., Janots, E., Austrheim, H., 2014. Garnets within geode-like serpentinite veins: Implications for element transport, hydrogen production and life-supporting environment formation. Geochim. Cosmochim. Acta , 141: 454-471.

Plümper, O., King, H.E., Geisler, T., Liu, Y., Pabst, S., Savov, I.P., Rost, D. and Zack, T., 2017. Subduction zone forearc serpentinites as incubators for deep microbial life. Proceedings of the National Academy of Sciences.

Pokrovsky, O.S., Schott, J., 2000. Kinetics and mechanism of forsterite dissolution at 25 C and pH from 1 to 12. Geochim. Cosmochim. Acta , 64(19): 3313-3325.

Roy, D.M., Roy, R., 1954. An experimental study of the formation and properties of synthetic serpentines and related layer silicate minerals. Am. Mineral., 39(11-1): 957-975.

Rüpke, L.H., Morgan, J.P., Hort, M., Connolly, J.A., 2004. Serpentine and the subduction zone water cycle. Earth Planet. Sci. Lett. , 223(1-2): 17-34.

Schmidt, O.G., Eberl, K., 2001. Nanotechnology: Thin solid films roll up into nanotubes. Nature, 410(6825): 168.

Seyfried Jr, W., Foustoukos, D., Fu, Q., 2007. Redox evolution and mass transfer during serpentinization: An experimental and theoretical study at 200 C, 500 bar with implications for ultramafic-hosted hydrothermal systems at Mid-Ocean Ridges. Geochim. Cosmochim. Acta , 71(15): 3872-3886.

Sunagawa, I., 1999. Growth and morphology of crystals. FORMA-TOKYO-, 14(1/2): 147-166.

Tominaga, M., Beinlich, A., Lima, E. A., Tivey, M. A., Hampton, B. A., Weiss, B. and Harigane, Y., 2017. Multi-scale magnetic mapping of serpentinite carbonation. Nat. Commun., 8(1): 1870.

Ulven, O.I., Beinlich, A., Hövelmann, J., Austrheim, H., Jamtveit, B., 2017. Subarctic physicochemical weathering of serpentinized peridotite. Earth Planet. Sci. Lett. , 468: 11-26.

Van Noort, R., Spiers, C., Drury, M., Kandianis, M., 2013. Peridotite dissolution and carbonation rates at fracture surfaces under conditions relevant for in situ mineralization of CO_2. Geochim. Cosmochim. Acta , 106: 1-24.

Wang, A., Freeman, J.J., Jolliff, B.L., 2015. Understanding the Raman spectral features of phyllosilicates. Journal of Raman Spectroscopy, 46(10): 829-845.

Wegner, W.W., Ernst, W., 1983. Experimentally determined hydration and dehydration reaction rates in the system MgO-SiO_2-H_2O. Amer. J. Sci., 283: 151-180.

Whitney, D.L., Evans, B.W., 2010. Abbreviations for names of rock-forming minerals. Am. Mineral., 95(1): 185-187.

Xia, F., Brugger, J., Chen, G., Ngothai, Y., O'Neill, B., Putnis, A. and Pring, A. 2009. Mechanism and kinetics of pseudomorphic mineral replacement reactions: A case study of the replacement of pentlandite by violarite. Geochimica et Cosmochimica Acta, 73(7), 1945-1969.

Yada, K., Iishi, K., 1974. Serpentine minerals hydrothermally synthesized and their microstructures. Journal of Crystal Growth, 24: 627-630.

Yada, K., & Iishi, K. 1977. Growth and microstructure of synthetic chrysotile. American Mineralogist, 62(9-10), 958-965.

Zega, T. J., Garvie, L. A., Dódony, I., Friedrich, H., Stroud, R. M. and Buseck, P. R.., 2006. Polyhedral serpentine grains in CM chondrites. Meteoritics & Planetary Science, 41(5): 681-688.

Chapter 3

Experimental Ni-tenor modification of Fe-Ni-sulphides through hydrothermal alteration

A modified version of this manuscript is in preparation for submission to a scientific journal.

Tobias Wengorsch, Ben Grguric, Andreas Beinlich, Andrew Putnis

3.1 Abstract

Post-magmatic hydrothermal alteration is an important process that has a major influence on the economic viability of many low grade sulphide deposits. In the case of magmatic Ni sulphide deposits hosted in olivine-rich lithologies, the most important process is serpentinisation and carbonation of the olivine gangue, however, the exact mechanism of how alteration of the gangue results in modification of the sulphide assemblage is controversial. In this study, we experimentally simulated the hydrothermal alteration of a magmatic Ni sulphide deposits by reacting high pH, NaCl bearing fluids at 240 °C with a composite powder of olivine rich gangue and Ni-sulphides to simulate an artificial Ni ore. The sulphide assemblages were upgraded in Ni-tenor through the replacement of pyrrhotite by magnetite, by the transformation of pentlandite to millerite and heazlewoodite, and by increasing Ni-contents in residual pentlandite. The product sulphide assemblages were dependent on redox conditions of fO_2, bulk composition of the sulphide fraction and the ratio between silicates and sulphides in the starting materials.

3.2 Introduction

Type 2 disseminated, magmatic, nickel sulphide deposits represent an economically-important type of Ni-deposit hosted in olivine cumulate rocks and characterised by often complex sulphide assemblages of high Ni-tenor (Groves et al., 1974; Eckstrand, 1975; Grguric et al., 2006; Grguric et al., 2013). The predominance of high-tenor Ni sulphides in Type 2 deposits contrasts with that of massive Ni sulphide deposits. Sulphide blebs (<5 mm across) are observed in various assemblages in these deposits, varying in Ni-tenor from pentlandite-pyrrhotite (corresponding essentially to the unmodified magmatic monosulphide solid solution Ni:Fe:S ratio) to the extreme of native nickel (99% Ni; Grguric et al., 2013). While it is generally accepted that the upgrading is due to hydrothermal overprinting, the exact mechanism of this post-magmatic tenor modification is controversial, and various mechanisms

have been proposed since the discovery of Mount Keith and other similar deposits in the late 1960's. Overall, these mechanisms can be simplified into two basic concepts:

1. Ni originally hosted in the silicate lattice of magmatic olivine (forsterite) at levels from 100's to 1000's of ppm is partially released during serpentinisation and carbonation and is preferentially partitioned into existing (recrystallised) magmatic sulphide blebs, thus increasing their Ni tenor (Barnes & Hill, 2000; Donaldson, 1981; Eckstrand, 1975; Groves et al., 1974; Sciortino et al., 2015)

2. Serpentinisation and carbonation results in progressive replacement of original magmatic sulphide blebs (of bulk composition approximately corresponding to primary mss) by non-sulphide species, consequently enriching the residual sulphide phase in Ni (Grguric, 2003; Grguric et al., 2006 & 2013; Konnunaho et al., 2013; Gole, 2014)

A distinct zonation in the gangue alteration assemblages of many Type 2 Ni deposits, from talc-carbonate alteration to serpentinisation has been shown to correspond to changes in sulphide assemblages within these zones (Eckstrand, 1975; Grguric et al., 2006; Barnes et al., 2009). The sulphides in these deposits are essentially accessory phases and the marked changes in Ni-tenor observed highlights the importance of fluids involved in the gangue alteration processes. Eckstrand (1975) developed a model for barren and weakly mineralized ultramafic rocks to explain the occurrence of different high tenor sulphides and Ni-alloys. He posited that these assemblages are controlled by the oxygen fugacity (fO_2) imposed by the hydrothermal reaction of the host rock. Serpentinsation leads to very reducing conditions, through the oxidation of ferrous iron of the fayalite component in olivine (e.g. Frost & Beard, 2007). In contrast, the conversion of olivine to talc-carbonate assemblages results in less reducing fluids (Eckstrand, 1975).

Numerous petrographic studies on Type 2 Ni sulphide deposits have been performed which have highlighted the variations in sulphide assemblages associated

with serpentinisation and carbonation of the host ultramafics (e.g. Eckstrand, 1975; Groves et al., 1974; Donaldson, 1981; Grguric, 2003; Gole, 2008; Barnes et al., 2009; Grguric et al., 2013). In contrast, few experimental studies relevant to the alteration processes in these deposits has been undertaken. Experimental work on the partitioning of Ni-Fe between olivine and sulphide at high temperatures has been performed by Clark and Naldrett (1972), Fleet et al. (1977), Fleet and MacRae (1983, 1987, 1988) and Brenan (2003). Filippidis (1982, 1985) conducted experimental serpentinisation of Ni-bearing olivine and demonstrated the formation of fine-grained Ni-sulphides and awaruite in the presence of dissolved S. Anders (2012) investigated the effect of olivine serpentinization on Ni-sulphides at very high silicate:sulphide ratios (99.66:0.33), characteristic for oceanic peridotites and found transformation of pentlandite to Ni-rich pentlandite and heazlewoodite. So far, no serpentinisation experiments have been undertaken on olivine-rich gangue containing sulphides as a starting material in order to simulate the hydrothermal alteration of an ultramafic-hosted ore. In this study, we hydrothermally altered a simulated Type 2 ore consisting of mixtures of natural olivine and sulphides (pentlandite, pyrrhotite, pyrite) to reproduce sulphide textures and mineral chemistry found in natural analogues, and to constrain conditions of the alteration reactions. Alkaline solutions were used to mimic their natural occurrence in ultramafic systems (Chavagnac et al., 2013) and due to their ability to increase the reaction rate of serpentinisation (Lafay et al., 2012). Furthermore, NaCl was added to the reacting solution, as chlorine is believed to be an important component of fluid responsible for the alteration of Ni-sulphide deposits (Stueber et al., 1968; Grguric et al., 2001; Gole, 2014). We varied the silicate:sulphide ratio from 5:95 to 0:100 in order to investigate the response of the sulphide fraction to hydrothermal alteration at known modal quantities in the system. Lastly, we compared the observed replacement textures to textures observed in natural Ni-sulphide deposits.

3.3 Methods

3.3.1 Starting Materials

Experimental

Fresh harzburgite (olivine: Fo92, enstatite: xMg: 0.92) from Twin Sisters Mountain, Washington State, USA (TS), and single crystals of olivine (Fo89) from San Carlos, Arizona, USA were crushed in a tungsten carbide disc mill (see also Table 2.2). Natural Ni-Fe sulphide ore from Lanfranchi, Western Australia (WA) and a separate of natural pentlandite crystals from Kambalda, WA, were disaggregated using a SelFrag AG electric pulse disaggregator at the John de Later Centre, Curtin University. This procedure was chosen to prevent the introduction of dislocations, which are believed to influence reaction kinetics. All powdered samples were sieved to yield particle sizes between 50 to 100 µm and washed in distilled water and ethanol. Starting materials were checked optically and by powder X-ray diffraction for impurities. A stock solution was prepared using 50% NaOH, sodium chloride 99.9 % (AnalaR NORMAPUR) and MilliQ water. This was diluted and 0.3 M NaCl added to produce a starting fluid with a pH = 12.75.

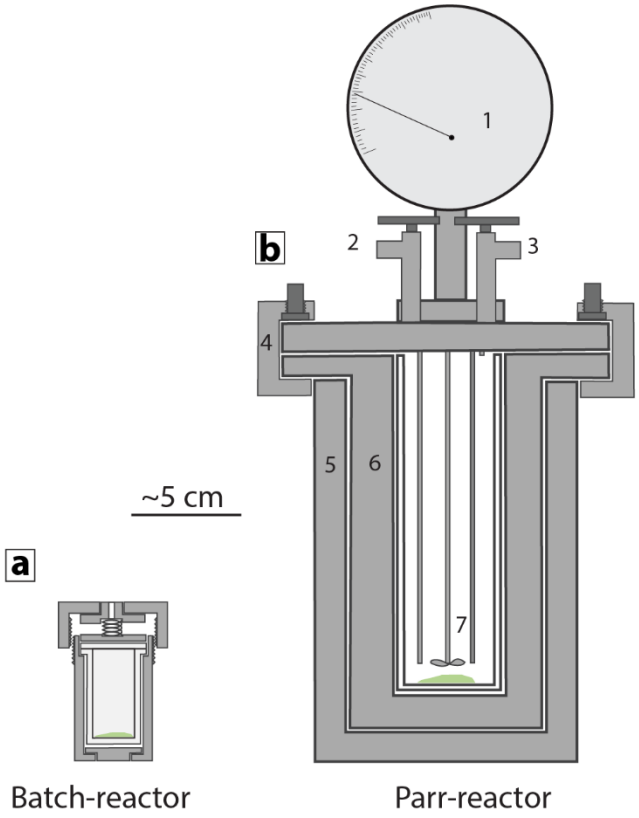

Figure 3.1: Comparison between batch reactor and Parr reactor. (a) Schematic sketch of batch reactor with Teflon liner. (b) Schematic sketch of Parr reactor with pressure gauge (1), gas inlet (2), gas outlet (3), clamps to seal the reactor (4), heating bay (5), reactor wall (6) and stirring unit with thermocouple (7).

Twenty-one hydrothermal batch experiments were performed using stainless steel batch reactors with 10 ml Teflon liners at 240ºC (Fig. 3.1a). All charges consisted of 100 mg powder and 5 ml fluid with the powder consisting of a mixture of silicate and sulphide powders in ratio varying from 5:95 to 0:100. Experiment durations were 2 days to 5 weeks. At the end of each experiment the fluid was filtered through a 0.45 µm syringe filter and acidified with 2% nitric acid. Solids were washed in distilled water and ethanol and dried in an oven for 1 hour at 100 °C. Although the reactors were properly shut before the experiment, a linear increase in weight loss for the Teflon liner was observed (0.048 g/day), which is attributed to loss of H_2O by permeation through the liner.

To test the influence of oxygen (either dissolved in the fluid phase or atmospheric within the headspace), an additional experiment using a Parr stirred reactor (Fig. 3.1b; Parr Instrument Company, Moline, Illinois) was conducted. The reactor consisted of a stainless steel vessel with a 50 ml Teflon liner. To ensure inert behaviour during experiment, titanium was used for the gas inlet tube, thermocouple and stirring unit, which reach into the Teflon liner and were in contact with the fluid. To passivate the material before the experiment, the reactor was filled with 20% nitric acid and held at 70°C for several hours, followed by triple washing with Milli-Q water. The sample consisted of 320 mg of Twin Sisters harzburgite, 80 mg Lanfranchi sulphide powder and 20 ml fluid. To obtain the same fluid composition as for batch reactor experiments NaOH pellets and NaCl were used and added to the solid charge. The reactor was flushed with nitrogen gas (20 bar) six times to remove oxygen from the vessel and filled with 20 ml degassed Milli-Q water over the gas inlet using a Semi-Prep degasser (Biotech Degasi) and Quizix QX pump (Chandler Engineering) over a period of 20 min. Finally, the reactor was placed in the heating bay controlled by a 4848 Reactor Controller (Parr) and heated to 240°C for 5 weeks. An internal stirrer was employed for the initial 20 min to ensure dissolution of NaCl and NaOH. A summary of experimental conditions is given in Table 3.1.

Natural samples

In order to compare textures of experimental reaction products with natural analouges, representative thin section samples of two disseminated Ni-sulphide deposit were examined, Mount Keith deposit and Black Swan deposit, both in Western Australia. Selected samples exhibit complete serpentinisation with minor carbonation, in addition sulphide minerals show significant alteration. No chemical analysis were performed on these samples.

Table 3.1: Experimental conditions and observed replacement phases

Experiment	Time (h)	Wt% sulphide in assemblage	Silicate material	Replacement sulphides	Replacement Fe-oxide
Pentlandite - Pyrrhotite - Pyrite					
S89	49	5	TS	Hzl	Mag, Hem
S90	94	5	TS	Hzl	Mag, Hem
S91	167	5	TS		Mag, Hem
S81	307	5	TS	Mlr	Mag, Hem
S102	835	5	TS	Mlr	Mag, Hem
S86	328	20	TS		Mag, Hem
S75	856	20	TS	Mlr	Mag, Hem
S82	307	40	TS		Mag, Hem
S103	835	40	TS		Mag, Hem
D12a	859	5	SC	Mlr	Mag, Hem
D8a	328	20	SC		Mag, Hem
D11a	833	20	SC	Mlr	Mag, Hem
D13a	859	40	SC		Mag, Hem
Lanfr5	328	100	-	Mss	Mag
Lanfr6	835	100	-	Mss	Mag
Parr1	836	20	TS	Hzl	Mag, (Hem)
Pentlandite					
S96	329	20	TS	Hzl	Mag, Hem
S97	833	20	TS	Hzl, Mlr	Mag, Hem
D9a	329	20	SC	Hzl	Mag, Hem
D10a	833	20	SC	Hzl, Mlr	Mag, Hem
Pent 1	329	100	-		Mag
Pent 2	833	100	-		Mag

3.3.2 Analysis of starting materials and run products

Electron microprobe analysis

The chemical composition of solid starting materials and run product phases was obtained by Electron Probe Micro Analysis (EPMA) on carbon–coated epoxy mounts using a JEOL JXA 8530F at the University of Münster, Germany and at the Centre for Microscopy, Characterisation and Analysis (CMCA), University of Western Australia. Olivine and pyroxene starting materials were analysed using a spot size of 1 μm and with an accelerating voltage of 20 keV, a 15 nA beam current, 30 s peak counting time and 5 s for background counts. Probe standards were periclase (Mg), corundum (Al), wollastonite (Ca), Durango fluorapatite (P), rutile (Ti), Mn-metal (Mn), magnetite (Fe), orthoclase (K) and jadeite (Na). Sulphides were analysed using

a spot size of 1 μm, an acceleration voltage of 20 keV, 40 nA beam current, 20 s peak counting time for S and Fe, and 40 s counting time for Cu, Ni and Co. Element maps were acquired at 20 keV and beam current of 40 nA, 0.5 μm step size and 200 ms dwell time. Standards were pentlandite (S, Fe), Cu-metal (Cu), millerite (Ni) and Co-metal (Co). Energy-dispersive X-ray Spectroscopy (EDS) maps were acquired on a FESEM, FEI Verios XHR, with 15 keV, 10 keV and 1.6 nA at CMCA. Mineral abbreviation follow those of Whitney and Evans (2010), in addition monosulphide solid solution in abbreviated Mss. Due to the small size and shape of the replacement products in combination with the formed porosity, it was difficult to obtain data free of contamination by another phase.

The nickel sulphide ore from Lanfranchi Nickel Mine, WA, consisted of pentlandite ($Fe_{4.2}Ni_{4.6}S_{8.1}$) ~42 wt%, pyrrhotite ~41 wt%, pyrite ~13 wt%, ~3 wt% chalcopyrite, and minor carbonate minerals. The pentlandite separate from Kambalda, WA, consisted of pentlandite ($Fe_{4.6}Ni_{4.2}S_{8.1}$) and minor monoclinic pyrrhotite and chalcopyrite ($CuFeS_2$). TS harzburgite consisted of ~83% olivine (Fo92) and ~15 wt% orthopyroxene (xMg = 0.92) with minor diopside, tremolite, lizardite, and chromite. San Carlos olivine used in this study has a composition of Fo89. Chemical compositions of starting materials are given in Table 2.2 and 3.2.

SEM and EDS analysis

High resolution imaging was performed on a FEI Verios XHR on Pt-coated samples at CMCA, The University of Western Australia. Images and backscattered electrons (BSE) at an acceleration voltage of 5 kV, 10 kV and a beam current of 0.1 nA for imaging and 1.6 nA for the mapping and spot analysis with the integrated Electron dispersive X-ray spectroscopy (EDS) detector.

Fluid analysis

Fluid sample compositions were analysed by Inductively Coupled Plasma–Optical Emission Spectrometry (ICP–OES) for Al, Ca, Fe, Ni, Mg, Na, Si and S at LabWest (Perth, Australia). Approximately 1 ml of fluid was used to measure fluid pH using a

Thermo Scientific Orion Star A211 pH meter at room temperature. The fluid sample of the O_2-free run was analysed without dilution in 2% nitric acid due to the precipitation of fine particles of reddish colour at the dilution step.

Table 3.2: Chemical composition of starting materials

Sample	Pentlandite Separate		Pentlandite Lanfranchi		Pyrrhotite Lanfranchi		Pyrite Lanfranchi	
n	9		18		9		10	
	Mean	SD	Mean	SD	Mean	SD	Mean	SD
S wt%	33.39	0.07	33.33	0.41	39.33	0.12	53.22	0.31
Fe wt%	33.14	0.15	30.39	0.79	59.23	0.65	45.43	0.52
Cu wt%	0.01	0.00	0.00	0.00	0.00	0.01	0.01	0.01
Ni wt%	32.12	0.13	35.29	0.61	0.64	0.03	0.34	0.36
Co wt%	0.42	0.03	0.28	0.05	0.02	0.03	1.33	0.30
Total	99.08	0.19	99.33	0.43	99.26	0.56	100.35	0.18
S at%	47.73		47.58		53.37		66.95	
Fe at%	27.20		24.91		46.15		32.81	
Ni at%	25.08		27.52		0.48		0.23	

3.4 Results

3.4.1 Serpentinisation of Lanfranchi sulphide and olivine mixtures

Mixtures of Lanfranchi sulphides and olivine varying in proportion from 5:95 to 40:60 were serpentinised in the standard stainless steel batch reactors at 240°C. Experimental durations varied from 49 hours to 5 weeks (Table 3.1). Alteration of silicate material resulted in the formation of serpentine rims around silicates, but also occasional coatings around sulphide grains (Fig. 3.2a arrow). Morphological observation of the replacement rim suggest a mixture of serpentine and minor brucite as the alteration product (Fig. 3.2b). A significant result of all these runs was that pyrrhotite was partly to completely replaced by magnetite, with the degree of replacement influenced by the sulphide:silicate ratio of the starting material.

In the case of the run with 5:95 sulphide:silicate starting material (S89), complete replacement of pyrrhotite by magnetite occurred within the shortest experimental duration (49 h), while in the runs containing sulphides only (Lanfr5, Lanfra6), some relict atolls of pyrrhotite were noted within the cores of the magnetite replacements (Fig. 3.3e). The magnetite after pyrrhotite generated in these batch reactor runs contained cores made up of a porous aggregate of subhedral to euhedral magnetite crystals and rims that either sharply preserved the former pyrrhotite grain margin (Fig. 3.3a), or were coated with aggregates of subhedral to euhedral magnetite crystals.

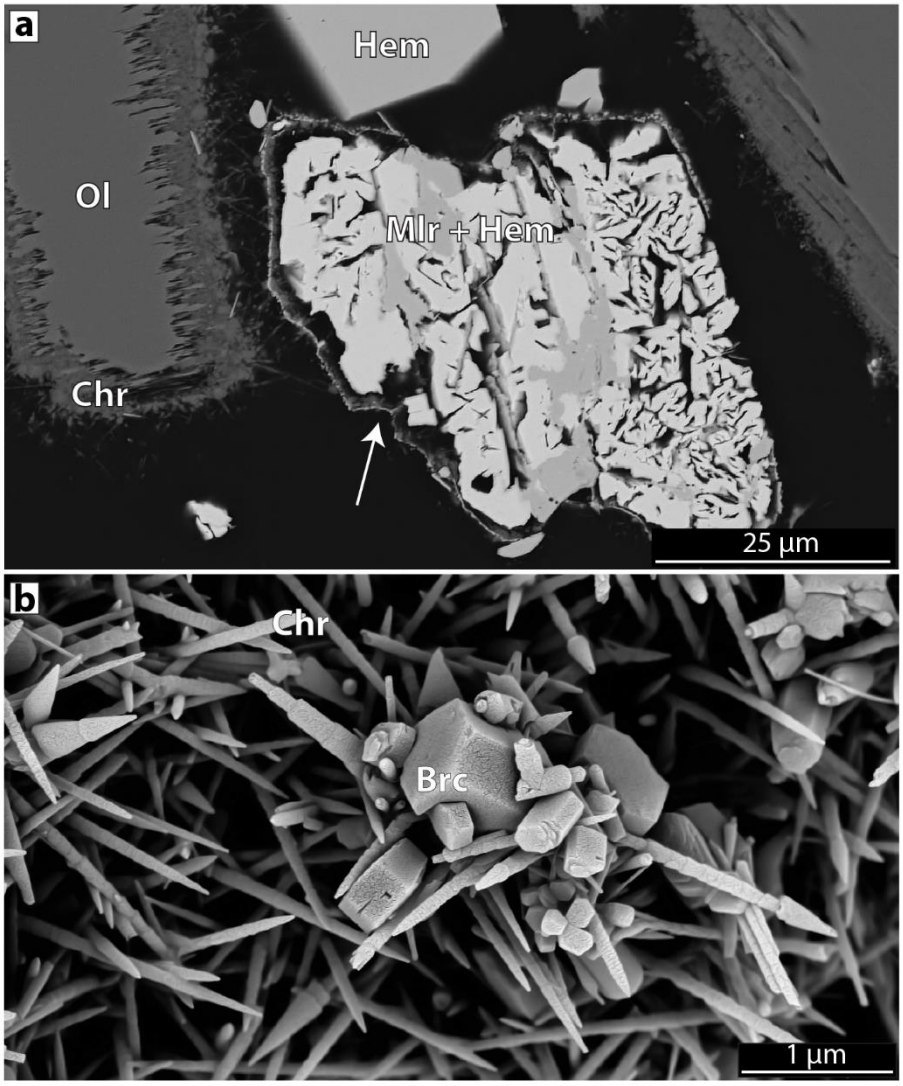

Figure 3.2: (a) BSE of cross-section in experiment S-75 after 856 h showing serpentine rims (Chr) around olivine and replaced sulphide (arrow). (b) Surface BSE image of the serpentine replacement rim of the same sample. Serpentine exhibits chrysotile morphology and small hexagonal crystals of brucite.

All the (oxygen bearing) batch reactor runs yielded hematite as a reaction product of the serpentinisation reactions. Hematite formed subhedral to euhedral crystals up to 50 microns encrusting both silicate (Fig. 3.3b) and sulphide grain margins, and was present as fracture-fill in sulphides and silicates. In some runs, hematite was also observed finely intergrown with magnetite which had replaced sulphide grains.

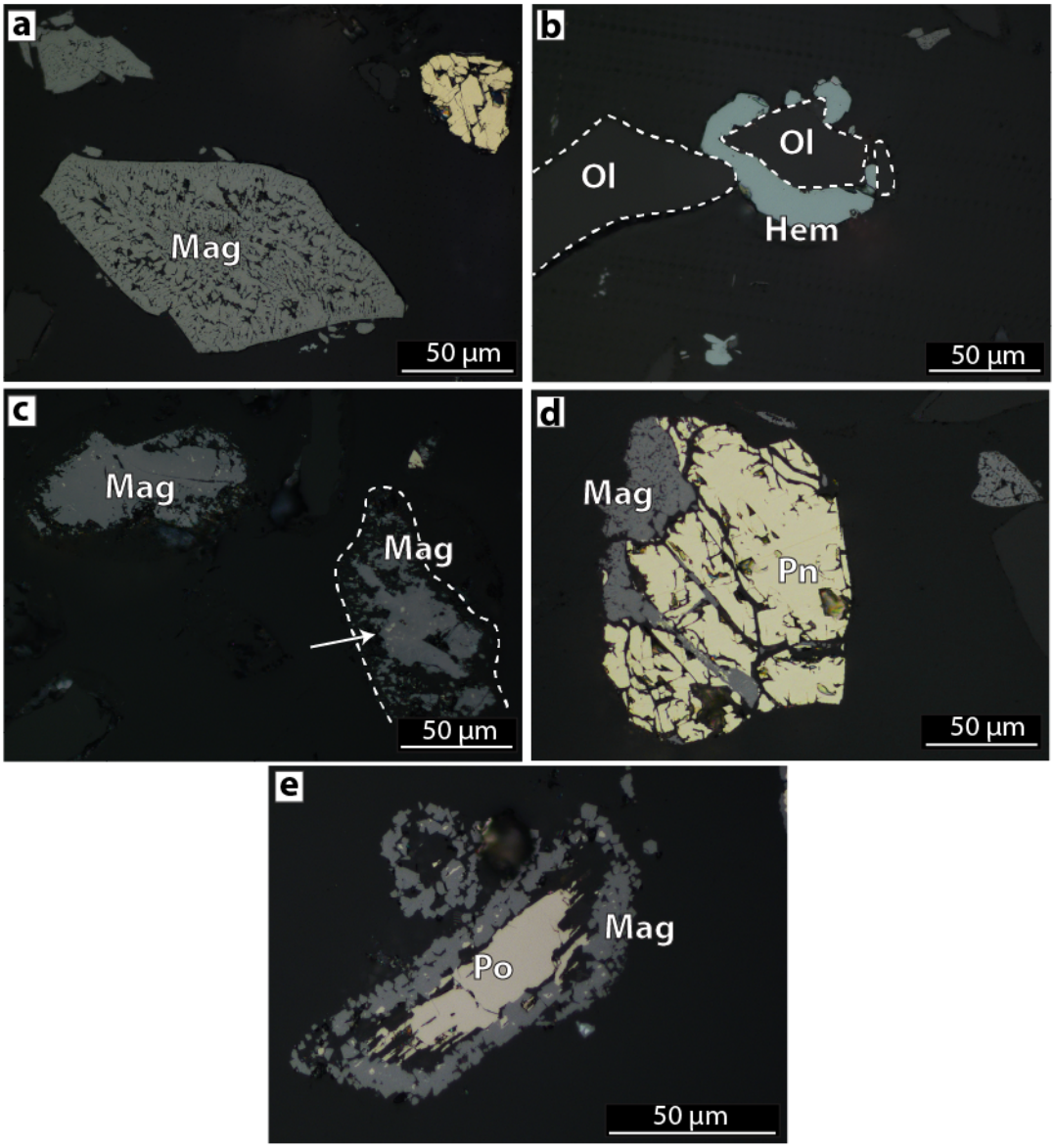

Figure 3.3: Reflected light images of pyrrhotite and pentlandite textures. (a) Magnetite texture after pyrrhotite in batch reactor experiments, exp. D8a. (b) Hematite mantling olivine grain in batch reactor experiment. Dashed line indicates grain boundary of olivine grains, exp. S81. (c) Magnetite after pyrrhotite in O_2-free experiments with unreacted pyrrhotite (arrow), dashed line indicates the approximate former grain boundary of pyrrhotite, exp. Parr 1. (d) Partly dissolved pentlandite grain after 167 h at 5 wt% sulphide showing newly formed magnetite, exp. S91. (e) Partly replaced pyrrhotite in experiment Lanfr6 on 100% sulphides, showing relict pyrrhotite in the core of the grain, exp. Lanfr6.

Pentlandite grains in these batch reactors runs generally showed one or more of the following changes:

1. Partial dissolution and the development of networks of microfractures. These were partially filled with precipitated magnetite and/or hematite (Fig. 3.3d).

2. Replacement by up to 25 micron thick magnetite (±hematite) mantles or coronas developed inwards from grain boundaries (Fig. 3.4). These typically contained atolls of relict pentlandite and showed arcuate boundaries with the parent pentlandite (Figure 3.4c).

3. Compositional modification, generally to more Ni-enriched pentlandite, but in two short duration runs (S89, S90), a slight decrease in Ni content relative to the starting material (Table 3.3).

4. Partial or complete replacement by patches and fronts of heazlewoodite (Ni_3S_2) or millerite (NiS; Fig. 3.4). The replacement sulphides were identified by a combination of EMP, EDS analysis (Table 3.4) and reflected light microscopy. Heazlewoodite was observed in the short duration (<94 hr) batch reactions, while millerite predominated as a replacement sulphide in the longer duration runs (Fig. 3.4; Table 3.1). In most of the latter runs, completely replacement of pentlandite by millerite had occurred, while preserving the original {111} pentlandite cleavage. The millerite showed the development of a fine, submicron porosity (Fig. 3.4) and arcuate boundaries with pentlandite starting material.

Experiments on sulphide:silicate of 40:60 weight ratio did not show a compositional change of the residual pentlandite and exhibited only minor dissolution.

Batch reactor experiments on 100 wt% sulphide without silicates resulted in a completely different alteration product for pentlandite. The pentlandite grains in these runs (Lanfr5; Lanfr6; Table 3.1) showed replacement by a Ni-rich pentlandite of 29.3 at% Ni and residual cores within the centre of the grains (Fig. 3.6) with compositions approximating the Mss(1) phase of Misra & Fleet (1973; Table 3.4).

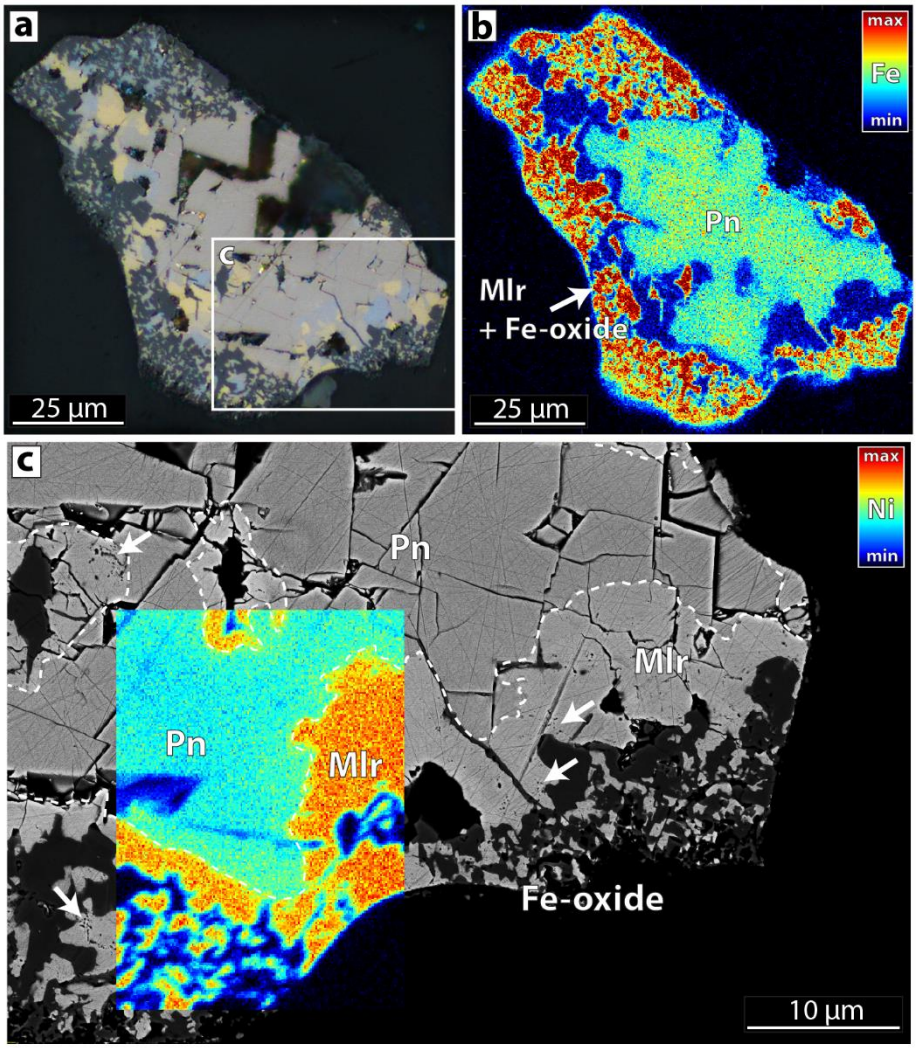

Figure 3.4: Partly reacted pentlandite, replaced by millerite and Fe-oxide, after 859 h at 5 wt% sulphide. (a) Reflected light image under crossed nicols showing characteristic blue-yellow interference colour of millerite. (b) Fe-EDS map highlighting Fe depletion and formation of Fe-oxide in the outer rim of the grain. (c) Magnified BSE image (area indicated in a) with Ni-EDS overlay. Millerite exhibits sharp contact towards the pentlandite host as well as porosity (arrows).

Pyrite in the Lanfranchi sulphide and olivine starting mixtures showed no sign of dissolution or reaction in our batch reactor experiments. Some microfractures in pyrite were observed encrusted with magnetite crystals. Chalcopyrite grains showed complete replacement by bornite with Cu-sulphide lamellae. Varying the forsterite content of the olivine in the starting mixtures by using San Carlos (Fo89) rather than

Twin Sisters (Fo92) resulted in no discernible difference in the textures or compositions of the reaction products (Table 3.1).

A single run (Parr1) consisting of a 20:80 Lanfranchi sulphide:silicate starting mixture was conducted under oxygen-free conditions in the Parr reactor vessel for 835 hours (Table 3.1). In this run, hematite was only observed in minute amounts intergrown with magnetite. Magnetite grains formed after pyrrhotite in the O_2-free experiments were free of porosity in the core of the grains but exhibited isolated patches (<1 μm) of relict pyrrhotite and irregular boundaries (Fig. 3.3c). Pentlandite showed partial replacement by heazlewoodite as patch-like domains to 20 microns developed inward from grain boundaries (Fig. 3.5) and an increase in Ni content in the residual pentlandite.

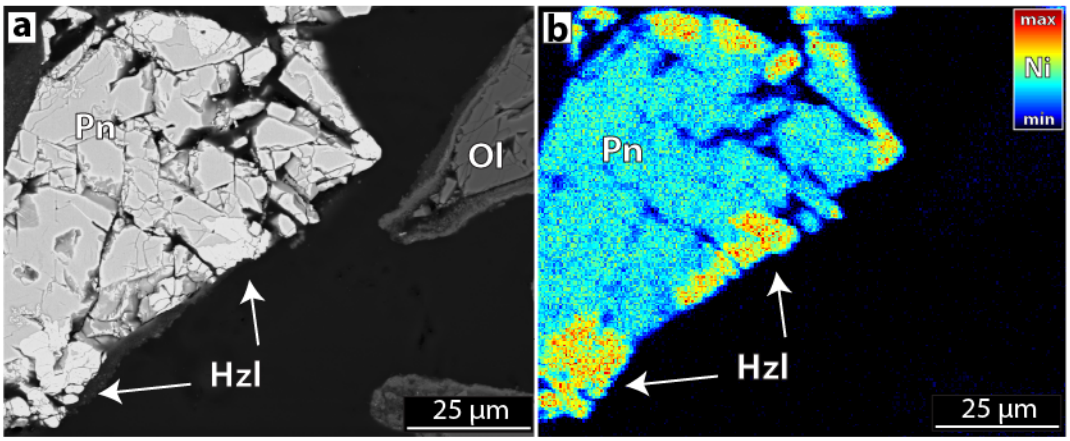

Figure 3.5: Pentlandite replacement by heazlewoodite in O_2 free run after 836 h (Parr1). (a) Heazlewoodite shows weak difference in z-contrast. One partly serpentinised olivine grain is visible on the right. (b) Ni-EDS map showing Ni enriched areas of heazlewoodite composition, see also Table 3.4.

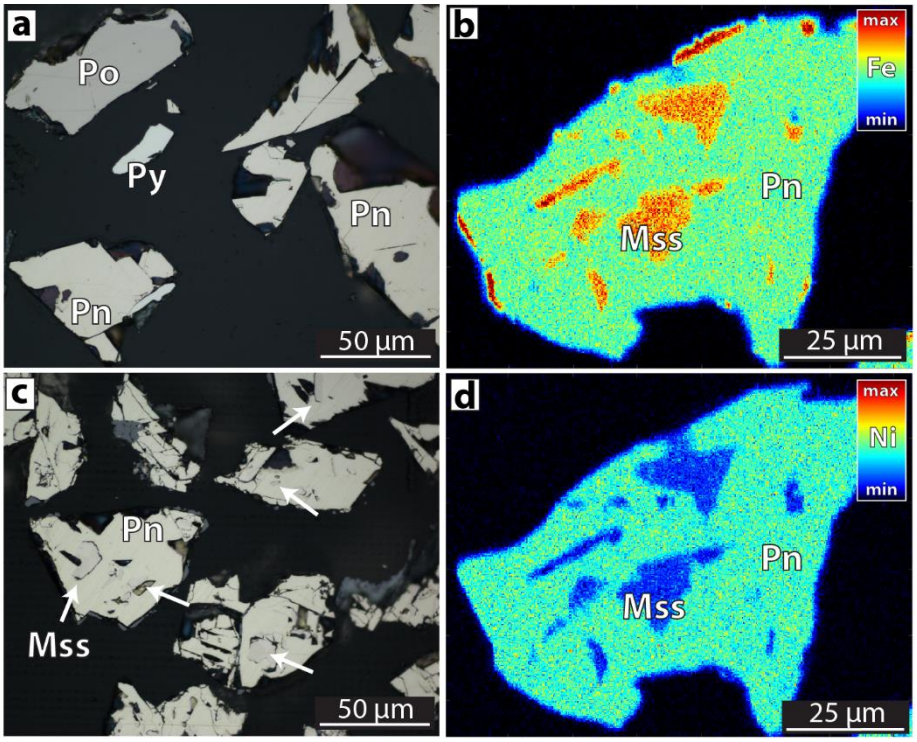

Figure 3.6: (a) Unreacted pentlandite-pyrrhotite-pyrite Starting material. (b) Silicate free experiment producing Mss exsolution (arrows), after 835 h. (c) Fe-EDS map of pentlandite grain with Mss exsolution. Note higher Fe contents at the grain boundary corresponding to magnetite (d) Fe-EDS map of pentlandite grain with Mss exsolution. See Table 3.4 for Mss composition.

3.4.2 Serpentinisation of Kambalda pentlandite and olivine mixtures

Mixtures of Kambalda pentlandite separate and olivine in a weight ratio of 20:80 were serpentinised in the Teflon lined stainless steel batch reactors at 240°C. Experimental durations were 329 and 833 hours (Table 3.1). The pentlandite separate was also run under the same conditions without silicates for the same durations (runs Pent1 and Pent2).

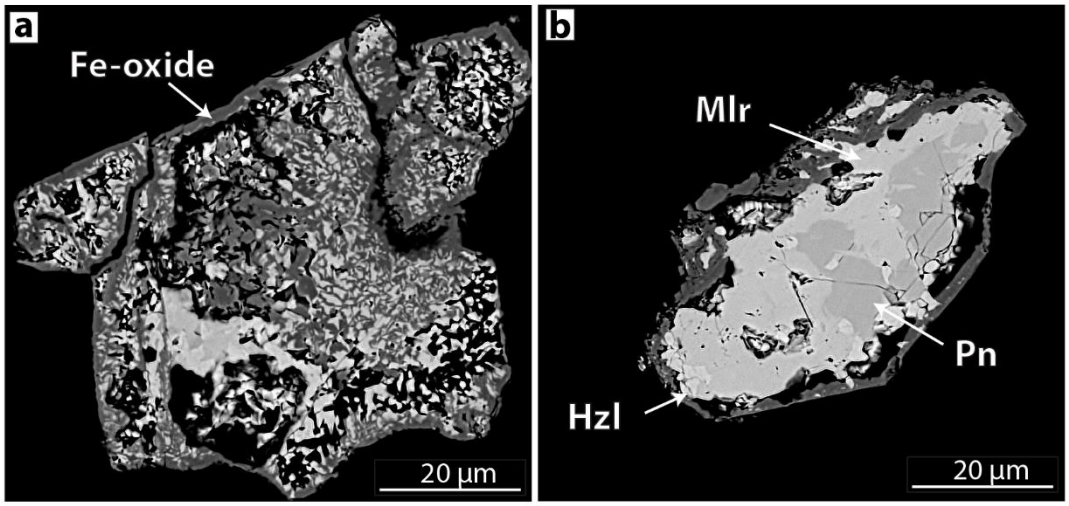

Figure 3.7: (a) Fine-grained intergrowth of Fe-oxide and Ni-sulphide and (b) co-occurrence of pentlandite, millerite and heazlewoodite in experiments on pentlandite concentrate + silicate, after 833 h.

Run products of the Kambalda pentlandite-olivine mixtures showed evidence of the formation of replacement coronas of hematite and magnetite around most pentlandite grains (Fig. 3.7), but large hematite crystals were scarce. Replacement of pentlandite inward from grain boundaries was more pronounced and the development of a network of cracks (seen in the Lanfranchi runs) was less evident. In the cores of some grains, a fine vermicular intergrowth of Ni-sulphide and magnetite was present (Fig. 3.7a), while other pentlandite grains from the same run seemed to be armoured by the development of a Fe-oxide corona, and did not react any further. The different degrees of alteration were accompanied by variations in the Ni-contents of residual pentlandite within and between runs, as measured by EMP, but a general trend of enrichment in the residual pentlandite up to 34.5 at% Ni over time was apparent. In

contrast to the Lanfranchi batch reactor experiments containing pyrrhotite and pyrite in starting material, heazlewoodite as patch-like anhedral bodies was observed as a replacement of pentlandite in all runs of the Kambalda pentlandite-olivine mixtures. In the longer duration runs (833 hours), millerite replacements of pentlandite were observed in addition to heazlewoodite, and in some grains co-existing pentlandite, heazlewoodite and millerite were observed (Fig. 3.7b and 3.8).

The batch reactor experiments on 100 wt% Kambalda pentlandite without silicates resulted in no significant compositional or textural changes to the reactant pentlandite. Minor Fe-oxide formation was observed after 833 hours of reaction, which may have been related to the presence of minor contaminant pyrrhotite in the starting material.

Varying the forsterite content of the olivine in the starting mixtures by using San Carlos (Fo89) rather than Twin Sisters (Fo92) resulted in no discernible difference in the textures or compositions of the reaction products (Table 3.1).

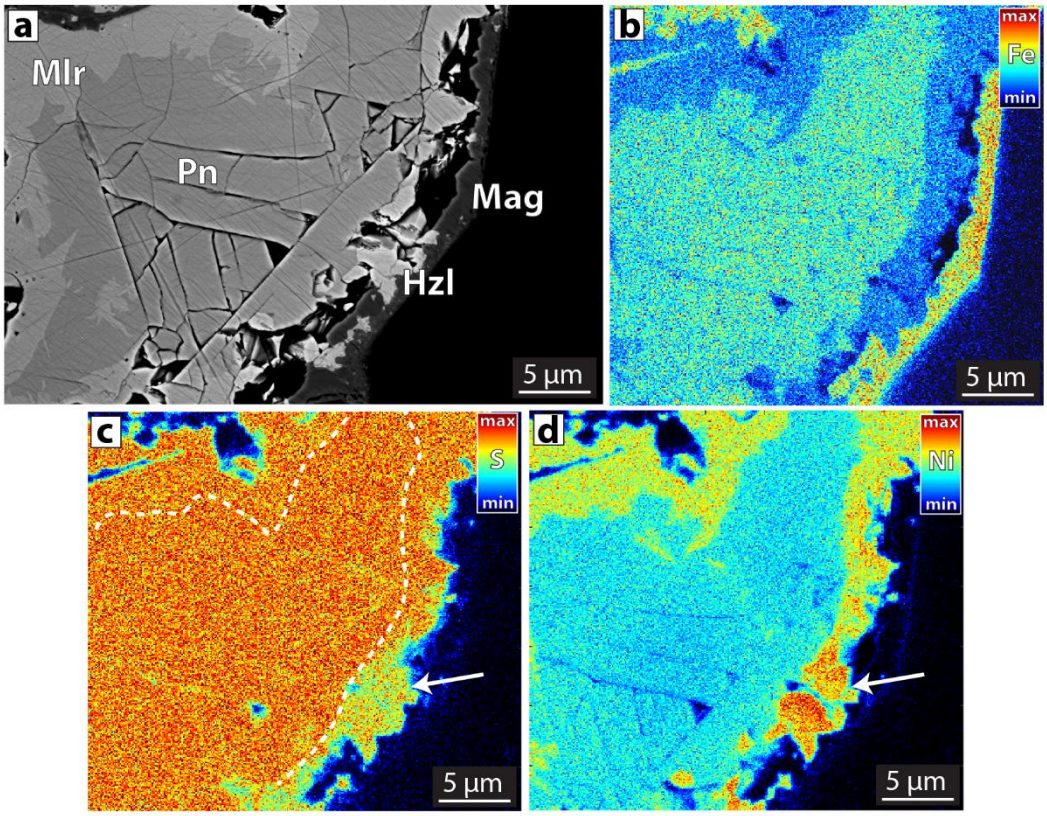

Figure 3.8: (a) BSE image of reacted pentlandite grain after 833 h using pentlandite concentrate + silicate. (b – d) EDS maps for Fe, Ni and S of the same area. Magnetite rims shows high intensities in Fe (b), whereas the reaction products millerite and heazlewoodite show lower concentrations of Fe along the replaced rim. (c) Sulphur intensities of pentlandite and millerite are indistinguishable from another (dashed line indicates border), whereas heazlewoodite shows lower intensities (arrow). (d) Ni intensities is increased in millerite over pentlandite and highest in heazlewoodite.

3.4.3 Fluid Compositions

Measured fluid compositions for all experimental runs are given in Table 3.5. The fluid pH was found to decrease with both experimental duration and initial sulphide content, and this tendency to acidity was more pronounced in runs containing pyrrhotite. Sulphur concentrations in reacted fluids were between 2.5 and 14.0 mmol/l. Iron concentrations were mostly below the detection limit of 0.002 mmol/l. Nickel concentrations varied from below detection limit of 0.034 µmol/l to 1.02 mmol/l and showed no clear correlation with other experimental variables.

Table 3.3: Measured compositions of residual pentlandite after the experiment

Sample	S89		S90		S91		S86		S82		D8a		Lanfr5		S96		S97		D9a	
n	7		4		5		5		4		2		4		9		21		3	
	Mean	SD	Mean	SD	Mean	SD	Mean	SD	Mean	SD	Mean	SD	Mean	SD	Mean	SD	Mean	SD	Mean	SD
S wt%	33.44	0.26	33.36	0.07	32.83	0.55	33.52	0.10	33.58	0.09	33.45	0.14	33.70	0.28	32.98	0.81	33.10	0.47	33.68	0.34
Fe wt%	33.47	0.59	32.96	0.62	29.41	1.87	25.77	3.19	30.44	0.10	28.36	0.54	28.01	0.83	28.50	4.83	21.97	3.99	30.12	2.21
Cu wt%	0.06	0.02	0.14	0.01	0.18	0.04	0.10	0.08	0.10	0.02	0.12	0.01	0.02	0.01	0.13	0.03	0.10	0.04	0.15	0.05
Ni wt%	32.00	0.59	32.56	0.30	37.12	2.18	39.65	3.31	35.24	0.12	36.93	0.46	37.66	0.75	37.96	4.98	44.13	3.73	36.34	3.80
Co wt%	0.29	0.05	0.08	0.15	0.21	0.02	0.19	0.04	0.18	0.06	0.19	0.06	0.26	0.03	0.67	0.69	0.73	0.37	0.40	0.02
Total	99.30	0.20	99.11	0.31	99.78	0.89	99.28	0.27	99.57	0.23	99.07	0.30	99.70	0.40	100.26	1.04	100.05	0.76	100.72	1.36
S at%	47.67		47.61		46.91		47.91		47.76		47.84		47.90		47.06		47.40		47.55	
Fe at%	27.40		27.01		24.12		21.14		24.86		23.29		22.86		23.35		18.06		24.41	
Ni at%	24.93		25.39		28.97		30.95		27.39		28.86		29.25		29.60		34.53		28.03	

Table 3.3 continued

D10a		Pent 1		Pent 2		Parr 1	
5		8		9		8	
Mean	SD	Mean	SD	Mean	SD	Mean	SD
32.95	0.30	33.25	0.13	33.28	0.05	33.17	0.43
23.52	6.48	33.10	0.59	33.16	0.53	23.33	0.84
0.11	0.04	0.19	0.03	0.33	0.02	0.52	0.60
43.17	6.04	32.22	0.50	31.93	0.28	41.10	0.56
0.86	0.50	0.42	0.02	0.43	0.01	0.39	0.16
100.64	0.45	99.18	0.26	99.15	0.31	98.90	0.59
47.04		47.60		47.70		48.05	
19.28		27.20		27.29		19.41	
33.68		25.20		25.01		32.54	

Table 3.4: Chemical composition of replacement products

	Mss		Mlr		Hzl	
n	1		7		5	
	Mean	SD	Mean	SD	Mean	SD
S wt%	37.81	-	33.56	1.04	27.65	0.54
Fe wt%	37.38	-	3.70	1.04	2.32	0.68
Cu wt%	0.00	-	0.11	0.02	0.56	0.35
Ni wt%	20.40	-	61.54	1.23	69.57	1.35
Co wt%	0.22	-	0.38	0.22	0.03	0.04
Total	95.81	-	99.28	0.82	100.12	1.33
S at%	53.61		48.21		41.03	
Fe at%	30.43		3.05		1.97	
Ni at%	15.79		48.29		56.39	

Table 3.5: Measured fluid composition after the experiments

Experiment	Time	pH	Al	Ca	Fe	Mg	Na	Ni	Si	S
	(h)	25 °C	(mmol/l)							
Pentlandite - Pyrrhotite - Pyrite										
S89	49	12.45	0.019	0.045	0.013	< 0.21	381	0.0006	0.51	4.68
S90	94	12.45	< 0.019	0.035	< 0.002	< 0.21	368	0.0001	0.39	4.99
S91	167	12.45	< 0.019	0.032	< 0.002	< 0.21	408	0.0004	0.35	3.43
S81	307	12.44	< 0.019	0.060	0.004	< 0.21	461	0.0037	0.31	6.24
S102	835	12.42	< 0.019	0.077	0.002	< 0.21	431	< 0.034	0.27	14.03
S86	328	12.45	< 0.019	0.040	0.004	< 0.21	411	0.0051	0.26	5.30
S75	856	NA	< 0.019	0.030	0.004	< 0.21	518	0.0007	0.16	6.86
S82	307	12.34	< 0.019	0.045	0.021	< 0.21	439	0.0191	0.27	4.37
S103	835	12.14	< 0.019	0.067	0.002	< 0.21	683	1.0223	0.28	5.92
D12a	859	12.50	0.019	0.067	0.004	< 0.21	505	0.3408	0.20	10.29
D8a	328	12.43	< 0.019	0.050	< 0.002	< 0.21	416	0.0005	0.11	4.05
D11a	833	12.35	< 0.019	0.047	< 0.002	< 0.21	522	0.0001	0.11	13.10
D13a	859	12.06	< 0.019	0.072	0.004	< 0.21	496	1.0223	0.17	4.68
Lanfr5	328	11.65	0.311	0.067	0.020	< 0.21	457	0.0030	0.07	2.49
Lanfr6	835	11.65	0.271	0.055	0.004	< 0.21	500	< 0.034	0.16	4.05
Parr1	836	12.46	0.004	0.008	0.001	0.002	866	0.0426	0.46	11.23
Pentlandite										
S96	329	12.46	0.022	0.052	< 0.002	< 0.21	414	0.0021	0.25	3.74
S97	833	12.46	< 0.019	0.045	< 0.002	< 0.21	444	0.0001	0.20	5.30
D9a	329	NA	< 0.019	0.047	< 0.002	< 0.21	411	0.0000	0.12	4.99
D10a	833	12.33	< 0.019	0.050	< 0.002	< 0.21	461	0.0001	0.12	5.92
Pent 1	329	12.43	0.052	0.077	< 0.002	< 0.21	373	0.0007	0.11	3.74
Pent 2	833	12.36	0.159	0.070	0.002	< 0.21	513	0.0004	0.09	6.55

3.5 Discussion

3.5.1 Alteration textures

Our hydrothermal experiments resulted in the formation of high Ni tenor sulphide assemblages containing heazlewoodite and millerite attending the serpentinisation of an ultramafic silicate assemblage. Alteration of primary sulphides occurred concurrently to serpentinisation of the silicate material, although the extent of serpentinisation was not directly determined, it is estimated to be in the range of 20% to 40% based on previous studies on serpentinisation of olivine in alkaline solutions (Lafay et al., 2012). Primary pyrrhotite and pentlandite were replaced by magnetite and hematite resulting in an increase of Ni in the remaining sulphide fraction and a fluid enriched in sulphur. This is in perfect agreement with petrographic observations for natural samples and the proposed process of Ni-tenor increase through natural hydrothermal alteration of low grade Ni-sulphide deposits (Grguric et al., 2006; Konnunaho et al., 2013). Ni-sulphides in disseminated deposits are often associated with abundant magnetite, interpreted to be formed from the oxidation of Fe component of Ni-sulphides, as shown in Figure 3.9 a-c, for different degrees of alteration of the host rock (serpentine – serpentine/carbonate). Our experiments on a primary magmatic assemblage consisting of pentlandite, pyrrhotite and pyrite produced textural features of iron oxides cross-cutting pentlandite and millerite and partly filling cracks and fractures (e.g. Fig. 3.9 d-f). These textures replicate those found in nature (e.g. Duluth, Mount Keith, Yakabindie) which with the cross-cutting magnetite has been termed ‘crossbars’ (Fig. 3.9 b)(Grguric, 2002; Grguric et al., 2013; Rosengren et al., 2007). The elevated sulphur concentrations in experimental fluids fit well with natural observations of S-loss during the alteration of this type deposits (e.g. Gole, 2008; 2014; Konnunaho et al., 2013) and desulphurisation during serpentinisation (Klein and Bach, 2009).

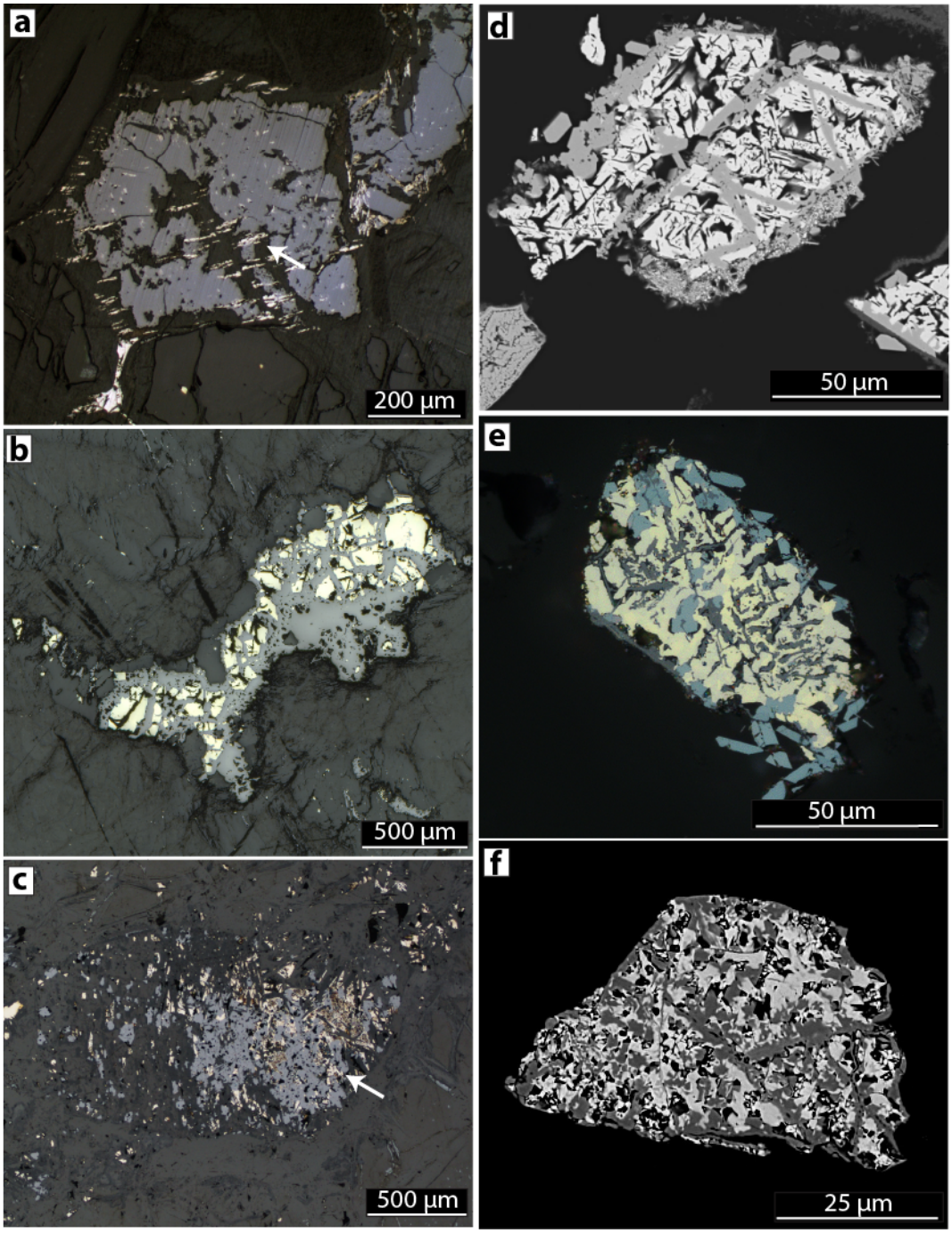

Figure 3.9: (a - c) Natural Ni-sulphide ore textures from three different deposits. (a) Reflected light image of magnetite (light grey) replacing primary sulphides in partly serpentinised matrix with relict pentlandite remaining (arrow), Panton Deposit, Western Australia, modified from (Beinlich et al., in revision). (b) Reflected light image of primary sulphide replaced by millerite and magnetite (light grey) in serpentine matrix and minor carbonates (dark grey), Mt. Keith Deposit, Western Australia. (c) Reflected light image of magnetite (light grey) with millerite, pyrite and pentlandite (arrow) in serpentine carbonate matrix (dark grey), Black Swan Deposit, Western Australia. (d -f) Experimental textures of replaced pentlandite from this study, showing millerite and magnetite ± hematite replacing pentlandite, (d and f) BSE image and (e) reflected light image.

3.5.2 Replacement mechanism and pentlandite composition

Most of our experimental runs containing pyrrhotite led to its complete replacement by magnetite. The observed textures resemble those of other experimental studies on pyrrhotite in which a replacement by dissolution reprecipitation mechanism was invoked (e.g. Qian et al., 2011). Residual pyrrhotite surrounded by magnetite coronas exhibited voids between reaction rims and unreacted pyrrhotite, consistent with precipitation being the rate limited step of the reaction (Altree-Williams et al., 2015). These textural features support a dissolution reprecipitation process for pyrrhotite in our experiments, as reported for other experimental studies on similar systems such as the Fe-Ni-Cu sulphides (Tenailleau et al., 2006; Qian et al., 2011; Zhao et al., 2014). The transformation to magnetite was completed after 49 hours in our experiments. This observation is in stark contrast to previous studies, which found general decreasing reaction kinetics with pH increase (Belzile et al., 2004; Qian et al., 2011), and found no reaction product after 1320 h at 190°C in alkaline fluid for the replacement reaction of pyrrhotite by pyrite/marcasite (Qian et al., 2011).

Pentlandite grains in our experiments showed evidence of obvious dissolution at contacts with the fluid, progressing with experimental duration and accompanied by significant compositional changes to lower and higher Ni-contents, depending on reaction time and sulphide:silicate ratio. The replacement of pentlandite by heazlewoodite occurred in patches developed inward of pentlandite grain margins and the heazlewoodite showed a sharp, generally arcuate boundary with the host pentlandite. This sharp boundary was also observed in the case of millerite partly replacing pentlandite. Furthermore, submicron porosity is observed in millerite. Identical textural features were described by Tenailleau et al. (2006) and Xia et al. (2009) in hydrothermal experiments involving the replacement of pentlandite by violarite. These workers interpreted the replacement of pentlandite by violarite as a dissolution reprecipitation reaction. At low temperature, fluid-driven replacement reactions are expected to be much faster than solid state diffusion (e.g. Ruiz-Agudo et

al., 2014), yet previous studies argued that for some mineral systems (e.g. sulphides), diffusion can still be sufficiently fast to compete with dissolution reprecipitation reactions at low temperatures (Zhao et al., 2014; Zhao et al., 2013). The formation of Mss within pentlandite in experiments on the Pn-Po-Py assemblage in the absence of silicates (runs Lanfr5 and Lanfr6) differs from the expected texture for a dissolution reprecipitation reaction, with the shape of the grain preserved but the Mss phase appearing in the centre of the grains. Thus, we interpret the formation of Mss in these runs as a result of solid state diffusion.

The reaction progress can be examined in our batch reactor experiments for mixtures of Lanfranchi sulphides and olivine, at a 5:95 ratio over an experimental duration of 49 to 835 hours. Under the given conditions, pyrrhotite was completely reacted within 49 hours and pentlandite was transformed into millerite within 307 hours, but core of residual pentlandite can still be observed after 835 hours. Heazlewoodite after pentlandite was observed for short experimental durations, suggesting this phase is likely to be metastable under the reaction conditions. The accompanied compositional Fe increase in pentlandite for short duration experiments can indicate a response to the dissolution of pyrrhotite which released a great amount of Fe within short a time, and which subsequently reacts with dissolved oxygen to form hematite with increasing run duration.

Residual pentlandite exhibited an increase in Ni-content following reaction for experiments with sulphide:olivine ratios of 20:80 (Fig. 3.10). Misra and Fleet (1973) and Grguric (2003) reported varying Ni-contents in pentlandite, dependent on the associated sulphide assemblage with a maximum of 34 at% for the Mlr-Hzl-Pn. Anders (2012) reported Ni-enrichment in hydrothermally altered pentlandite in addition to heazlewoodite formation. This is in perfect agreement with our observations that show an increase of Ni-content of pentlandite with reaction progress up to a measured 34.5 at%.

3.5.3 Replacement assemblage and 'self-buffering' mechanism

An important parameter governing the phase assemblage, that has been widely used to interpret mineral deposits, is the bulk composition of the system. The Ni-Fe-S phase relations have been extensively studied (Kullerud and Yoder, 1959; Kullerud and Yund, 1962; Naldrett et al., 1967; Kullerud, 1969; Craig, 1973; Misra and Fleet, 1973) with Mss-compositions being the focus for most studies. Our chosen sulphide starting materials (pentlandite and pentlandite-pyrrhotite-pyrite) represent two different sulphide bulk compositions (Fig. 3.10). The bulk composition of our pentlandite-pyrrhotite-pyrite assemblage resembles approximately Mss composition, whereas pentlandite represents the second composition. Previous studies (e.g. Craig 1973) observed different stable assemblages formed as a response to only slight changes in the bulk composition of the system. Thus, our observed change in sulphide assemblage in experiments exhibiting pentlandite, heazlewoodite and millerite is in good agreement with former experimental studies.

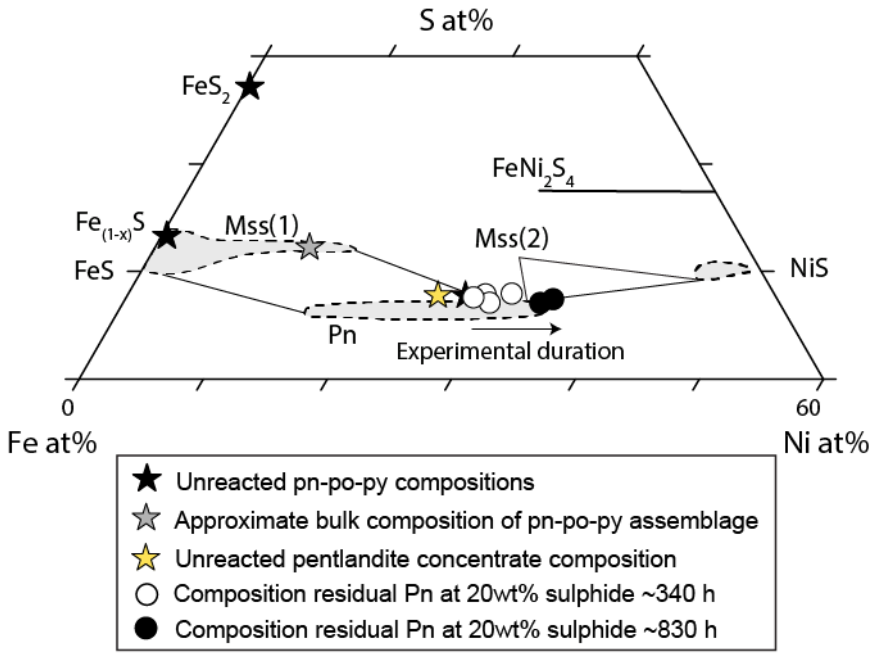

Figure 3.10: Fe-Ni-S ternary diagram section after modified after Misra and Fleet (1973). Compositions of unreacted starting material are shown as stars. Circles represent the compositional evolution of the residual pentlandite after experiments over time.

An increase in sulphide:silicate (pn-po-py assemblage) in our experiments resulted in a series of different Ni-sulphide assemblages at given experimental duration (~ 840 h). Many studies report varying Ni-tenor assemblages for disseminated Ni-sulphide deposits (e.g. Barnes and Hill, 2000; Grguric et al., 2006; Gole, 2008), whereas massive ore deposits exhibit a homogeneous assemblage with generally far less variation in the Ni tenor of individual sulphide componentss (Barnes et al., 2009). The difference in these two deposit types is effectively a change in sulphide:silicate ratio. In nature, the varying Ni-tenor assemblages are explained by the 'self-buffering' capacity of sulphides, which are able overcome the strongly reducing conditions imposed by alteration of the ultramafic host rock at increased sulphide:silicate (Eckstrand, 1975). This mechanism is in good agreement with observations from our experimental products. Low amounts of sulphide in the system (5 wt% and 20 wt%) show a transformation to high Ni-tenor sulphides, whereas an increase in sulphides (40 wt%) does not result in the transformation of pentlandite. Sulphides in experiments without silicate are unaffected by changes in fO_2 through silicate alteration, and should evolve to the assemblage stable under the imposed conditions.

Another explanation opposed to the commonly used 'self-buffering' mechanism could be a compositional change of the bulk sulphide towards a more Ni-rich and S-depleted composition of the sulphide fraction through the dissolution of sulphides. The large amount of fluid (high fluid:rock) used in our experiments can host a significant amount of sulphur but little Ni or Fe, as seen in our fluid analysis. In addition, Fe precipitates as oxides and depletes the system of Fe. The remaining sulphide fraction would thus be enriched in Ni. This effect would be most pronounced at low sulphide:silicate and high fluid/rock ratio, as in our experiments. A basic mass balance calculation suggests that the amount of S liberated by the dissolution of pyrrhotite (in experiments containing 5 wt% sulphide) could almost completely be dissolved in the 5 ml reacting fluid, at the measured S-concentration. The shift in bulk sulphide composition towards more Ni-rich compositions is in agreement with the observed Ni-rich phases after the experiments.

Although serpentinisation of ultramafic rock is known to produce highly reducing conditions, we observed hematite in the experimental products. It is not possible to determine if this only the effect of O_2 present in the initial fluid and headspace, or due to atmospheric oxygen in our experimental setup. It is likely that atmospheric O_2 inside the oven diffused through the liner material at increased temperatures. The reaction between the rock powder and fluid within the liner would create an oxygen sink thus precipitating Fe-oxides. Due to the consistent loss of water from the liner over the experimental duration, batch reactor experiments have to be interpreted as a somewhat open system. However, the presence of O_2 within the system allows us to investigate the effect of O_2 on the system compared to an O_2 free experiment (e.g. the Parr1 run). Experiments containing atmospheric oxygen in the headspace and dissolved in solution produced great quantities of hematite in addition to the formation millerite after pentlandite. In contrast, experiments without O_2 led to a great reduction of the amount of observed hematite, an absence of millerite, and heazlewoodite was observed as a replacement product of pentlandite. Co-occurring hematite and magnetite can be in equilibrium at fixed fO_2,g and both can be associated with different Ni-sulphides according to fO_2,g – fS_2,g diagrams constructed by Klein and Bach (2009). Our observations of changing Ni-sulphide assemblages from heazlewoodite to millerite with increasing fO_2 fits well with the proposed process and highlights the effect of fO_2 on the sulphide assemblage. In addition, the alkaline fluids used in our experiments are expected to have an effect on the stable assemblage as well. Xia et al. (2009) showed the increasing stability field of millerite with temperature. Thus, an increase in O_2 and the observed decrease in pH in the system forming millerite are in agreement with the calculated assemblages.

Many studies have been focused of the exchange of Ni-Fe between sulphide fraction and host olivine (Brenan, 2003; Clark & Naldrett, 1972; Fleet & MacRae, 1983, 1987, 1988; Fleet et al., 1977). This process is controlled by diffusion and thus dependent on temperature and might not be relevant for our experiments at relatively low temperature (Evans, 2010), although no chemical analysis of the unreacted olivine after experiments has been performed to show potential Ni-gradients. However, the

Ni component liberated through dissolution of olivine is likely to contribute to the Ni budget of the system, as has been shown by other studies on high Ni-olivine (Filippidis, 1982, 1985). Finely dispersed sulphide grains are the result of this reaction and also often found within serpentine after olivine in natural samples (Eckstrand, 1975; Donaldson, 1981; Grguric et al., 2006; Klein et al., 2009).

Although the fate of the Ni hosted by the silicate matrix was not investigated in our experiments, observed textures and assemblages of the replacement products (high Ni-tenor sulphide and abundant Fe-oxides) allow significant insight into the prevailing mechanism. These observations provide a strong argument for the increase in Ni-tenor through progressive replacement by non-sulphide species suggested by (Grguric, 2003: Grguric et al., 2006 & 2013; Konnunaho et al., 2013; Gole, 2014).

3.6 Conclusion

It has been shown that a primary magmatic Ni-sulphide assemblages in contact with ultramafic rock can be experimentally transformed into a high Ni-tenor assemblage using high pH fluids commonly associated with serpentinisation. Primary pyrrhotite is replaced by magnetite within 49 h at 240°C. The replacement sulphide assemblage consists of millerite ± residual pentlandite with increased Ni-content ± heazlewoodite or residual pentlandite with increased Ni-content + heazlewoodite depending on O_2 content in the system and bulk sulphide composition and silicate/sulphide. These observations give important implications for interpretations on the genesis of hydrothermally altered Ni-sulphide deposits and highlight the fast and extensive response to chemical changes in the system induced by hydrothermal fluids.

3.7 References

Altree-Williams, A., Pring, A., Ngothai, Y. and Brugger, J. 2015. Textural and compositional complexities resulting from coupled dissolution–reprecipitation reactions in geomaterials. Earth-Science Reviews, 150, 628-651.

Anders, H. 2012. Experimental investigations of interactions between saltwater and ultramafic rocks in hydrothermal systems. Doctoral dissertation, Bremen University.

Barnes, S. J. and Hill, R. E. 2000. Metamorphism of komatiite-hosted nickel sulfide deposits.

Barnes, S. J., Wells, M. A. and Verrall, M. R. 2009. Effects of magmatic processes, serpentinization, and talc-carbonate alteration on sulfide mineralogy and ore textures in the Black Swan disseminated nickel sulfide deposit, Yilgarn Craton. Economic Geology, 104(4), 539-562.

Beinlich, A., von Heydebrand, A., Klemd, R., Martin, L., Hicks, J.. Compositional variations in chromite, pentlandite, chalcopyrite and bulk rock PGE in massive chromitite due to metamorphism of the Panton Intrusion, east Kimberley, Western Australia. In revision for Ore Geology Reviews.

Belzile, N., Chen, Y.-W., Cai, M.-F. and Li, Y. 2004. A review on pyrrhotite oxidation. Journal of Geochemical Exploration, 84(2), 65-76.

Brenan, J. M. 2003. Effects of fO_2, fS_2, temperature, and melt composition on Fe-Ni exchange between olivine and sulfide liquid: implications for natural olivine–sulfide assemblages. Geochimica et Cosmochimica Acta, 67(14), 2663-2681.

Chavagnac, V., Monnin, C., Ceuleneer, G., Boulart, C. and Hoareau, G. 2013. Characterization of hyperalkaline fluids produced by low-temperature serpentinization of mantle peridotites in the Oman and Ligurian ophiolites. Geochemistry, Geophysics, Geosystems, 14(7), 2496-2522.

Clark, T. and Naldrett, A. 1972. The distribution of Fe and Ni between synthetic olivine and sulfide at 900 degrees C. Economic Geology, 67(7), 939-952.

Craig, J. R. 1973. Pyrite-pentlandite assemblages and other low temperature relations in the Fe-Ni-S system. American Journal of Science, 273(A), 496-510.

Donaldson, M. 1981. Redistribution of ore elements during serpentinization and talc-carbonate alteration of some Archean dunites, Western Australia. Economic Geology, 76(6), 1698-1713.

Eckstrand, O. 1975. The Dumont serpentinite; a model for control of nickeliferous opaque mineral assemblages by alteration reactions in ultramafic rocks. Economic Geology, 70(1), 183-201.

Evans, B. W. 2010. Lizardite versus antigorite serpentinite: Magnetite, hydrogen, and life (?). Geology, 38(10), 879-882.

Filippidis, A. 1982. Experimental study of the serpentinization of Mg-Fe-Ni olivine in the presence of sulfur. The Canadian Mineralogist, 20(4), 567-574.

Filippidis, A. 1985. Formation of awaruite in the system Ni-Fe-Mg-Si-OHS and olivine hydration with NaOH solution, an experimental study. Economic Geology, 80(7), 1974-1980.

Fleet, M. and MacRae, N. 1983. Partition of Ni between olivine and sulfide and its application to Ni-Cu sulfide deposits. Contributions to Mineralogy and Petrology, 83(1-2), 75-81.

Fleet, M. and MacRae, N. 1987. Partition of Ni between olivine and sulfide: the effect of temperature. Contributions to Mineralogy and Petrology, 95(3), 336-342.

Fleet, M. and MacRae, N. 1988. Partition of Ni between olivine and sulfide: equilibria with sulfide-oxide liquids. Contributions to Mineralogy and Petrology, 100(4), 462-469.

Fleet, M., MacRae, N. and Herzberg, C. 1977. Partition of nickel between olivine and sulfide: A test for immiscible sulfide liquids. Contributions to Mineralogy and Petrology, 65(2), 191-197.

Frost, B. R. and Beard, J. S. 2007. On silica activity and serpentinization. Journal of Petrology, 48(7), 1351-1368.

Gole, M. 2008. Metasomatic interaction between disseminated nickel sulphides and reduced metamorphic fluids, Honeymoon Well komatiite complex, Western Australia. Applied Earth Science, 117(3), 112-124.

Gole, M. J. 2014. Leaching of S, Cu, and Fe from disseminated Ni-(Fe)-(Cu) sulphide ore during serpentinization of dunite host rocks at Mount Keith, Agnew-Wiluna Belt, Western Australia. Mineralium Deposita, 49(7), 821-842.

Grguric, B. 2002. Hypogene violarite of exsolution origin from Mount Keith, Western Australia: field evidence for a stable pentlandite− violarite tie line: De Gruyter.

Grguric, B. 2003. Minerals of the MKD5 nickel deposit, Mount Keith, Western Australia. Australian Journal of Mineralogy, 9, 55-71.

Grguric, B., Madsen, I. and Pring, A. 2001. Woodallite, a new chromium analogue of iowaite from the Mount Keith nickel deposit, Western Australia. Mineralogical Magazine, 65(3), 427-435.

Grguric, B., Rosengren, N., Fletcher, C. and Hronsky, J. 2006. Type 2 deposits: Geology, mineralogy, and processing of the Mount Keith and Yakabindie orebodies, Western Australia. Special Publication-Society of Economic Geologists, 13, 119.

Grguric, B. A., Seat, Z., Karpuzov, A. A. and Simonov, O. N. 2013. The West Jordan deposit, a newly-discovered type 2 dunite-hosted nickel sulphide system in the northern Agnew–Wiluna belt, Western Australia. Ore Geology Reviews, 51, 79-92.

Groves, D., Hudson, D. and Hack, T. 1974. Modification of iron-nickel sulfides during serpentinization and talc-carbonate alteration at Black Swan, Western Australia. Economic Geology, 69(8), 1265-1281.

Klein, F. and Bach, W. 2009. Fe–Ni–Co–O–S phase relations in peridotite–seawater interactions. Journal of Petrology, 50(1), 37-59.

Klein, F., Bach, W., Jöns, N., McCollom, T., Moskowitz, B. and Berquó, T. 2009. Iron partitioning and hydrogen generation during serpentinization of abyssal peridotites from 15 N on the Mid-Atlantic Ridge. Geochimica et Cosmochimica Acta 73, 6868-6893.

Konnunaho, J., Hanski, E., Bekker, A., Halkoaho, T., Hiebert, R. and Wing, B. 2013. The Archean komatiite-hosted, PGE-bearing Ni–Cu sulfide deposit at Vaara, eastern Finland: evidence for assimilation of external sulfur and post-depositional desulfurization. Mineralium Deposita, 48(8), 967-989.

Kullerud, G. 1969. Phase relations in the Cu-Fe-S, Cu-Ni-S and Fe-Ni-S system. Magmatic ore deposits, 323-343.

Kullerud, G. and Yoder, H. S. 1959. Pyrite stability relations in the Fe-S system. Economic Geology, 54(4), 533-572.

Kullerud, G. and Yund, R. A. 1962. The Ni-S system and related minerals. Journal of Petrology, 3(1), 126-175.

Lafay, R., Montes-Hernandez, G., Janots, E., Chiriac, R., Findling, N. and Toche, F. 2012. Mineral replacement rate of olivine by chrysotile and brucite under high alkaline conditions. Journal of Crystal Growth, 347(1), 62-72.

Misra, K. and Fleet, M. 1973. The chemical compositions of synthetic and natural pentlandite assemblages. Economic Geology, 68(4), 518-539.

Naldrett, A., Craig, J. and Kullerud, G. 1967. The central portion of the Fe-Ni-S system and its bearing on pentlandite exsolution in iron-nickel sulfide ores. Economic Geology, 62(6), 826-847.

Qian, G., Xia, F., Brugger, J., Skinner, W. M., Bei, J., Chen, G. and Pring, A. 2011. Replacement of pyrrhotite by pyrite and marcasite under hydrothermal conditions up to 220 C: An experimental study of reaction textures and mechanisms. American Mineralogist, 96(11-12), 1878-1893.

Rosengren, N., Grguric, B., Beresford, S., Fiorentini, M. and Cas, R. 2007. Internal stratigraphic architecture of the komatiitic dunite-hosted MKD5 disseminated nickel sulfide deposit, Mount Keith Domain, Agnew-Wiluna greenstone belt, Western Australia. Mineralium Deposita, 42(8), 821-845.

Ruiz-Agudo, E., Putnis, C. and Putnis, A. 2014. Coupled dissolution and precipitation at mineral–fluid interfaces. Chemical geology, 383, 132-146.

Sciortino, M., Mungall, J. E. and Muinonen, J. 2015. Generation of High-Ni sulfide and alloy phases during serpentinization of dunite in the Dumont sill, Quebec. Economic Geology, 110(3), 733-761.

Stueber, A., Huang, W. and Johns, W. 1968. Chlorine and fluorine abundances in ultramafic rocks. Geochimica et Cosmochimica Acta, 32(3), 353-358.

Tenailleau, C., Pring, A., Etschmann, B., Brugger, J., Grguric, B. and Putnis, A. 2006. Transformation of pentlandite to violarite under mild hydrothermal conditions. American Mineralogist, 91(4), 706-709.

Xia, F., Brugger, J., Chen, G., Ngothai, Y., O'Neill, B., Putnis, A. and Pring, A. 2009. Mechanism and kinetics of pseudomorphic mineral replacement reactions: A case study of the replacement of pentlandite by violarite. Geochimica et Cosmochimica Acta, 73(7), 1945-1969.

Zhao, J., Brugger, J., Ngothai, Y. and Pring, A. 2014. The replacement of chalcopyrite by bornite under hydrothermal conditions. American Mineralogist, 99(11-12), 2389-2397.

Zhao, J., Brugger, J., Xia, F., Ngothai, Y., Chen, G. and Pring, A. 2013. Dissolution-reprecipitation vs. solid-state diffusion: Mechanism of mineral transformations in sylvanite,(AuAg) 2Te4, under hydrothermal conditions. American Mineralogist, 98(1), 19-32.

Chapter 4

Effect of hematite on the textural evolution during the replacement of ilmenite by rutile

A modified version of this manuscript is in preparation for submission to a scientific journal.

Tobias Wengorsch, Andreas Beinlich, Andrew Putnis

4.1 Abstract

The understanding of the chemical behaviour of ilmenite is of interest for both, natural alteration under crustal / surface conditions and mineral processing for industrial applications, as ilmenite represents an important mineral in igneous and metamorphic rocks and the most important source of titanium for TiO_2 particle production. The fluid driven replacement mechanism was investigated by batch reactor experiments of ilmenite cubes with pre-existing hematite exsolution lamellae in acidic solutions of 0.1 M and 3 M HCl at 150 °C. Formation of secondary rutile and the development of a coarse network of porosity throughout the volume of the cube was observed. The generation of porosity was aided by the preceding selective dissolution of connected hematite lamellae visualized by focused ion beam tomography. This observation is in contrast to reported results from literature, as the development of hierarchical fractures was not observed in our experiments. This is expected to have major implications for rock properties, such as permeability, as the alteration at low acid concentration only affects the margin and areas exposed through pre-existing cracks for ilmenite with hematite lamellae, whereas the alteration of pure ilmenite develops a large network of fractures. Furthermore, the dissolution of hematite effectively reduced contents of trace elements such as vanadium and chromium in the remaining solid fraction.

4.2 Introduction

Ilmenite is an economically important mineral and embodies the main ore for TiO_2 particle production, which is of great demand for the paint industry. Large quantities of ilmenite can be found in coastal placer deposits as well as in magmatic settings like Tellnes Deposit, Norway (e.g. Bruckard et al., 2015; Charlier et al., 2006; Charlier et al., 2007). While magmatic deposits show mostly homogeneous mineralogy, ilmenite from placer deposits has been exposed to earth surface conditions for long periods of time and is thus commonly altered. These alterations at earth surface conditions generally lead to an enrichment of the Ti component, but also enrich the residual

grains in trace elements (Grey et al., 2005; Pownceby, 2010), especially at late stages of the alteration (Frost et al., 1983). Apart from weathering at surface conditions, oxides minerals such as ilmenite can be considerably altered by hydrothermal fluids under metamorphic conditions as observed in natural samples and experiments (Angiboust and Harlov, 2017; Pochon et al., 2017). Natural ilmenite often shows subsolidus hematite exsolution, which may be completely or partially dissolved, while the residual ilmenite remains unaffected (e.g. Craig, 2001; Darby, 1984). Hematite in ilmenite is also of interest as it controls the magnetic properties of the composite material and has thus important implications for remote sensing (Kletetschka et al., 2002; McEnroe et al., 2002; McEnroe et al., 2007). The alteration of single phase ilmenite (Ti/(Ti+Fe) ratio of ≤0.5) has been described to initiate with the formation of hydrated ilmenite (Ti/(Ti+Fe) ratio of 0.5 to 0.6) followed by pseudorutile (Ti/(Ti+Fe) ratio of 0.6 to 0.7) and end at leucoxene (Ti/(Ti+Fe) ratio of 0.7 to 0.9) or hydroxylian pseudorutile with pseudorutite-like structure but leucoxene composition (Grey and Li, 2003; Pownceby, 2010). Many studies investigated the alteration process of ilmenite. The accepted model states that the Fe component is completely oxidized and partly removed from the crystal lattice by diffusion to from pseudorutile (Grey and Li, 2003; Grey and Reid, 1975; Schroeder et al., 2002; Temple, 1966). However, Janssen et al. (2010) showed, that for high pH conditions, the replacement of ilmenite by rutile proceeds via a coupled dissolution reprecipitation reaction in which the host ilmenite is dissolved before the Ti-phase is precipitated. The replacement initiates at the contact between solid and fluid and develops a random network of fractures that can reach far into the ilmenite material. This experimental method is also used in hydrothermal processing of ilmenite ore.

Two different approaches are used for the production of TiO_2 particles. The first is the sulphate route which involves the complete dissolution of ilmenite in sulphuric acid (e.g. Gázquez et al., 2014; Nguyen and Lee, 2019). Subsequently, the iron component is precipitated from solution with the Ti rich solution remaining for further purification and precipitation of TiO_2. The downside of this process is the generation of large amounts of acid waste. The second approach is the chlorination route which

requires a high grade Ti-feedstock and accounts for about 60% of the world's TiO_2 production (Gázquez et al., 2014). The material is transferred into gaseous $TiCl_4$ which is used to produce TiO_2 of high quality. This process produces a higher quality product, less waste and lower environmental impact compared to the sulphate route. However, due to the sensitivity of this process to impurity elements such as Si and Mg, the starting material has to be carefully controlled and of high Ti-content (Jena et al., 1995; Stanaway, 1994). Ilmenite has replaced rutile as the most important Ti ore because of its natural abundance (Itoh et al., 2006). However, in order to meet the requirements for the chlorination route, ilmenite has to undergo preprocessing (Habashi et al., 2014; Mackey, 1994). Different methods have been developed to make the use of ilmenite viable, many of which involve the reduction of the material, such as the Becher process. Alternatively, Ti-rich slag can be used as a feedstock material, produced by smelting (e.g. Gueguin and Cardarelli, 2007). In addition, ilmenite can be upgraded by hydrothermal treatment (Nguyen and Lee, 2019). The ground material is exposed to concentrated hydrochloric acid at elevated temperature to remove the iron component of the ilmenite and form a secondary phase called synthetic rutile (Mahmoud et al., 2004; Van Dyk et al., 2002). Synthetic rutile exhibits higher concentrations of TiO_2 compared to the precursor ilmenite and is used for the subsequent production of TiO_2 particle via the chlorination route (Zhang et al., 2011). Previous studies focussed on the reaction kinetics and chemical compositions of the reaction products and found solid/acid ratio, acid concentration, temperature, grain size and mechanical or thermal activation to be important factors controlling the reaction of ilmenite in hydrochloric acid in order to achieve a high quality feedstock (El-Hazek et al., 2007; Janssen and Putnis, 2011; Olanipekun, 1999; Ping et al., 2011; Van Dyk et al., 2002; Zhang et al., 2010; Zhang et al., 2011). Ilmenite ore contains Fe in its structure but is also often associated with exsolution lamellae of hematite. Hematite is also an important host for trivalent trace elements such as Cr and V, which affect the pigment colour of the final product (Stanaway, 1994).

The replacement of ilmenite by rutile has been described as a coupled dissolution reprecipitation mechanism (Janssen et al., 2010). The access of fluid to the reaction

front is crucial and facilitated by the formation of porosity which can be further enhanced by reaction induced fracturing (e.g. Putnis, 2009). The fracturing process generates new surfaces area which in turn increases the rate of the reaction (Jamtveit et al., 2009). Reaction induced fracturing is a common observation for many mineral replacement reactions, such as serpentinisation of olivine or the replacement of leucite by analcime (e.g. Plümper et al., 2012; Putnis et al., 2007). For the replacement of ilmenite by rutile, Janssen et al. (2010) reported the development of a network of hierarchical fractures trough the primary ilmenite which was very pronounced even at reactions with low acid concentrations. Although the exact process is poorly understood, coupled processes between different minerals in the form of intergrowths versus mechanical mixtures have been reported to influence the kinetics of the replacement reaction (Xia et al., 2007). Ilmenite is well-suited as a model system, as it is commonly observed with exsolution of hematite and also exposed to fluid induced alteration not only in nature but industrial applications. This study investigates the effect of pre-existing hematite lamellae on the reaction mechanism of rutile formation in hydrochloric acid. We employ hydrothermal alteration experiments to investigate the textural and chemical evolution of the host mineral at 0.1 M and 3 M HCl and 150 °C. Furthermore, we use focused ion beam (FIB) tomography to extract 3D textural information for the replacement front of this reaction.

4.3 Methods

An ilmenite hand specimen containing hematite lamellae from an unknown location in Norway was cut into cubes with approximate dimensions of 3 mm x 1.6 mm x 1.6.mm. The cubes were weighted and placed in 10 ml Teflon liners together with the reacting fluid, inserted into a stainless steel reactor and placed inside the oven. Experimental conditions were adopted from Janssen et al. (2010) to make a comparison possible. However, due to the size of the reaction vessel the fluid ratio of the 0.1 M HCl experiment was reduced by factor two. Two cubes were reacted with 3M HCl for 2 and 4 days, with an ilmenite to fluid mass ratio of 1:15, the third cube was reacted with 0.1 M HCl for 31 days, with a ilmenite to fluid mass ratio of 1:55 at

a temperature of 150 °C. At the end of an experiment reactors were placed on a ceramic plate to cool down to room temperature over a duration of 1.5 hours. The reacted cubes were washed in distilled water, dried at 100 °C and weighted. Subsequently, cubes were embedded in 1 inch epoxy resin mounts, cut and polished perpendicular to the longest axis to approximately half the cubes thickness (0.8 mm) to expose cross sections.

4.3.1 SEM imaging and FIB tomography

High resolution imaging was performed on a FEI Verios XHR on Pt-coated samples at Centre for Microscopy, Characterisation and Analysis (CMCA), The University of Western Australia. Images were acquired using secondary (SE) and backscattered electrons (BSE) at an acceleration voltage of 5 kV and a beam current of 0.1 nA. An integrated Electron dispersive X-ray spectroscopy (EDS) detector was used for spot analysis and compositional mapping of small areas. For focussed ion beam (FIB) slice and view a FEI Helios SEM was used. To reduce charging during the slicing process the sample was drilled out of the epoxy mount to reduce the amount of resin, also the sample was recoated after the cutting of trenches at the site of interest. The sample was loaded into the machine at least 12 hours prior the start of the process. An area of 15 x 15 µm at 30 nm slice thickness was selected for FIB tomography, therefore images were acquired in two sessions. Images were pre-processed using Adobe Photoshop to correct for the slightly different magnifications of the two sessions and reduced in file size. The software Aviso 9.2 was used for 3D reconstruction using the Dual Beam Wizard function. Manual adjustments were made to correct for curtaining effects on acquired images.

4.3.2 Chemical composition

Chemical compositions and elemental maps were obtained by Electron microprobe analysis (EMPA) on a JEOL 8530F at CMCA on carbon coated cross sections in 1 inch resin mounts. Operating conditions were 20 keV acceleration voltage, a 20 nA beam current, 100 s peak counting time at a spot size of 1 µm. Element maps were

acquired at 20 keV and beam current of 50 nA, 1.5 µm step size and 150 ms dwell time. Corundum, periclase, wollastonite, rutile, V-metal, Cr-metal, Mn-metal, and Fe-metal were used as standard materials for analysis.

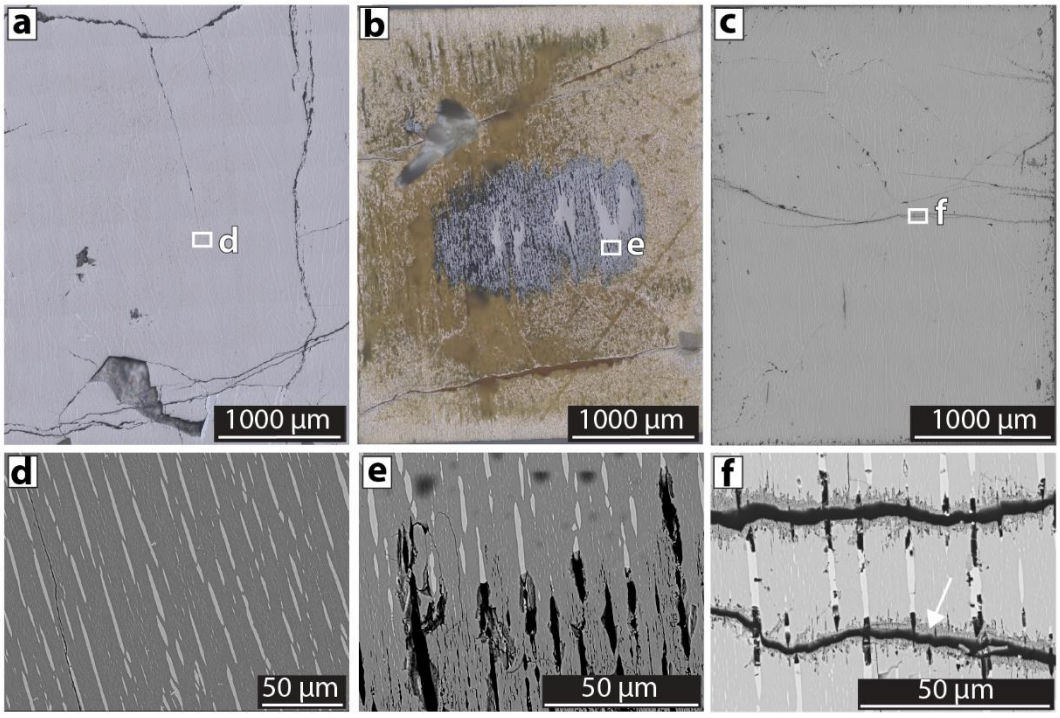

Figure 4.1: Reflected light images of starting material and reacted cubes embedded in resin and exposed to half of its width, perpendicular to its longest side. (a) Unreacted starting material with pre-existing cracks. (b) Reaction in 3 M HCl after 4 days, showing the outermost first zone (yellow) followed by the second (grey with black porosity) and the third zone, ilmenite + hematite (grey without porosity). (c) Reaction product after 31 days in 0.1 M HCl exhibiting dissolution along cracks and the cubes margins. (d) Magnified (BSE) image of the starting material showing hematite exsolution lamellae. (e) Close up (BSE) from (b) of the interface between the third and second zone showing hematite dissolution. (f) Magnified (BSE) image from (c) of the reaction along cracks within the cube exhibiting dissolution of hematite and formation of a replacement product after ilmenite (white arrow).

4.4 Results

The starting material consists of ilmenite with hematite lamellae (Fig. 4.1). The material shows pre-existing cracks within the unreacted parts of the starting material. The orientation of lamellae with respect to the surface was not determined. Hematite lamellae thickness reaches from < 1 µm to ~ 5 µm in cross sections depending on the angle of intersection. Due to the high density of thin hematite lamellae throughout the sample it was not possible to acquire compositional data for ilmenite or hematite free

of contamination by the respective other phase. However, trace elements, such as V and Cr show an affinity to hematite, whereas Mg and Mn are more abundant in ilmenite (Fig. 4.2). Chemical compositions are given in Table 4.1.

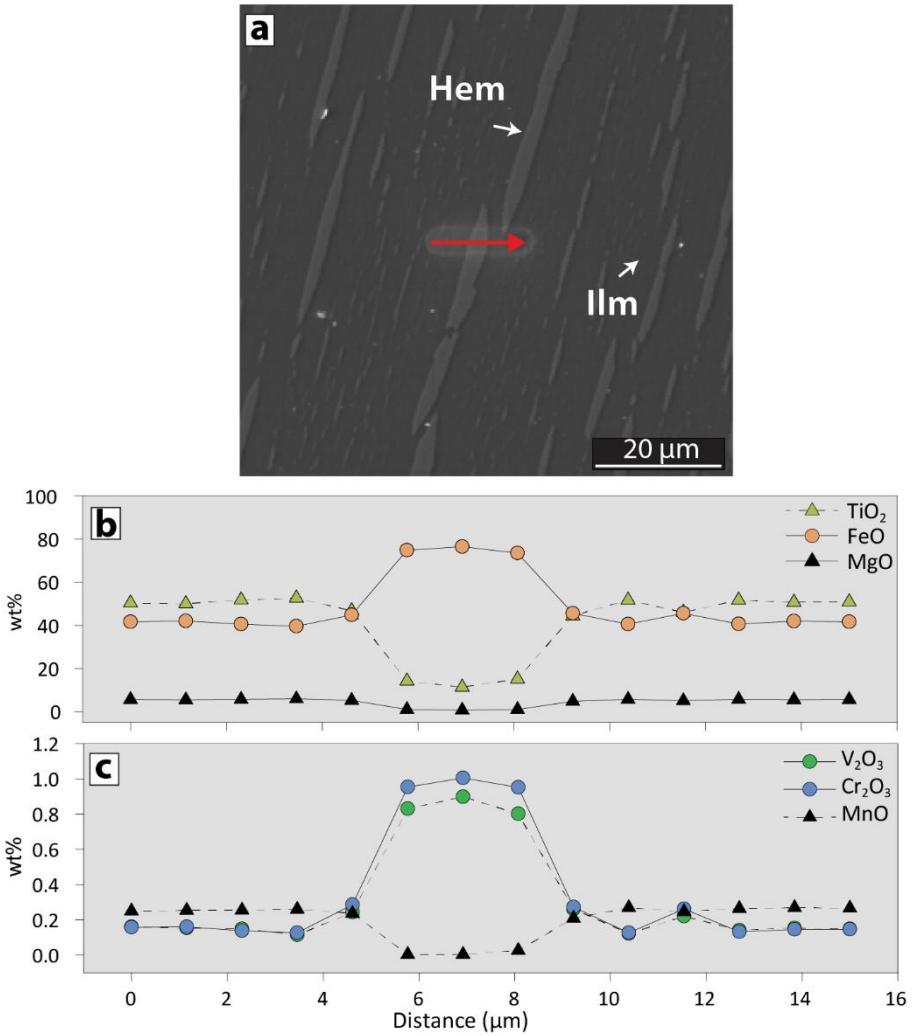

Figure 4.2: (a) BSE image of the unreacted starting material with the location of the analysed profile (red arrow) across hematite exsolution. (b) Major element concentrations along the profile showing low concentrations of TiO_2 and MgO in hematite. (c) Trace elements along the traverse, exhibiting accumulation of V_2O_3 and Cr_2O_3 and depletion of MnO in hematite.

Cubes reacted with 3 M HCl show a significant decrease in weight (45% and 48% at 2 and 4 days respectively). In addition, the colour of cubes changed from grey to yellow-white. However, the difference in reaction extent between the 2 and 4 days experiment is very small, with a relative difference in weight by 3%. Observations of polished cross sections under reflected light microscopy reveal three distinct zones within the cube with sharp contacts but irregular shapes (Fig. 4.1b and 4.3). The first zone is the unreacted material in the centre of the cubes, exhibiting residual ilmenite with hematite lamellae. The second grey zone resembles the original material with hematite being completely dissolved, hence forming porosity. The third outermost zone is porous and of yellow colour and reaches slightly further into the material along the pre-existing cracks within the cubes.

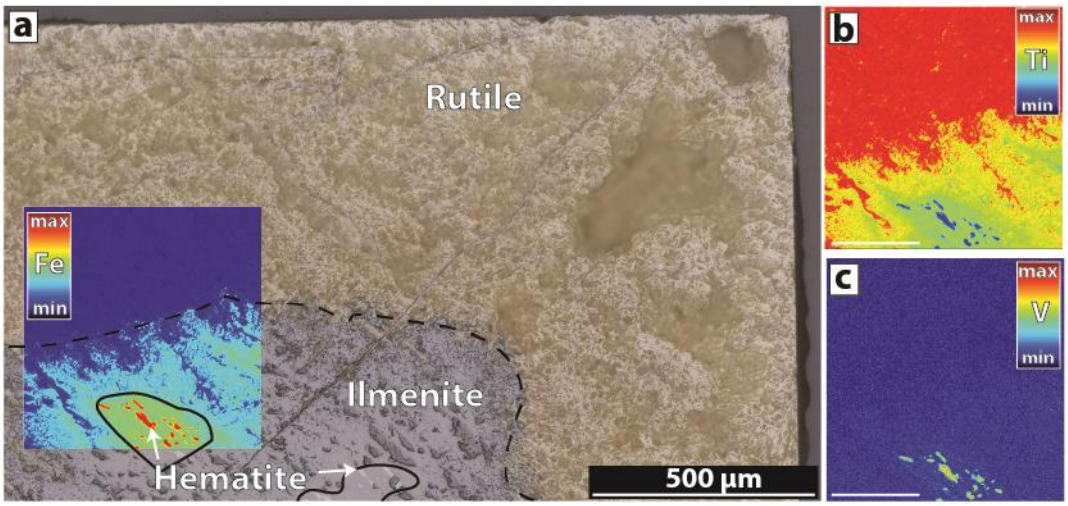

Figure 4.3: (a) Composite of reflected light image with FeO compositional map overlay for the sample reacted in 3 M HCl for 2 days. First zone (rutile) is highlighted by homogeneous depletion of FeO. Transition into the second zone is indicated by dashed line, which shows hematite dissolution. The third zone is highlighted by the solid line, in which hematite is still present. (b) Compositional map for TiO_2 of the same area and magnification, exhibiting higher concentration in the replacement product. (Scale bar is 200 µm) (c) Compositional map for V_2O_3 of the same area and magnification (Scale bar is 200 µm).

Compositional analyses along traverses across the two interfaces between the three zones were acquired, as well as a large scale elemental map (500 x 500 µm) to understand major and trace element behaviour of the replacement reaction (Fig. 4.3 and 4.4). The first profile from the unreacted core to the hematite dissolved zone and avoids large hematite lamellae (Fig 4.4). This profile shows a continuous increase in

TiO_2 from ~52 wt% to 60 wt% and decreasing contents of FeO, MnO, V_2O_3 and Cr_2O_3. The profile over the second interface shows lower average contents of V_2O_3 and Cr_2O_3 compared to the first profile. TiO_2, FeO, MnO and MgO show strong variations in composition across this interface, which is especially pronounced for MgO ranging from 0.35 to 6.70 wt%. These observations are complemented by the large-scale elemental map, which reveals the outermost zone to be homogeneous, TiO_2 rich and FeO depleted (Fig. 4.3a and b). Also the contents of MnO, MgO, V_2O_3 and Cr_2O_3 are greatly reduced compared to the unreacted zone in the centre (Fig. 4.3c). The unreacted zone consists of ilmenite containing minor amounts of MgO and MnO, and hematite identified by high FeO concentrations and higher values of Cr_2O_3 and V_2O_3. Chemical compositions of ilmenite in the innermost zone match those of the unreacted starting material (Table 4.1). The second zone is compositional inhomogeneous and shows a transition from the first to the third zone. The most obvious feature of this zone is the lack of hematite lamellae within the host material.

Table 4.1: Chemical composition of starting materials and replacement products

	SM-Ilmenite		SM-Hematite		3M-HCl-Ilmenite		3M-HCl-Rutile	
n	23		9		12		25	
	Mean	SD	Mean	SD	Mean	SD	Mean	SD
SiO_2 wt%	0.00	0.00	0.01	0.01	0.00	0.00	0.10	0.15
MnO wt%	0.26	0.01	0.01	0.01	0.27	0.01	0.00	0.00
Cr_2O_3 wt%	0.13	0.01	0.96	0.08	0.13	0.01	0.01	0.01
Al_2O_3 wt%	0.03	0.01	0.17	0.03	0.05	0.01	0.04	0.09
FeO wt%	40.13	0.34	74.40	2.25	40.03	0.28	3.35	0.26
TiO_2 wt%	51.84	0.54	14.63	3.21	51.82	0.29	92.08	2.50
MgO wt%	5.72	0.09	0.60	0.28	5.70	0.12	0.07	0.10
V_2O_3 wt%	0.13	0.02	0.85	0.04	0.12	0.02	0.01	0.01
Total	98.24	0.35	91.63	0.84	98.13	0.15	95.66	2.51

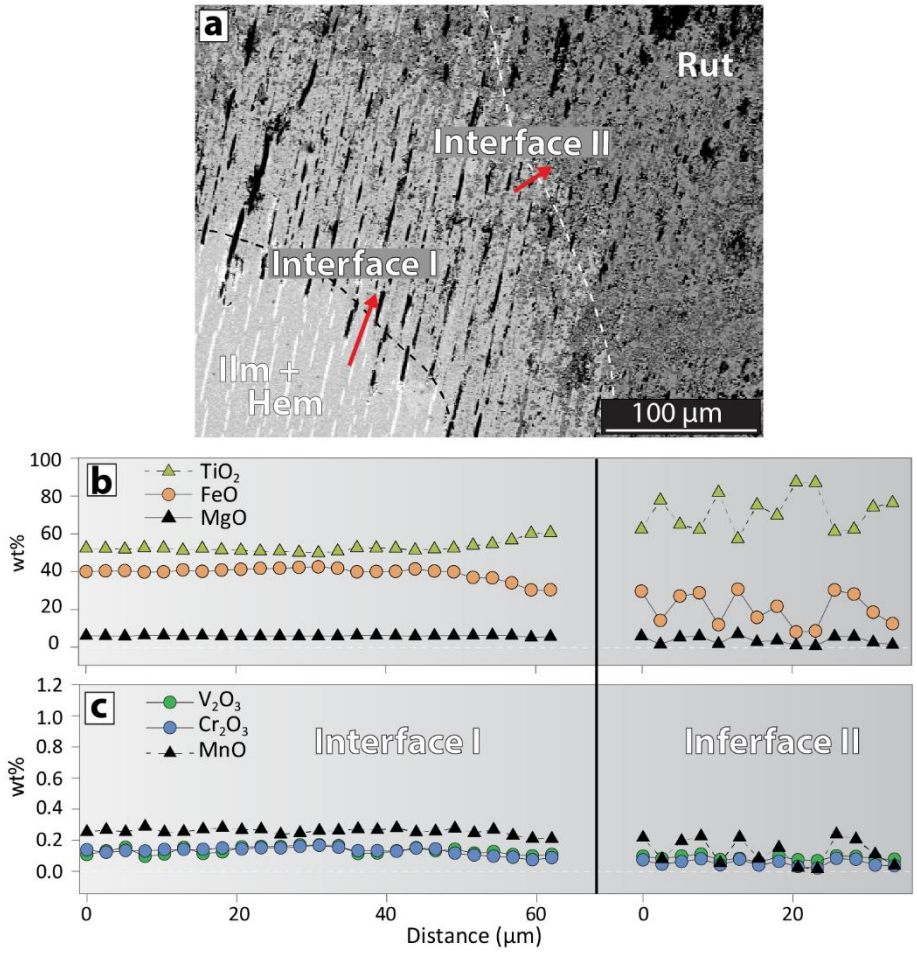

Figure 4.4: (a) BSE-image with location of the compositional profiles (red arrows) for the two interfaces for the sample reacted in 3M HCl for 4 days. (b) Homogeneous profile for major elements at interface I, with slight decrease in FeO and increase in TiO_2 towards the second zone. The profile over the second interface exhibits strong scattering for all elements and a negative correlation between TiO_2 and FeO + MgO. (c) Trace elements along the two to interfaces. Interface I shows homogenous profile whereas interface II is slightly depleted in trace elements and shows strong scattering of data points especially for MnO.

High resolution imaging on cross-sections of the reacted cubes show increased porosity for the outermost zone (Fig. 4.5) and was performed on the sample reacted for 2 days. The surface of this sample was exposed at an angle with respect to hematite lamellae, allowing observations inside the formed porosity formed by dissolution of the former phase. Large cavities of > 10 µm diameter with variable shape develop in the host material (Fig. 4.5b and c). The material is completely replaced by fine needles of varying diameters below ~100 nm, matching the expected habit of rutile crystals also forming twinning as described by Janssen et al. (2010) (Fig. 4.5d). The interface

between the completely replaced outermost zone and the second zone shows a patchy appearance of areas with unreacted ilmenite and areas with secondary rutile (Fig. 4.5b). Former hematite lamellae are completely free of the primary phase, instead small crystals nucleate on the walls of this newly formed porosity (Fig. 4.6).

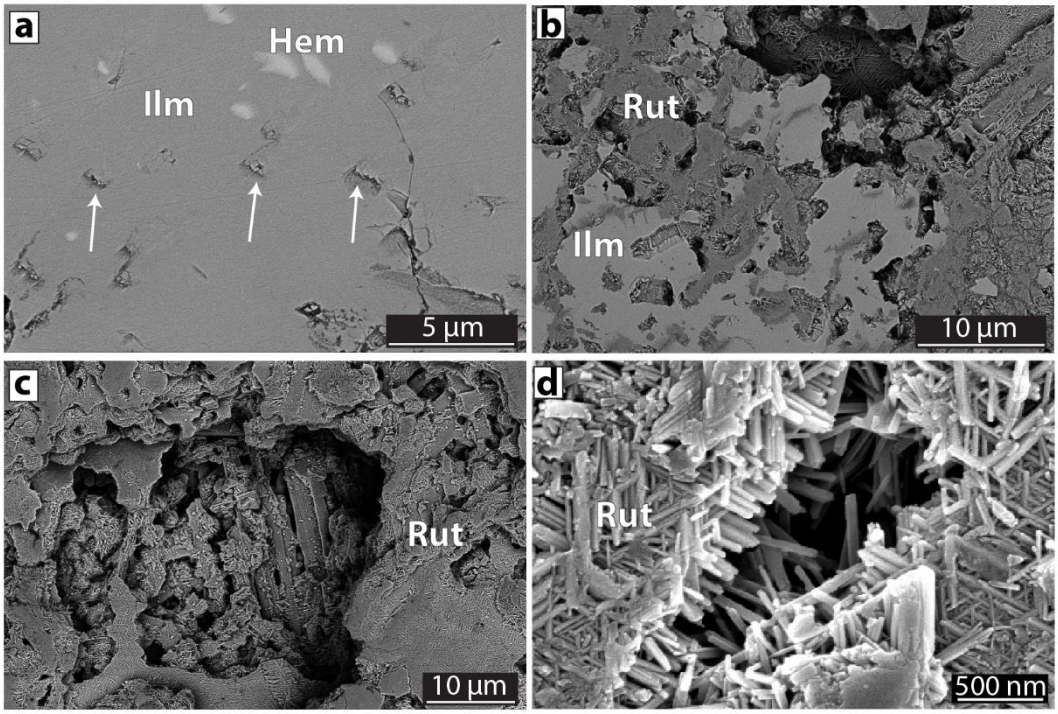

Figure 4.5: High resolution images (BSE + SE) of the sample reacted in 3 M HCl for 2 days. (a) Showing the first interface which exhibits porosity caused by the dissolution of hematite (arrows). (b) Showing interface II with patchy intergrowth of primary ilmenite and secondary rutile. (c) Zone of complete replacement of ilmenite and hematite, note the formation of large porosity. Also the location of former lamellae is indeterminable. (d) SE-image of the replacement product after ilmenite exhibiting fine needles.

The interface between the unreacted core and the hematite dissolved zone was chosen as a target area for FIB tomography to understand the connectivity of the hematite lamellae and the porosity generation at this interface. The sample reacted for 4 days was chosen for this method with lamellae being orientated perpendicularly towards the surface, which allowed for easy tracing of the individual lamellae through the larger volume. The selected area had a width and length of 15 µm at a depth of ~10 µm at a slice size of 30 nm. Due to image processing and cut off, this area was reduced to a width and length of ~ 10 µm. A snapshot of the constructed 3D model is

given in Figure 7. The 3D model shows that individual lamellae reach through the whole of the investigated volume, independent of the individual lamellae size. Dissolution only occurs along hematite lamellae with ilmenite being unaffected, no secondary phase is observed at the site of hematite dissolution and a sharp boundary between hematite and porosity is formed. This is in contrast to observations given above and is likely due to the location of the slice and view directly at the interface towards the unreacted core. Volume analysis give ~14 vol% for the hematite fraction in the investigated volume. Furthermore, thin elongated exsolutions were observed within large hematite lamellae (> 2 µm diameter), this phase is likely to be ilmenite, although no compositional data was obtained for this phase.

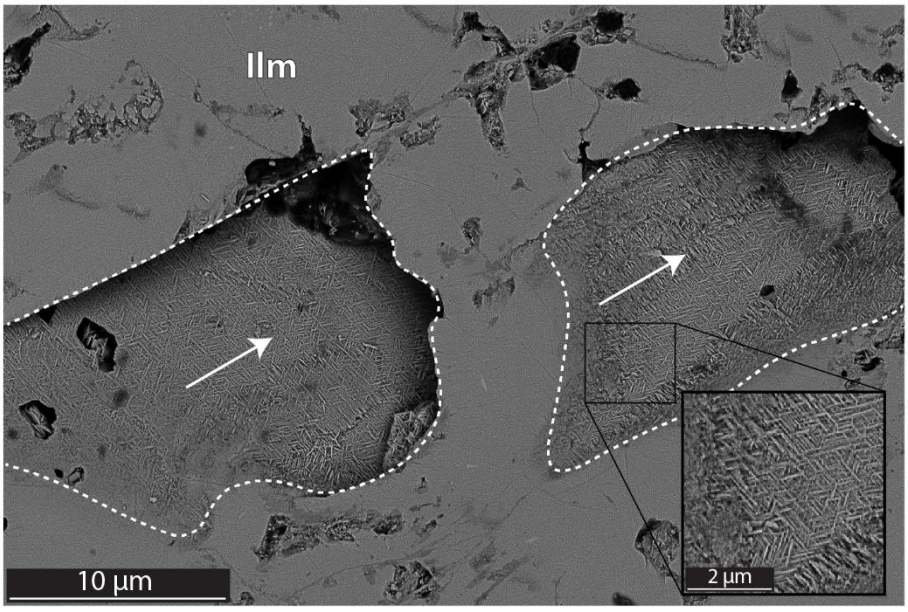

Figure 4.6: BSE image of second zone of sample reacted in 3 M HCl for 2 days. Location of former hematite is indicated by dashed line. Porosity after hematite is dipping into the image plane indicated by arrow, walls towards ilmenite are covered with fine needles of rutile (insert).

The experiment with 0.1 M HCl shows only a small relative difference in weight of 1 % after 31 days without noticeable change in colour on the outside of the cube, opposed to experiments at higher acid concentration. Observations of cross sections show dissolution of hematite lamellae that reach ~100 µm into the sample from the surface of the cube without replacement of ilmenite. Dissolution of hematite is also observed in the centre of the cube where pre-existing cracks allowed fluid access,

which reach about 40 µm into the material. In contrast to the margins of the cube, ilmenite shows replacement by a secondary phase. This replacement is only observed in the vicinity of pre-existing cracks and reaches to the inside of the cube (Fig. 4.1f). The secondary phase after ilmenite is porous and reaches a thickness of maximum ~ 5 µm. Due to its size no attempt was made to analyse this phase by EMPA. However, the analysis shows increased concentrations of TiO_2 and decreasing for FeO as for the reaction product at 3 M HCl.

4.5 Discussion

Ilmenite cubes readily reacted with 3 M HCl solutions in our experiments. The resulting internal texture was the complete replacement of ilmenite by rutile at the outer margins, which was preceded by the selective dissolution of hematite lamellae towards the core of the cubes. FIB tomography revealed connectivity of hematite, even for the smallest lamellae (Fig. 4.7). The dissolution of hematite is thus an effective mechanism to facilitate widespread porosity generation and fluid access inside the sample material, which has also been described for the reaction with sulfuric acid (Chernet, 1999).

The observed porosity generation by selective dissolution is responsible for progressive replacement as has been described for induced fracturing during replacement reactions (Jamtveit et al., 2009; Putnis, 2015). Our observations match those of Janssen et al. (2010), who described the generation of two zones for the reaction of pure ilmenite in 3 M HCl. However, the generation of fractures of ‘fish bone’ texture through the ilmenite was not observed in our experiments. In addition, we observe the formation of a transitional zone which is standing out by the complete dissolution of hematite which appears to react much faster than ilmenite.

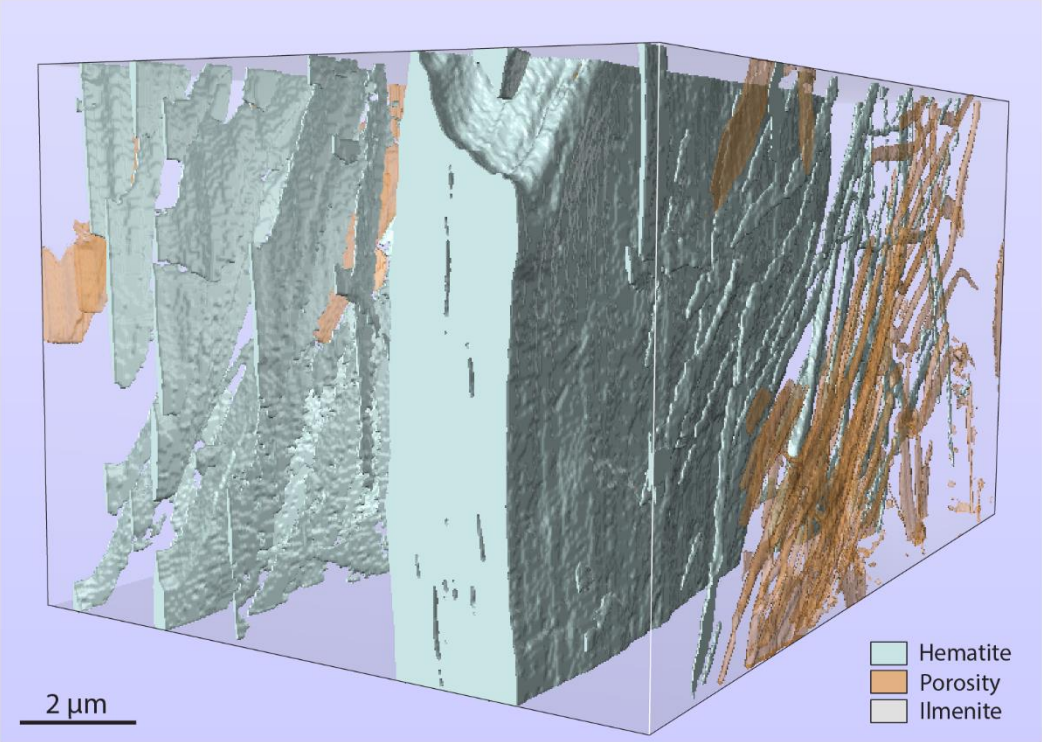

Figure 4.7: Snapshot of the constructed 3D model of the first interface (progressive hematite dissolution), 3 M HCl for 4 days. Individual hematite lamellae are connected throughout the volume independent of their size and are directly connected to porosity via a sharp boundary.

This zone also resembles natural occurring ilmenite grains in mineral sands which are depleted of hematite forming porosity within the grains (e.g. Craig, 2001). The precipitation of secondary rutile is delayed within this second zone, which is likely due to the dissolution of hematite. According to the coupled dissolution reprecipitation mechanism, an interfacial layer of elevated concentration would form at the site of the mineral (hematite – ilmenite) dissolution. Due to the observed fast dissolution of hematite, elemental concentrations of Fe would rise within the interfacial fluid layer and prevent Ti-rich phases from precipitating. The relative rates of mass transport and surface reaction have great influence on precipitated layers in replacement reactions (Ruiz-Agudo et al., 2016; Xia et al., 2007). The porosity generated through this reaction enables exchange of dissolved species (mainly Fe) with the bulk fluid outside of the cube and consequently lowering the concentration of Fe along a profile to the rims of the cube, which results in the onset of secondary

rutile precipitation at a certain Fe concentration. The influence of mass transport from the reaction site and the interfacial fluid is also apparent for the experiment with 0.1 M HCl, as a replacement product is only observed in the inside of the cube following pre-existing cracks that infiltrated by the reacting fluid. It can be expected that mass exchange with the bulk fluid was limited and thus a different fluid composition developed with respect to the bulk fluid, which led to the replacement of ilmenite.

However, it is interesting to note that both mechanisms, the reported reaction induced fracturing in pure ilmenite (Janssen et al., 2010), and hematite lamellae dissolution in our experiments lead to a comparable amount of overall replacement under the same conditions, compared by reaction extent in cross sections for experiments at 3 M HCl. The replacement reaction of ilmenite ending in leucoxene causes a volume decrease of 40% for pure ilmenite (Mücke and Chaudhuri, 1991), this is further increased by the presence of hematite which is completely dissolved. This is also reflected in the strong decrease of sample weight after the experiments (up to 48%). Opposed to the pervasive replacement at higher acid concentrations, experiments with 0.1 M HCl produced minimal dissolution of hematite and replacement of ilmenite which was restricted to the cubes margins and material along pre-existing cracks which allowed fluid access. This observation is in stark difference to reported textures of hierarchical fracture generation which affect large volumes of sample (Janssen et al., 2010) (Fig. 4.8).

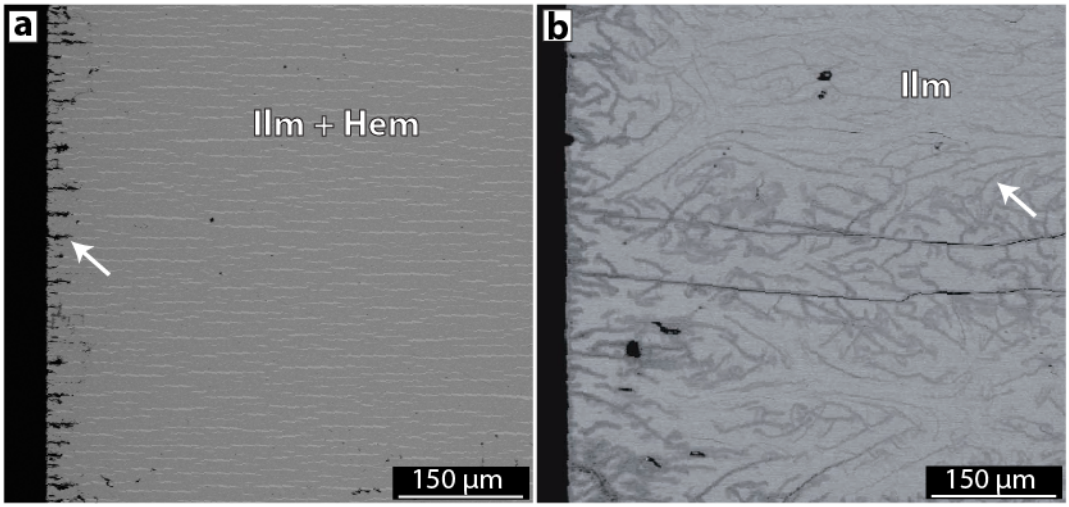

Figure 4.8: (a) BSE cross section of cube reacted in 0.1M HCl for 31 d, exhibiting dissolution (arrow) of hematite (bright grey) starting from the cubes margin. (b) Network of fractures and formation of replacement product (dark grey, arrow) generated by the reaction of pure ilmenite under same conditions as in (a), modified after Janssen et al. (2010).

Element distribution mapping shows secondary rutile to be compositionally homogeneous on the large scale, which is also reflected in low standard deviations of spot analysis, and perfectly match those reported in literature (Janssen et al., 2010). The compositional profile of the first interface from the unreacted core to the hematite dissolved zone exhibits an increase of TiO_2 and decrease of FeO, as expected for the selective dissolution of hematite (Fig. 4.4b). The second interface into the secondary rutile shows strong compositional variation and a negative correlation between TiO_2 and FeO, MgO and MnO. This is due to the incipient patchy formation of rutile (Fig. 4.5b), which is free of MnO and only contains minor amounts of MgO and FeO. This replacement appears to be initiated at the walls of the former hematite lamellae and completely overprints holes (porosity) formed by hematite dissolution. The location of previous hematite lamellae is indeterminable within the porous rutile zone (Fig. 4.5c and 4.6). Along with the dissolution of hematite, elemental concentrations of V_2O_3 and Cr_2O_3 are greatly reduced, as these elements are primarily hosted in hematite (Fig. 4.3c and 4.4c). Elemental concentrations of MnO and MgO hosted in the primary ilmenite show a strong decrease in the secondary rutile. Furthermore, contents of

Al_2O_3 do show no distinguishable compositional change between parent mineral and replacement product, whereas SiO_2 is slightly elevated in the latter. This is in good agreement with reported compositions of natural samples that show depletion in MgO, MnO and accumulation of Al_2O_3 and SiO_2 within the secondary product during alteration at surface conditions (Frost et al., 1983; Pownceby, 2010). In contrast, Cr_2O_3 contents do not increase in our secondary rutile.

4.6 Conclusion

This study provides new insight into the replacement mechanism of ilmenite with hematite exsolution lamellae, commonly observed in natural rocks. The reactions in acidic solutions form the same replacement product as the reaction of pure ilmenite. However, the resulting texture differs greatly between the different starting materials. Janssen et al. (2010) reported a fracture network on the scale of hundreds of µm, whereas our experiments show that only ~100 µm of the material are affected by the reaction, which is due to hematite dissolution rather than replacement. This means, that the presence of hematite lamellae can potentially influence properties of the rock, such as permeability, as it prevents the host rock from fracturing. Furthermore, for mineral processing, the presence of hematite prevents fracture generation and might negatively impact the overall replacement kinetics of ilmenite by rutile in addition to the increased amount of Fe present in the system that has to be dissolved.

At high acid concentrations shows porosity generation through the fast dissolution of connected hematite lamellae. This aids the reaction, as it provides fluid access throughout the sample. In addition, impurity element hosted by hematite such as V and Cr are efficiently removed by its dissolution.

4.7 References

Angiboust, S., Harlov, D., 2017. Ilmenite breakdown and rutile-titanite stability in metagranitoids: Natural observations and experimental results. American Mineralogist, 102(8): 1696-1708.

Bruckard, W.J., Pownceby, M.I., Smith, L.K., Sparrow, G.J., 2015. Review of processing conditions for Murray Basin ilmenite concentrates. Mineral Processing and Extractive Metallurgy, 124(1): 47-63.

Charlier, B., Duchesne, J.-C., Vander Auwera, J., 2006. Magma chamber processes in the Tellnes ilmenite deposit (Rogaland Anorthosite Province, SW Norway) and the formation of Fe–Ti ores in massif-type anorthosites. Chemical Geology, 234(3-4): 264-290.

Charlier, B., Skår, Ø., Korneliussen, A., Duchesne, J.-C., Vander Auwera, J., 2007. Ilmenite composition in the Tellnes Fe–Ti deposit, SW Norway: fractional crystallization, postcumulus evolution and ilmenite–zircon relation. Contributions to Mineralogy and Petrology, 154(2): 119-134.

Chernet, T., 1999. Effect of mineralogy and texture in the TiO 2 pigment production process of the Tellnes ilmenite concentrate. Mineralogy and petrology, 67(1-2): 21-32.

Craig, J.R., 2001. Ore-mineral textures and the tales they tell. The Canadian Mineralogist, 39(4): 937-956.

Darby, D.A., 1984. Trace elements in ilmenite: a way to discriminate provenance or age in coastal sands. Geological Society of America Bulletin, 95(10): 1208-1218.

El-Hazek, N., Lasheen, T., El-Sheikh, R., Zaki, S.A., 2007. Hydrometallurgical criteria for TiO_2 leaching from Rosetta ilmenite by hydrochloric acid. Hydrometallurgy, 87(1-2): 45-50.

Frost, M., Grey, I., Harrowfield, I., Mason, K., 1983. The dependence of alumina and silica contents on the extent of alteration of weathered ilmenites from Western Australia. Mineralogical Magazine, 47(343): 201-208.

Gázquez, M.J., Bolívar, J.P., Garcia-Tenorio, R., Vaca, F., 2014. A review of the production cycle of titanium dioxide pigment. Materials Sciences and Applications, 5(07): 441.

Grey, I., Li, C., 2003. Hydroxylian pseudorutile derived from picroilmenite in the Murray Basin, southeastern Australia. De Gruyter.

Grey, I., MacRae, C., Silvester, E., Susini, J., 2005. Behaviour of impurity elements during the weathering of ilmenite. Mineralogical Magazine, 69(4): 437-446.

Grey, I.E., Reid, A.F., 1975. The structure of pseudorutile and its role in the natural alteration of ilmenite. American Mineralogist: Journal of Earth and Planetary Materials, 60(9-10): 898-906.

Gueguin, M., Cardarelli, F., 2007. Chemistry and mineralogy of titania-rich slags. Part 1—hemo-ilmenite, sulphate, and upgraded titania slags. Mineral Processing and Extractive Metallurgy Review, 28(1): 1-58.

Habashi, F., Kamaleddine, F., Bourricaudy, E., 2014. A New Process to upgrade ilmenite to synthetic rutile, Conference of Metallurgists Proceedings (COM 2014).

Itoh, S., Sato, S., Ono, J., Okada, H., Nagasaka, T., 2006. Feasibility study of the new rutile extraction process from natural ilmenite ore based on the oxidation reaction. Metallurgical and Materials Transactions B, 37(6): 979-985.

Jamtveit, B., Putnis, C.V., Malthe-Sørenssen, A., 2009. Reaction induced fracturing during replacement processes. Contributions to Mineralogy and Petrology, 157(1): 127-133.

Janssen, A., Putnis, A., 2011. Processes of oxidation and HCl-leaching of Tellnes ilmenite. Hydrometallurgy, 109(3-4): 194-201.

Janssen, A., Putnis, A., Geisler, T., Putnis, C., 2010. The experimental replacement of ilmenite by rutile in HCl solutions. Mineralogical Magazine, 74(4): 633-644.

Jena, B., Dresler, W., Reilly, I., 1995. Extraction of titanium, vanadium and iron from titanomagnetite deposits at pipestone lake, Manitoba, Canada. Minerals engineering, 8(1-2): 159-168.

Kletetschka, G., Wasilewski, P.J., Taylor, P.T., 2002. The role of hematite–ilmenite solid solution in the production of magnetic anomalies in ground-and satellite-based data. Tectonophysics, 347(1-3): 167-177.

Mackey, T.S., 1994. Upgrading ilmenite into a high-grade synthetic rutile. Jom, 46(4): 59-64.

Mahmoud, M., Afifi, A., Ibrahim, I., 2004. Reductive leaching of ilmenite ore in hydrochloric acid for preparation of synthetic rutile. Hydrometallurgy, 73(1-2): 99-109.

McEnroe, S., Harrison, R., Robinson, P., Langenhorst, F., 2002. Nanoscale haematite–ilmenite lamellae in massive ilmenite rock: an example of 'lamellar magnetism'with implications for planetary magnetic anomalies. Geophysical Journal International, 151(3): 890-912.

McEnroe, S.A., Robinson, P., Langenhorst, F., Frandsen, C., Terry, M.P. and Boffa Ballaran, T. 2007. Magnetization of exsolution intergrowths of hematite and ilmenite: Mineral chemistry, phase relations, and magnetic properties of hemo-ilmenite ores with micron-to nanometer-scale lamellae from Allard Lake, Quebec. Journal of Geophysical Research: Solid Earth 112.

Mücke, A., Chaudhuri, J.B., 1991. The continuous alteration of ilmenite through pseudorutile to leucoxene. Ore geology reviews, 6(1): 25-44.

Nguyen, T.H., Lee, M.S., 2019. A review on the recovery of titanium dioxide from Ilmenite ores by direct leaching technologies. Mineral Processing and Extractive Metallurgy Review, 40(4): 231-247.

Olanipekun, E., 1999. A kinetic study of the leaching of a Nigerian ilmenite ore by hydrochloric acid. Hydrometallurgy, 53(1): 1-10.

Ping, T., Hu, H.-P., Zhang, L., 2011. Effects of mechanical activation and oxidation-reduction on hydrochloric acid leaching of Panxi ilmenite concentration. Transactions of Nonferrous Metals Society of China, 21(6): 1414-1421.

Plümper, O., Røyne, A., Magrasó, A., Jamtveit, B., 2012. The interface-scale mechanism of reaction-induced fracturing during serpentinization. Geology, 40(12): 1103-1106.

Pochon, A., Beaudoin, G., Branquet, Y., Boulvais, P., Gloaguen, E. and Gapais, D. 2017. Metal mobility during hydrothermal breakdown of Fe-Ti oxides: insights from Sb-Au mineralizing event (Variscan Armorican Massif, France). Ore Geology Reviews 91, 66-99.

Pownceby, M., 2010. Alteration and associated impurity element enrichment in detrital ilmenites from the Murray Basin, southeast Australia: a product of multistage alteration. Australian Journal of Earth Sciences, 57(2): 243-258.

Putnis, A., 2009. Mineral replacement reactions. Reviews in mineralogy and geochemistry, 70(1): 87-124.

Putnis, A., 2015. Transient porosity resulting from fluid–mineral interaction and its consequences. Reviews in Mineralogy and Geochemistry, 80(1): 1-23.

Putnis, C.V., Geisler, T., Schmid-Beurmann, P., Stephan, T., Giampaolo, C., 2007. An experimental study of the replacement of leucite by analcime. American Mineralogist, 92(1): 19-26.

Ruiz-Agudo, E., King, H.E., Patiño-López, L.D., Putnis, C.V., Geisler, T., Rodriguez-Navarro, C. and Putnis, A. 2016. Control of silicate weathering by interface-coupled dissolution-precipitation processes at the mineral-solution interface. Geology 44, 567-570.

Schroeder, P.A., Le Golvan, J.J., Roden, M.F., 2002. Weathering of ilmenite from granite and chlorite schist in the Georgia Piedmont. American Mineralogist, 87(11-12): 1616-1625.

Stanaway, K., 1994. Overview of titanium dioxide feedstocks. Mining engineering, 46(12): 1367-1370.

Temple, A.K., 1966. Alteration of ilmenite. Economic Geology, 61(4): 695-714.

Van Dyk, J.P., Vegter, N.M., Pistorius, P.C., 2002. Kinetics of ilmenite dissolution in hydrochloric acid. Hydrometallurgy, 65(1): 31-36.

Xia, F., Zhou, J., Pring, A., Ngothai, Y., O'Neill, B., Brugger, J., Chen, G. and Colby, C. 2007. The role of pyrrhotite (Fe 7 S 8) and the sample texture in the hydrothermal transformation of pentlandite ((Fe, Ni) 9 S 8) to violarite ((Ni, Fe) 3 S 4). Reaction Kinetics and Catalysis Letters 92, 257-266.

Zhang, L., Hu, H., Wei, L., Chen, Q., Tan, J., 2010. Hydrochloric acid leaching behaviour of mechanically activated Panxi ilmenite (FeTiO3). Separation and Purification Technology, 73(2): 173-178.

Zhang, L., Li, G.-Q., Zhang, W., 2011. Synthesis of rutile from high titania slag by pyrometallurgical route. Transactions of Nonferrous Metals Society of China, 21(10): 2317-2322.

Every reasonable effort has been made to acknowledge the owners of copyright material. I would be pleased to hear from any copyright owner who has been omitted or incorrectly acknowledged.

Chapter 5

Thesis Conclusion

5.1 Thesis Conclusion

This PhD research presents new insight into the prevailing mechanisms during fluid rock interactions. Hydrothermal experiments were conducted on different mineral systems, which results are significant for both natural systems and mineral processing. Chemical and textural information was obtained by using various methods, such as FESEM, EDS, EMPA, FIB-tomography, TGA, Raman spectroscopy and ICP-MS.

The experimental alteration of olivine rich mineral assemblages shows the effect of fluid composition and presence of additional enstatite on the evolving serpentine morphology. With increasing fluid salinity, the serpentine morphology evolves from fine-grained proto–serpentine, polyhedral serpentine and lizardite, to lizardite and chrysotile fibres, to serpentine tubes, cones and fibres. This observation permits a qualitative link between the reacting fluid composition and the morphology of precipitating secondary serpentine. The occurrence of polyhedral serpentine is restricted to alteration in non–saline solution in a narrow compositional span of the solid phases, which may reflect its relatively rare occurrence in natural alteration systems. The increase in serpentinisation rate with fluid salinity in our experiments is linked to the concurrent dissolution of enstatite, which dissolution is increased in saline solutions. This highlights the importance of the interplay between different minerals reacting with a fluid phase at the same time. The delamination of serpentine reaction rims in high saline experiments indicates a further increase in reaction rate as it creates new surface area exposed to the fluid phase and may indicate that serpentine precipitation at high salinity is spatially decoupled from olivine/enstatite dissolution, whereas serpentinisation at lower salinity may proceed as an interface-coupled replacement reaction.

It was shown that a primary nickel ore can be upgraded to high Ni tenor ore during concurrent serpentinisation of ultramafic rock within laboratory time scales. For assemblages containing Pn-Po-Py, the replacement proceeds rapidly through the

dissolution and replacement of the primary pyrrhotite by magnetite. This is accompanied by the replacement of pentlandite by millerite, in O_2-containing experiments, or heazlewoodite, in O_2-free experiments, at low sulphide/silicate ratios ≤ 20 wt%, whereas experiments with >40 wt% sulphides do not show the formation of millerite or heazlewoodite. The change of bulk sulphide compositions to pentlandite favours the formation of both millerite and heazlewoodite within the same experiment at 20 wt% sulphides. Experiments for pure sulphide Pn-Po-Py assemblages form exsolutions of Mss within pentlandite, in contrast to pure pentlandite, which doesn't change in composition. In addition to the observed assemblages, textural replacement features resemble those found in natural deposits. These observations highlight the complex control of this replacement reaction, which is depending on bulk sulphide composition, sulphide/silicate and O_2 content.

Hydrothermal experiments on the alteration of ilmenite with hematite lamellae provide new insight into the replacement reaction of ilmenite by rutile. Whereas the replacement product of ilmenite is the same as the replacement product produced in the absence of hematite. However, concurrently reacting hematite lamellae led to a great change in observed textures within cubes, in acidic solutions. The development of a hierarchical network of fractures is not observed in cubes containing hematite lamellae. This is in contrast to reported observations from literature, which has potential influence on the physical properties of the rock, such as permeability. Furthermore, concurrently dissolving hematite lamellae led to the formation of connected porosity reaching into the ilmenite host. In addition, impurity elements hosted by hematite, such as Cr and V, are greatly reduced through its dissolution.

All of the above investigated relations in the investigated mineral systems show the complex interactions occurring during fluid rock interactions. This work revealed important leads into the reaction of composite mineral systems reacting in a fluid phase. It appears that especially the spatial distribution of mineral phases have important consequences on the reaction pathways of the system. For example, small concentration of Si released by enstatite dissolution suppresses brucite formation and

increases the reaction kinetics of olivine serpentinisation. Also, the alteration of sulphides is greatly affected by the presence of ultramafic rock and concurrently dissolving hematite in ilmenite affects the final alteration texture. These examples highlight the complex interplay in mineral alteration reactions.

5.2 Future work

It is apparent that a wide range of variables play into the evolution of these experimental multicomponent systems, such as grain size, temperature, pressure, fluid composition. Therefore, different factors have to be carefully controlled in order to investigate their effect on others. For instance, serpentinisation experiments in Chapter 2 and 3 were all conducted at identical temperature and pressure conditions (vapour pressure). This offers great opportunity to extend this work into different P-T conditions, e.g. into the stability field of antigorite. Furthermore, the evolution of serpentine morphology is controlled by both the composition of the fluid and solid phase. Although not investigated in detail, the morphologies of serpentine in experiments with coexisting sulphides show a very distinct morphology of chrysotile and even the formation of brucite, not observed in most experiments in Chapter 2, highlighting the effect of the fluid composition and bulk composition. Although it was not possible to determine the effect of fluid rock ratio on the morphology, we would expect this to have an effect on the morphology, especially at very low fluid/rock ratios, as the activity of water is reduced. Lastly, the investigation of serpentine polymorphs by TEM grown in controlled environments might hold clues about their growth mechanism, e.g. potential incorporation of impurity elements.

Bibliography

Altree-Williams, A., Pring, A., Ngothai, Y. and Brugger, J. 2015. Textural and compositional complexities resulting from coupled dissolution–reprecipitation reactions in geomaterials. Earth-Science Reviews 150, 628-651.

Allen, D.E., Seyfried Jr, W., 2003. Compositional controls on vent fluids from ultramafic-hosted hydrothermal systems at mid-ocean ridges: An experimental study at 400 C, 500 bars. Geochim. Cosmochim. Acta , 67(8): 1531-1542.

Anders, H. 2012. Experimental investigations of interactions between saltwater and ultramafic rocks in hydrothermal systems. Doctoral dissertation, Bremen University.

Andreani, M., Mével, C., Boullier, A.M., Escartin, J., 2007. Dynamic control on serpentine crystallization in veins: Constraints on hydration processes in oceanic peridotites. Geochemistry, Geophysics, Geosystems, 8(2).

Andreani, M., Grauby, O., Baronnet, A., Muñoz, M., 2008. Occurrence, composition and growth of polyhedral serpentine. European Journal of Mineralogy, 20(2): 159-171.

Andreani, M., Daniel, I., Pollet-Villard, M., 2013a. Aluminum speeds up the hydrothermal alteration of olivine. Am. Mineral., 98(10): 1738-1744.

Andreani, M., Munoz, M., Marcaillou, C., Delacour, A., 2013b. μXANES study of iron redox state in serpentine during oceanic serpentinization. Lithos, 178: 70-83.

Angiboust, S. and Harlov, D. 2017. Ilmenite breakdown and rutile-titanite stability in metagranitoids: Natural observations and experimental results. American Mineralogist 102, 1696-1708.

Bach, W., Paulick, H., Garrido, C.J., Ildefonse, B., Meurer, W.P. and Humphris, S.E. 2006. Unraveling the sequence of serpentinization reactions: petrography, mineral chemistry, and petrophysics of serpentinites from MAR 15 N (ODP Leg 209, Site 1274). Geophysical research letters 33.

Bach, W., Garrido, C.J., Paulick, H., Harvey, J., Rosner, M., 2004. Seawater-peridotite interactions: First insights from ODP Leg 209, MAR 15 N. Geochemistry, Geophysics, Geosystems, 5(9).

Baronnet, A., Andréani, M., Grauby, O., Devouard, B., Nitsche, S. and Chaudanson, D. 2007. Onion morphology and microstructure of polyhedral serpentine. American Mineralogist 92, 687-690.

Baronnet, A. and Devouard, B. 1996. Topology and crystal growth of natural chrysotile and polygonal serpentine. Journal of Crystal Growth 166, 952-960.

Barnes, S. J. and Hill, R. E. 2000. Metamorphism of komatiite-hosted nickel sulfide deposits.

Barnes, S. J., Wells, M. A. and Verrall, M. R. 2009. Effects of magmatic processes, serpentinization, and talc-carbonate alteration on sulfide mineralogy and ore textures in the Black Swan disseminated nickel sulfide deposit, Yilgarn Craton. Economic Geology, 104(4), 539-562.

Beard, J.S. and Frost, B.R. 2017. The stoichiometric effects of ferric iron substitutions in serpentine from microprobe data. International Geology Review 59, 541-547.

Beard, J.S., Frost, B.R., Fryer, P., McCaig, A., Searle, R., Ildefonse, B., Zinin, P. and Sharma, S.K. 2009. Onset and progression of serpentinization and magnetite formation in olivine-rich troctolite from IODP Hole U1309D. Journal of Petrology 50, 387-403.

Beinlich, A., von Heydebrand, A., Klemd, R., Martin, L., Hicks, J.. Compositional variations in chromite, pentlandite, chalcopyrite and bulk rock PGE in massive chromitite due to metamorphism of the Panton Intrusion, east Kimberley, Western Australia. In revision for Ore Geology Reviews.

Beinlich, A., Austrheim, H., Mavromatis, V., Grguric, B., Putnis, C. V. and Putnis, A. 2018. Peridotite weathering is the missing ingredient of Earth's continental crust composition. Nat. Commun., 9(1): 634.

Beinlich, A., Plümper, O., Hövelmann, J., Austrheim, H., Jamtveit, B., 2012. Massive serpentinite carbonation at Linnajavri, N–Norway. Terra Nova, 24(6): 446-455.

Beinlich, A., Austrheim, H., Glodny, J., Erambert, M., Andersen, T.B., 2010. CO_2 sequestration and extreme Mg depletion in serpentinized peridotite clasts from the Devonian Solund basin, SW-Norway. Geochim. Cosmochim. Acta , 74(24): 6935-6964.

Belzile, N., Chen, Y.-W., Cai, M.-F. and Li, Y. 2004. A review on pyrrhotite oxidation. Journal of Geochemical Exploration, 84(2), 65-76.

Brenan, J. M. 2003. Effects of fO_2, fS_2, temperature, and melt composition on Fe-Ni exchange between olivine and sulfide liquid: implications for natural olivine–sulfide assemblages. Geochimica et Cosmochimica Acta, 67(14), 2663-2681.

Bruckard, W.J., Pownceby, M.I., Smith, L.K. and Sparrow, G.J. 2015. Review of processing conditions for Murray Basin ilmenite concentrates. Mineral Processing and Extractive Metallurgy 124, 47-63.

Butt, C. and Brand, N. 2005. Mt. Keith nickel sulphide deposit, Western Australia. Regolith Expression of Australian Ore Systems, 112-114.

Butt, C. and Nickel, E. 1981. Mineralogy and geochemistry of the weathering of the disseminated nickel sulfide deposit at Mt. Keith, Western Australia. Economic Geology 76, 1736-1751.

Charlier, B., Duchesne, J.-C. and Vander Auwera, J. 2006. Magma chamber processes in the Tellnes ilmenite deposit (Rogaland Anorthosite Province, SW Norway) and the formation of Fe–Ti ores in massif-type anorthosites. Chemical Geology 234, 264-290.

Charlier, B., Skår, Ø., Korneliussen, A., Duchesne, J.-C. and Vander Auwera, J. 2007. Ilmenite composition in the Tellnes Fe–Ti deposit, SW Norway: fractional crystallization, postcumulus evolution and ilmenite–zircon relation. Contributions to Mineralogy and Petrology 154, 119-134.

Chavagnac, V., Monnin, C., Ceuleneer, G., Boulart, C. and Hoareau, G. 2013. Characterization of hyperalkaline fluids produced by low-temperature serpentinization of mantle peridotites in the Oman and Ligurian ophiolites. Geochemistry, Geophysics, Geosystems, 14(7), 2496-2522.

Chernet, T. 1999. Effect of mineralogy and texture in the TiO_2 pigment production process of the Tellnes ilmenite concentrate. Mineralogy and petrology 67, 21-32.

Clark, T. and Naldrett, A. 1972. The distribution of Fe and Ni between synthetic olivine and sulfide at 900 degrees C. Economic Geology, 67(7), 939-952.

Craig, J. R. 1973. Pyrite-pentlandite assemblages and other low temperature relations in the Fe-Ni-S system. American Journal of Science, 273(A), 496-510.

Craig, J.R. 2001. Ore-mineral textures and the tales they tell. The Canadian Mineralogist 39, 937-956.

Colás, V., Padrón-Navarta, J.A., González-Jiménez, J.M., Fanlo, I., Sánchez-Vizcaíno, V.L., Gervilla, F. and Castroviejo, R. 2017. The role of silica in the hydrous metamorphism of chromite. Ore Geology Reviews 90, 274-286.

Cole, D.R., Larson, P.B., Riciputi, L.R. and Mora, C.I. 2004. Oxygen isotope zoning profiles in hydrothermally altered feldspars: Estimating the duration of water-rock interaction. Geology 32, 29-32.

Darby, D.A. 1984. Trace elements in ilmenite: a way to discriminate provenance or age in coastal sands. Geological Society of America Bulletin 95, 1208-1218.

De Ruiter, L. and Austrheim, H. 2018. Formation of magnesium silicate hydrate cement in nature. Journal of the Geological Society 175, 308-320.

De Ruiter, L., Putnis, C.V., Hövelmann, J.r., King, H.E. and Austrheim, H. 2019. Direct observations of the coupling between quartz dissolution and Mg-silicate formation. ACS Earth and Space Chemistry 3, 617-625.

Donaldson, M. 1981. Redistribution of ore elements during serpentinization and talc-carbonate alteration of some Archean dunites, Western Australia. Economic Geology, 76(6), 1698-1713.

Dunn, R.A., Arai, R., Eason, D.E., Canales, J.P. and Sohn, R.A. 2017. Three-Dimensional Seismic Structure of the Mid-Atlantic Ridge: An Investigation of Tectonic, Magmatic, and Hydrothermal Processes in the Rainbow Area. Journal of Geophysical Research: Solid Earth 122, 9580-9602.

Eckstrand, O. 1975. The Dumont serpentinite; a model for control of nickeliferous opaque mineral assemblages by alteration reactions in ultramafic rocks. Economic Geology, 70(1), 183-201.

El-Hazek, N., Lasheen, T., El-Sheikh, R. and Zaki, S.A. 2007. Hydrometallurgical criteria for TiO_2 leaching from Rosetta ilmenite by hydrochloric acid. Hydrometallurgy 87, 45-50.

Emmanuel, S., Ague, J.J. and Walderhaug, O. 2010. Interfacial energy effects and the evolution of pore size distributions during quartz precipitation in sandstone. Geochimica et Cosmochimica Acta 74, 3539-3552.

Evans, B. W. 2010. Lizardite versus antigorite serpentinite: Magnetite, hydrogen, and life (?). Geology, 38(10), 879-882.

Evans, B.W., 2004. The serpentinite multisystem revisited: chrysotile is metastable. International Geology Review, 46(6): 479-506.

Evans, B.W., 2008. Control of the products of serpentinization by the Fe2+ Mg− 1 exchange potential of olivine and orthopyroxene. Journal of Petrology, 49(10): 1873-1887.

Evans, K., Powell, R. and Frost, B. 2013. Using equilibrium thermodynamics in the study of metasomatic alteration, illustrated by an application to serpentinites. Lithos 168, 67-84.

Farough, A., Moore, D.E., Lockner, D.A. and Lowell, R. 2016. Evolution of fracture permeability of ultramafic rocks undergoing serpentinization at hydrothermal conditions: An experimental study. Geochemistry, Geophysics, Geosystems 17, 44-55.

Filippidis, A. 1982. Experimental study of the serpentinization of Mg-Fe-Ni olivine in the presence of sulfur. The Canadian Mineralogist, 20(4), 567-574.

Filippidis, A. 1985. Formation of awaruite in the system Ni-Fe-Mg-Si-OHS and olivine hydration with NaOH solution, an experimental study. Economic Geology, 80(7), 1974-1980.

Fleet, M. and MacRae, N. 1983. Partition of Ni between olivine and sulfide and its application to Ni-Cu sulfide deposits. Contributions to Mineralogy and Petrology, 83(1-2), 75-81.

Fleet, M. and MacRae, N. 1987. Partition of Ni between olivine and sulfide: the effect of temperature. Contributions to Mineralogy and Petrology, 95(3), 336-342.

Fleet, M. and MacRae, N. 1988. Partition of Ni between olivine and sulfide: equilibria with sulfide-oxide liquids. Contributions to Mineralogy and Petrology, 100(4), 462-469.

Fleet, M., MacRae, N. and Herzberg, C. 1977. Partition of nickel between olivine and sulfide: A test for immiscible sulfide liquids. Contributions to Mineralogy and Petrology, 65(2), 191-197.

Frost, B.R., Evans, K.A., Swapp, S.M., Beard, J.S. and Mothersole, F.E. 2013. The process of serpentinization in dunite from New Caledonia. Lithos 178, 24-39.

Frost, B. R. and Beard, J. S. 2007. On silica activity and serpentinization. Journal of Petrology, 48(7), 1351-1368.

Frost, M., Grey, I., Harrowfield, I. and Mason, K. 1983. The dependence of alumina and silica contents on the extent of alteration of weathered ilmenites from Western Australia. Mineralogical Magazine 47, 201-208.

Gázquez, M.J., Bolívar, J.P., Garcia-Tenorio, R. and Vaca, F. 2014. A review of the production cycle of titanium dioxide pigment. Materials Sciences and Applications 5, 441.

Geisler, T., Dohmen, L., Lenting, C. and Fritzsche, M.B. 2019. Real-time in situ observations of reaction and transport phenomena during silicate glass corrosion by fluid-cell Raman spectroscopy. Nature materials, 1.

Gole, M. J. 2014. Leaching of S, Cu, and Fe from disseminated Ni-(Fe)-(Cu) sulphide ore during serpentinization of dunite host rocks at Mount Keith, Agnew-Wiluna Belt, Western Australia. Mineralium Deposita, 49(7), 821-842.

Gole, M. 2008. Metasomatic interaction between disseminated nickel sulphides and reduced metamorphic fluids, Honeymoon Well komatiite complex, Western Australia. Applied Earth Science, 117(3), 112-124.

Grguric, B. A., Seat, Z., Karpuzov, A. A. and Simonov, O. N. 2013. The West Jordan deposit, a newly-discovered type 2 dunite-hosted nickel sulphide system in the northern Agnew–Wiluna belt, Western Australia. Ore Geology Reviews, 51, 79-92.

Grguric, B., Rosengren, N., Fletcher, C. and Hronsky, J. 2006. Type 2 deposits: Geology, mineralogy, and processing of the Mount Keith and Yakabindie orebodies, Western Australia. Special Publication-Society of Economic Geologists, 13, 119.

Grguric, B. 2003. Minerals of the MKD5 nickel deposit, Mount Keith, Western Australia. Australian Journal of Mineralogy, 9, 55-71.

Grguric, B. 2002. Hypogene violarite of exsolution origin from Mount Keith, Western Australia: field evidence for a stable pentlandite− violarite tie line: De Gruyter.

Grguric, B., Madsen, I. and Pring, A. 2001. Woodallite, a new chromium analogue of iowaite from the Mount Keith nickel deposit, Western Australia. Mineralogical Magazine, 65(3), 427-435.

Grey, I. and Li, C. 2003. Hydroxylian pseudorutile derived from picroilmenite in the Murray Basin, southeastern Australia. De Gruyter.

Grey, I., MacRae, C., Silvester, E. and Susini, J. 2005. Behaviour of impurity elements during the weathering of ilmenite. Mineralogical Magazine 69, 437-446.

Grey, I.E. and Reid, A.F. 1975. The structure of pseudorutile and its role in the natural alteration of ilmenite. American Mineralogist: Journal of Earth and Planetary Materials 60, 898-906.

Groves, D., Hudson, D. and Hack, T. 1974. Modification of iron-nickel sulfides during serpentinization and talc-carbonate alteration at Black Swan, Western Australia. Economic Geology, 69(8), 1265-1281.

Gueguin, M. and Cardarelli, F. 2007. Chemistry and mineralogy of titania-rich slags. Part 1—hemo-ilmenite, sulphate, and upgraded titania slags. Mineral Processing and Extractive Metallurgy Review 28, 1-58.

Habashi, F., Kamaleddine, F. and Bourricaudy, E. 2014. A New Process to upgrade ilmenite to synthetic rutile, Conference of Metallurgists Proceedings (COM 2014).

Hellmann, R., Wirth, R., Daval, D., Barnes, J.-P., Penisson, J.-M., Tisserand, D., Epicier, T., Florin, B. and Hervig, R.L. 2012. Unifying natural and laboratory chemical weathering with interfacial dissolution–reprecipitation: a study based on the nanometer-scale chemistry of fluid–silicate interfaces. Chemical Geology 294, 203-216.

Hövelmann, J., Austrheim, H., Beinlich, A., Anne Munz, I., 2011. Experimental study of the carbonation of partially serpentinized and weathered peridotites. Geochim. Cosmochim. Acta , 75(22): 6760-6779.

Huang, R., Lin, C.-T., Sun, W., Ding, X., Zhan, W. and Zhu, J. 2017a. The production of iron oxide during peridotite serpentinization: Influence of pyroxene. Geoscience Frontiers 8, 1311-1321.

Huang, R., Song, M., Ding, X., Zhu, S., Zhan, W. and Sun, W. 2017b. Influence of pyroxene and spinel on the kinetics of peridotite serpentinization. Journal of Geophysical Research: Solid Earth 122, 7111-7126.

Itoh, S., Sato, S., Ono, J., Okada, H. and Nagasaka, T. 2006. Feasibility study of the new rutile extraction process from natural ilmenite ore based on the oxidation reaction. Metallurgical and Materials Transactions B 37, 979-985.

Iyer, K., Austrheim, H., John, T. and Jamtveit, B. 2008. Serpentinization of the oceanic lithosphere and some geochemical consequences: constraints from the Leka Ophiolite Complex, Norway. Chemical Geology 249, 66-90.

James, R.H., Green, D.R., Stock, M.J., Alker, B.J., Banerjee, N.R., Cole, C., German, C.R., Huvenne, V.A., Powell, A.M. and Connelly, D.P., 2014. Composition of hydrothermal fluids and mineralogy of associated chimney material on the East Scotia Ridge back-arc spreading centre. Geochim. Cosmochim. Acta , 139: 47-71.

Jamtveit, B. and Hammer, Ø. 2012. Sculpting of rocks by reactive fluids. Geochemical Perspectives 1, 341-342.

Jamtveit, B., Putnis, C.V. and Malthe-Sørenssen, A. 2009. Reaction induced fracturing during replacement processes. Contributions to Mineralogy and Petrology 157, 127-133.

Jamtveit, B., Malthe-Sørenssen, A. and Kostenko, O. 2008. Reaction enhanced permeability during retrogressive metamorphism. Earth and Planetary Science Letters 267, 620-627.

Janecky, D., Seyfried Jr, W., 1986. Hydrothermal serpentinization of peridotite within the oceanic crust: experimental investigations of mineralogy and major element chemistry. Geochim. Cosmochim. Acta , 50(7): 1357-1378.

Janssen, A. and Putnis, A. 2011. Processes of oxidation and HCl-leaching of Tellnes ilmenite. Hydrometallurgy 109, 194-201.

Janssen, A., Putnis, A., Geisler, T. and Putnis, C. 2010. The experimental replacement of ilmenite by rutile in HCl solutions. Mineralogical Magazine 74, 633-644.

Jarosewich, E., Nelen, J.A., Norberg, J.A., 1980. Reference Samples for Electron Microprobe Analysis. Geostandards Newsletter, 4(1): 43-47.

Jena, B., Dresler, W. and Reilly, I. 1995. Extraction of titanium, vanadium and iron from titanomagnetite deposits at pipestone lake, Manitoba, Canada. Minerals engineering 8, 159-168.

Johnson, J.W., Oelkers, E.H., Helgeson, H.C., 1992. SUPCRT92: A software package for calculating the standard molal thermodynamic properties of minerals, gases, aqueous species, and reactions from 1 to 5000 bar and 0 to 1000 C. Computers & Geosciences, 18(7): 899-947.

Klein, F., McCollom, T.M., 2013. From serpentinization to carbonation: New insights from a CO_2 injection experiment. Earth Planet. Sci. Lett. , 379: 137-145.

Klein, F., Bach, W. and McCollom, T.M. 2013. Compositional controls on hydrogen generation during serpentinization of ultramafic rocks. Lithos 178, 55-69.

Klein, F. and Garrido, C.J. 2011. Thermodynamic constraints on mineral carbonation of serpentinized peridotite. Lithos 126, 147-160.

Klein, F. and Bach, W. 2009. Fe–Ni–Co–O–S phase relations in peridotite–seawater interactions. Journal of Petrology, 50(1), 37-59.

Klein, F., Bach, W., Jöns, N., McCollom, T., Moskowitz, B. and Berquó, T. 2009. Iron partitioning and hydrogen generation during serpentinization of abyssal peridotites from 15 N on the Mid-Atlantic Ridge. Geochimica et Cosmochimica Acta 73, 6868-6893.

Kletetschka, G., Wasilewski, P.J. and Taylor, P.T. 2002. The role of hematite–ilmenite solid solution in the production of magnetic anomalies in ground-and satellite-based data. Tectonophysics 347, 167-177.

Konnunaho, J., Hanski, E., Bekker, A., Halkoaho, T., Hiebert, R. and Wing, B. 2013. The Archean komatiite-hosted, PGE-bearing Ni–Cu sulfide deposit at Vaara, eastern Finland: evidence for assimilation of external sulfur and post-depositional desulfurization. Mineralium Deposita, 48(8), 967-989.

Kullerud, G. 1969. Phase relations in the Cu-Fe-S, Cu-Ni-S and Fe-Ni-S system. Magmatic ore deposits, 323-343.

Kullerud, G. and Yoder, H. S. 1959. Pyrite stability relations in the Fe-S system. Economic Geology, 54(4), 533-572.

Kullerud, G. and Yund, R. A. 1962. The Ni-S system and related minerals. Journal of Petrology, 3(1), 126-175.

Labotka, T.C., Cole, D.R., Fayek, M., Riciputi, L.R. and Stadermann, F.J. 2004. Coupled cation and oxygen-isotope exchange between alkali feldspar and aqueous chloride solution. American Mineralogist 89, 1822-1825.

Lafay, R., Fernandez-Martinez, A., Montes-Hernandez, G., Auzende, A.L., Poulain, A., 2016. Dissolution-reprecipitation and self-assembly of serpentine nanoparticles preceding chrysotile formation: Insights into the structure of proto-serpentine. Am. Mineral., 101(12): 2666-2676.

Lafay, R., Montes-Hernandez, G., Janots, E., Auzende, A.-L., Chiriac, R., Lemarchand, D. and Toche, F. 2014. Influence of trace elements on the textural properties of synthetic chrysotile: Complementary insights from macroscopic and nanoscopic measurements. Microporous and Mesoporous Materials 183, 81-90.

Lafay, R., Montes-Hernandez, G., Janots, E., Chiriac, R., Findling, N. and Toche, F. 2012. Mineral replacement rate of olivine by chrysotile and brucite under high alkaline conditions. Journal of Crystal Growth, 347(1), 62-72.

Lamadrid, H.M., Rimstidt, J.D., Schwarzenbach, E.M., Klein, F., Ulrich, S., Dolocan, A. and Bodnar, R.J. 2017. Effect of water activity on rates of serpentinization of olivine. Nature communications 8, 16107.

Lenting, C., Plümper, O., Kilburn, M., Guagliardo, P., Klinkenberg, M. and Geisler, T. 2018. Towards a unifying mechanistic model for silicate glass corrosion. npj Materials Degradation 2, 28.

Li, K., Pring, A., Etschmann, B., Macmillan, E., Ngothai, Y., O'Neill, B., Hooker, A., Mosselmans, F. and Brugger, J. 2015. Uranium scavenging during mineral replacement reactions. American Mineralogist 100, 1728-1735.

Mackey, T.S. 1994. Upgrading ilmenite into a high-grade synthetic rutile. Jom 46, 59-64.

Mahmoud, M., Afifi, A. and Ibrahim, I. 2004. Reductive leaching of ilmenite ore in hydrochloric acid for preparation of synthetic rutile. Hydrometallurgy 73, 99-109.

Malvoisin, B., Brantut, N. and Kaczmarek, M.-A. 2017. Control of serpentinisation rate by reaction-induced cracking. Earth and Planetary Science Letters 476, 143-152.

Malvoisin, B., Brunet, F., Carlut, J., Rouméjon, S., Cannat, M., 2012. Serpentinization of oceanic peridotites: 2. Kinetics and processes of San Carlos olivine hydrothermal alteration. J. Geophys. Res.: Solid Earth, 117(B4).

Marcaillou, C., Munoz, M., Vidal, O., Parra, T., Harfouche, M., 2011. Mineralogical evidence for H2 degassing during serpentinization at 300 C/300 bar. Earth Planet. Sci. Lett. , 303(3-4): 281-290.

Martin, B. and Fyfe, W. 1970. Some experimental and theoretical observations on the kinetics of hydration reactions with particular reference to serpentinization. Chemical geology 6, 185-202.

Mayhew, L.E., Ellison, E., McCollom, T., Trainor, T. and Templeton, A. 2013. Hydrogen generation from low-temperature water–rock reactions. Nature Geoscience 6, 478.

McCollom, T.M., Klein, F., Robbins, M., Moskowitz, B., Berquó, T.S., Jöns, N., Bach, W. and Templeton, A. 2016. Temperature trends for reaction rates, hydrogen generation, and partitioning of iron during experimental serpentinization of olivine. Geochimica et Cosmochimica Acta 181, 175-200.

McCollom, T.M. and Bach, W. 2009. Thermodynamic constraints on hydrogen generation during serpentinization of ultramafic rocks. Geochimica et Cosmochimica Acta 73, 856-875.

McEnroe, S.A., Robinson, P., Langenhorst, F., Frandsen, C., Terry, M.P. and Boffa Ballaran, T. 2007. Magnetization of exsolution intergrowths of hematite and ilmenite: Mineral chemistry, phase relations, and magnetic properties of hemo-ilmenite ores with micron-to nanometer-scale lamellae from Allard Lake, Quebec. Journal of Geophysical Research: Solid Earth 112.

McEnroe, S., Harrison, R., Robinson, P. and Langenhorst, F. 2002. Nanoscale haematite–ilmenite lamellae in massive ilmenite rock: an example of 'lamellar magnetism'with implications for planetary magnetic anomalies. Geophysical Journal International 151, 890-912.

Misra, K. and Fleet, M. 1973. The chemical compositions of synthetic and natural pentlandite assemblages. Economic Geology 68, 518-539.

Miyoshi, A., Kogiso, T., Ishikawa, N. and Mibe, K. 2014. Role of silica for the progress of serpentinization reactions: Constraints from successive changes in mineralogical textures of serpentinites from Iwanaidake ultramafic body, Japan. American Mineralogist 99, 1035-1044.

Moody, J. 1976. An experimental study on the serpentinization of iron-bearing olivines. The Canadian Mineralogist 14, 462-478.

Mora, C.I., Riciputi, L.R., Cole, D.R. and Walker, K.D. 2009. High-temperature hydrothermal alteration of the Boehls Butte anorthosite: origin of a bimodal plagioclase assemblage. Contributions to Mineralogy and Petrology 157, 781.

Mothersole, F.E., Evans, K. and Frost, B.R. 2017. Abyssal and hydrated mantle wedge serpentinised peridotites: a comparison of the 15°20′ N fracture zone and New Caledonia serpentinites. Contributions to Mineralogy and Petrology 172, 69.

Mücke, A. and Chaudhuri, J.B. 1991. The continuous alteration of ilmenite through pseudorutile to leucoxene. Ore geology reviews 6, 25-44.

Naldrett, A., Craig, J. and Kullerud, G. 1967. The central portion of the Fe-Ni-S system and its bearing on pentlandite exsolution in iron-nickel sulfide ores. Economic Geology 62, 826-847.

Nguyen, T.H. and Lee, M.S. 2019. A review on the recovery of titanium dioxide from Ilmenite ores by direct leaching technologies. Mineral Processing and Extractive Metallurgy Review 40, 231-247.

Niedermeier, D.R., Putnis, A., Geisler, T., Golla-Schindler, U. and Putnis, C.V. 2009. The mechanism of cation and oxygen isotope exchange in alkali feldspars under hydrothermal conditions. Contributions to Mineralogy and Petrology 157, 65.

Normand, C., Williams-Jones, A.E., Martin, R.F. and Vali, H. 2002. Hydrothermal alteration of olivine in a flow-through autoclave: Nucleation and growth of serpentine phases. American Mineralogist 87, 1699-1709.

Oelkers, E.H., Schott, J., 2001. An experimental study of enstatite dissolution rates as a function of pH, temperature, and aqueous Mg and Si concentration, and the mechanism of pyroxene/pyroxenoid dissolution. Geochim. Cosmochim. Acta , 65(8): 1219-1231.

O'Hanley, D.S. 1992. Solution to the volume problem in serpentinization. Geology 20, 705-708.

O'Hanley, D.S. and Wicks, F.J. 1995. Conditions of formation of lizardite, chrysotile and antigorite, Cassiar, British Columbia. The Canadian Mineralogist 33, 753-773.

Ohnishi, I. and Tomeoka, K. 2007. Hydrothermal alteration experiments of enstatite: implications for aqueous alteration of carbonaceous chondrites. Meteoritics & Planetary Science 42, 49-61.

Okamoto, A., Ogasawara, Y., Hirano, N., Tsushiya, N., 2013. Effect of silica transport on serpentinization in the Ol-Opx-H_2O system. Procedia Earth and Planetary Science, 7: 628-631.

Okamoto, A., Ogasawara, Y., Ogawa, Y. and Tsuchiya, N. 2011. Progress of hydration reactions in olivine–H_2O and orthopyroxenite–H_2O systems at 250 C and vapor-saturated pressure. Chemical geology 289, 245-255.

Olanipekun, E. 1999. A kinetic study of the leaching of a Nigerian ilmenite ore by hydrochloric acid. Hydrometallurgy 53, 1-10.

Olsen, A.A., Hausrath, E.M., Rimstidt, J.D., 2015. Forsterite dissolution rates in Mg-sulfate-rich Mars-analog brines and implications of the aqueous history of Mars. Journal of Geophysical Research: Planets, 120(3): 388-400.

Ogasawara, Y., Okamoto, A., Hirano, N., Tsuchiya, N., 2013. Coupled reactions and silica diffusion during serpentinization. Geochim. Cosmochim. Acta , 119: 212-230.

Otálora, F., García-Ruiz, J., 2014. Nucleation and growth of the Naica giant gypsum crystals. Chemical Society Reviews, 43(7): 2013-2026.

Oufi, O., Cannat, M. and Horen, H. 2002. Magnetic properties of variably

serpentinized abyssal peridotites. Journal of Geophysical Research: Solid Earth 107, EPM 3-1-EPM 3-19.

Oyanagi, R., Okamoto, A., Harigane, Y., Tsuchiya, N., 2018. Al-zoning of serpentine aggregates in mesh texture induced by metasomatic replacement reactions. Journal of Petrology.

Oyanagi, R., Okamoto, A., Hirano, N., Tsuchiya, N., 2015. Competitive hydration and dehydration at olivine–quartz boundary revealed by hydrothermal experiments: Implications for silica metasomatism at the crust–mantle boundary. Earth Planet. Sci. Lett. , 425: 44-54.

Pens, M., Andreani, M., Daniel, I., Perrillat, J.-P., Cardon, H., 2016. Contrasted effect of aluminum on the serpentinization rate of olivine and orthopyroxene under hydrothermal conditions. Chem. Geol., 441: 256-264.

Petriglieri, J. R., Salvioli-Mariani, E., Mantovani, L., Tribaudino, M., Lottici, P. P., Laporte-Magoni, C. and Bersani, D., 2015. Micro-Raman mapping of the polymorphs of serpentine. Journal of Raman Spectroscopy, 46(10): 953-958.

Phillips-Lander, C., Legett, C., Parnell, S., Elwood Madden, A., Elwood Madden, M., 2016. Pyroxene dissolution rates in high salinity brines: Implications for post-Noachian aqueous alteration on Mars, Lunar and Planetary Science Conference, pp. 1313.

Ping, T., Hu, H.-P. and Zhang, L. 2011. Effects of mechanical activation and oxidation-reduction on hydrochloric acid leaching of Panxi ilmenite concentration. Transactions of Nonferrous Metals Society of China 21, 1414-1421.

Plümper, O., King, H.E., Geisler, T., Liu, Y., Pabst, S., Savov, I.P., Rost, D. and Zack, T., 2017. Subduction zone forearc serpentinites as incubators for deep microbial life. Proceedings of the National Academy of Sciences.

Plümper, O., Beinlich, A., Bach, W., Janots, E., Austrheim, H., 2014. Garnets within geode-like serpentinite veins: Implications for element transport, hydrogen

production and life-supporting environment formation. Geochim. Cosmochim. Acta , 141: 454-471.

Plümper, O., Røyne, A., Magrasó, A. and Jamtveit, B. 2012. The interface-scale mechanism of reaction-induced fracturing during serpentinization. Geology 40, 1103-1106.

Pochon, A., Beaudoin, G., Branquet, Y., Boulvais, P., Gloaguen, E. and Gapais, D. 2017. Metal mobility during hydrothermal breakdown of Fe-Ti oxides: insights from Sb-Au mineralizing event (Variscan Armorican Massif, France). Ore Geology Reviews 91, 66-99.

Pokrovsky, O.S., Schott, J., 2000. Kinetics and mechanism of forsterite dissolution at 25 C and pH from 1 to 12. Geochim. Cosmochim. Acta , 64(19): 3313-3325.

Pownceby, M. 2010. Alteration and associated impurity element enrichment in detrital ilmenites from the Murray Basin, southeast Australia: a product of multistage alteration. Australian Journal of Earth Sciences 57, 243-258.

Power, I.M., Wilson, S.A. and Dipple, G.M. 2013. Serpentinite carbonation for CO_2 sequestration. Elements 9, 115-121.

Putnis, A. 2015. Transient porosity resulting from fluid–mineral interaction and its consequences. Reviews in Mineralogy and Geochemistry 80, 1-23.

Putnis, C.V. and Ruiz-Agudo, E. 2013. The mineral–water interface: where minerals react with the environment. Elements 9, 177-182.

Putnis, A. 2009. Mineral replacement reactions. Reviews in mineralogy and geochemistry 70, 87-124.

Putnis, A., Hinrichs, R., Putnis, C.V., Golla-Schindler, U. and Collins, L.G. 2007. Hematite in porous red-clouded feldspars: evidence of large-scale crustal fluid–rock interaction. Lithos 95, 10-18.

Putnis, C.V., Geisler, T., Schmid-Beurmann, P., Stephan, T. and Giampaolo, C. 2007. An experimental study of the replacement of leucite by analcime. American Mineralogist 92, 19-26.

Putnis, A. and Putnis, C.V. 2007. The mechanism of reequilibration of solids in the presence of a fluid phase. Journal of Solid State Chemistry 180, 1783-1786.

Putnis, C.V., Tsukamoto, K. and Nishimura, Y. 2005. Direct observations of pseudomorphism: compositional and textural evolution at a fluid-solid interface. American Mineralogist 90, 1909-1912.

Putnis, A. 2002. Mineral replacement reactions: from macroscopic observations to microscopic mechanisms. Mineralogical Magazine 66, 689-708.

Qian, G., Xia, F., Brugger, J., Skinner, W. M., Bei, J., Chen, G. and Pring, A. 2011. Replacement of pyrrhotite by pyrite and marcasite under hydrothermal conditions up to 220 C: An experimental study of reaction textures and mechanisms. American Mineralogist, 96(11-12), 1878-1893.

Qian, G., Brugger, J., Skinner, W.M., Chen, G. and Pring, A. 2010. An experimental study of the mechanism of the replacement of magnetite by pyrite up to 300 C. Geochimica et Cosmochimica Acta 74, 5610-5630.

Rosengren, N., Grguric, B., Beresford, S., Fiorentini, M. and Cas, R. 2007. Internal stratigraphic architecture of the komatiitic dunite-hosted MKD5 disseminated nickel sulfide deposit, Mount Keith Domain, Agnew-Wiluna greenstone belt, Western Australia. Mineralium Deposita, 42(8), 821-845.

Roy, D.M., Roy, R., 1954. An experimental study of the formation and properties of synthetic serpentines and related layer silicate minerals. Am. Mineral., 39(11-1): 957-975.

Ruiz-Agudo, E., Putnis, C. and Putnis, A. 2014. Coupled dissolution and precipitation at mineral–fluid interfaces. Chemical geology, 383, 132-146.

Ruiz-Agudo, E., King, H.E., Patiño-López, L.D., Putnis, C.V., Geisler, T., Rodriguez-Navarro, C. and Putnis, A. 2016. Control of silicate weathering by interface-coupled dissolution-precipitation processes at the mineral-solution interface. Geology 44, 567-570.

Rüpke, L.H., Morgan, J.P., Hort, M., Connolly, J.A., 2004. Serpentine and the subduction zone water cycle. Earth Planet. Sci. Lett. , 223(1-2): 17-34.

Russell, M.J. and Hall, A. 1997. The emergence of life from iron monosulphide bubbles at a submarine hydrothermal redox and pH front. Journal of the Geological Society 154, 377-402.

Schmidt, O.G., Eberl, K., 2001. Nanotechnology: Thin solid films roll up into nanotubes. Nature, 410(6825): 168.

Schroeder, P.A., Le Golvan, J.J. and Roden, M.F. 2002. Weathering of ilmenite from granite and chlorite schist in the Georgia Piedmont. American Mineralogist 87, 1616-1625.

Schwarzenbach, E.M., Caddick, M.J., Beard, J.S. and Bodnar, R.J. 2016. Serpentinization, element transfer, and the progressive development of zoning in veins: evidence from a partially serpentinized harzburgite. Contributions to Mineralogy and Petrology 171, 5.

Sciortino, M., Mungall, J. E. and Muinonen, J. 2015. Generation of High-Ni sulfide and alloy phases during serpentinization of dunite in the Dumont sill, Quebec. Economic Geology, 110(3), 733-761.

Seyfried Jr, W., Foustoukos, D., Fu, Q., 2007. Redox evolution and mass transfer during serpentinization: An experimental and theoretical study at 200 C, 500 bar with implications for ultramafic-hosted hydrothermal systems at Mid-Ocean Ridges. Geochim. Cosmochim. Acta , 71(15): 3872-3886.

Sleep, N., Meibom, A., Fridriksson, T., Coleman, R. and Bird, D. 2004. H2-rich fluids from serpentinization: geochemical and biotic implications. Proceedings of the National Academy of Sciences 101, 12818-12823.

Stanaway, K. 1994. Overview of titanium dioxide feedstocks. Mining engineering 46, 1367-1370.

Stueber, A., Huang, W. and Johns, W. 1968. Chlorine and fluorine abundances in ultramafic rocks. Geochimica et Cosmochimica Acta, 32(3), 353-358.

Sunagawa, I., 1999. Growth and morphology of crystals. FORMA-TOKYO-, 14(1/2): 147-166.

Syverson, D.D., Tutolo, B.M., Borrok, D.M. and Seyfried Jr, W.E. 2017. Serpentinization of olivine at 300° C and 500 bars: an experimental study examining the role of silica on the reaction path and oxidation state of iron. Chemical Geology 475, 122-134.

Temple, A.K. 1966. Alteration of ilmenite. Economic Geology 61, 695-714.

Tenailleau, C., Pring, A., Etschmann, B., Brugger, J., Grguric, B. and Putnis, A. 2006. Transformation of pentlandite to violarite under mild hydrothermal conditions. American Mineralogist 91, 706-709.

Tominaga, M., Beinlich, A., Lima, E. A., Tivey, M. A., Hampton, B. A., Weiss, B. and Harigane, Y., 2017. Multi-scale magnetic mapping of serpentinite carbonation. Nat. Commun., 8(1): 1870.

Ulven, O.I., Beinlich, A., Hövelmann, J., Austrheim, H., Jamtveit, B., 2017. Subarctic physicochemical weathering of serpentinized peridotite. Earth Planet. Sci. Lett. , 468: 11-26.

Van Dyk, J.P., Vegter, N.M. and Pistorius, P.C. 2002. Kinetics of ilmenite dissolution in hydrochloric acid. Hydrometallurgy 65, 31-36.

Van Noort, R., Spiers, C., Drury, M., Kandianis, M., 2013. Peridotite dissolution and carbonation rates at fracture surfaces under conditions relevant for in situ mineralization of CO_2. Geochim. Cosmochim. Acta , 106: 1-24.

Wang, A., Freeman, J.J., Jolliff, B.L., 2015. Understanding the Raman spectral features of phyllosilicates. Journal of Raman Spectroscopy, 46(10): 829-845.

Wegner, W.W., Ernst, W., 1983. Experimentally determined hydration and dehydration reaction rates in the system MgO-SiO_2-H_2O. Amer. J. Sci., 283: 151-180.

Whitney, D.L., Evans, B.W., 2010. Abbreviations for names of rock-forming minerals. Am. Mineral., 95(1): 185-187.

Xia, F., Brugger, J., Chen, G., Ngothai, Y., O'Neill, B., Putnis, A. and Pring, A. 2009. Mechanism and kinetics of pseudomorphic mineral replacement reactions: A case study of the replacement of pentlandite by violarite. Geochimica et Cosmochimica Acta, 73(7), 1945-1969.

Xia, F., Zhou, J., Brugger, J., Ngothai, Y., O'Neill, B., Chen, G. and Pring, A. 2008. Novel route to synthesize complex metal sulfides: Hydrothermal coupled dissolution− reprecipitation replacement reactions. Chemistry of Materials 20, 2809-2817.

Xia, F., Zhou, J., Pring, A., Ngothai, Y., O'Neill, B., Brugger, J., Chen, G. and Colby, C. 2007. The role of pyrrhotite (Fe 7 S 8) and the sample texture in the hydrothermal transformation of pentlandite ((Fe, Ni) 9 S 8) to violarite ((Ni, Fe) 3 S 4). Reaction Kinetics and Catalysis Letters 92, 257-266.

Yada, K., Iishi, K., 1974. Serpentine minerals hydrothermally synthesized and their microstructures. Journal of Crystal Growth, 24: 627-630.

Yada, K., & Iishi, K. 1977. Growth and microstructure of synthetic chrysotile. American Mineralogist, 62(9-10), 958-965.

Zhao, J. and Pring, A. 2019. Mineral Transformations in Gold–(Silver) Tellurides in the Presence of Fluids: Nature and Experiment. Minerals 9, 167.

Zhao, J., Brugger, J. and Pring, A. 2019. Mechanism and kinetics of hydrothermal replacement of magnetite by hematite. Geoscience Frontiers 10, 29-41.

Zhao, J., Brugger, J., Ngothai, Y. and Pring, A. 2014. The replacement of chalcopyrite by bornite under hydrothermal conditions. American Mineralogist 99, 2389-2397.

Zhao, J., Brugger, J., Xia, F., Ngothai, Y., Chen, G. and Pring, A. 2013. Dissolution-reprecipitation vs. solid-state diffusion: Mechanism of mineral transformations in sylvanite,(AuAg) 2Te4, under hydrothermal conditions. American Mineralogist 98, 19-32.

Zhang, L., Hu, H., Wei, L., Chen, Q. and Tan, J. 2010. Hydrochloric acid leaching behaviour of mechanically activated Panxi ilmenite (FeTiO3). Separation and Purification Technology 73, 173-178.

Zhang, L., Li, G.-Q. and Zhang, W. 2011. Synthesis of rutile from high titania slag by pyrometallurgical route. Transactions of Nonferrous Metals Society of China 21, 2317-2322.

Zega, T. J., Garvie, L. A., Dódony, I., Friedrich, H., Stroud, R. M. and Buseck, P. R.., 2006. Polyhedral serpentine grains in CM chondrites. Meteoritics & Planetary Science, 41(5): 681-688.

Appendix

Statement of authorship

Chapter 2

To whom it may concern,

By signing the statement of authorship, each author confirms the stated contribution to the manuscript.

Manuscript title: Fluid compositional control on serpentinisation kinetics and textural evolution				
Author	T. Wengorsch	A. Beinlich	A. Putnis	B. Grguric
Contribution %	70	15	10	5
Date	25.09.2019	24-09-2019	24.09.2019	19-9-2019
Signature				

Chapter 3

To whom it may concern,

By signing the statement of authorship, each author confirms the stated contribution to the manuscript.

Manuscript title: Experimental Ni-tenor modification of Fe-Ni-sulphides through hydrothermal alteration				
Author	T. Wengorsch	A. Beinlich	A. Putnis	B. Grguric
Contribution %	75	10	5	10
Date	25.09.2019	24-09-2019	24.09.2019	19-9-2019
Signature				

Chapter 4

To whom it may concern,

By signing the statement of authorship, each author confirms the stated contribution to the manuscript.

Manuscript title: Effect of hematite on the textural evolution during the replacement of ilmenite by rutile			
Author	T. Wengorsch	A. Beinlich	A. Putnis
Contribution %	80	10	10
Date	25.09.2019	24-09-2019	24.09.2019
Signature			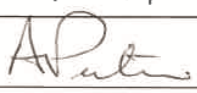

Thermogravimetric data

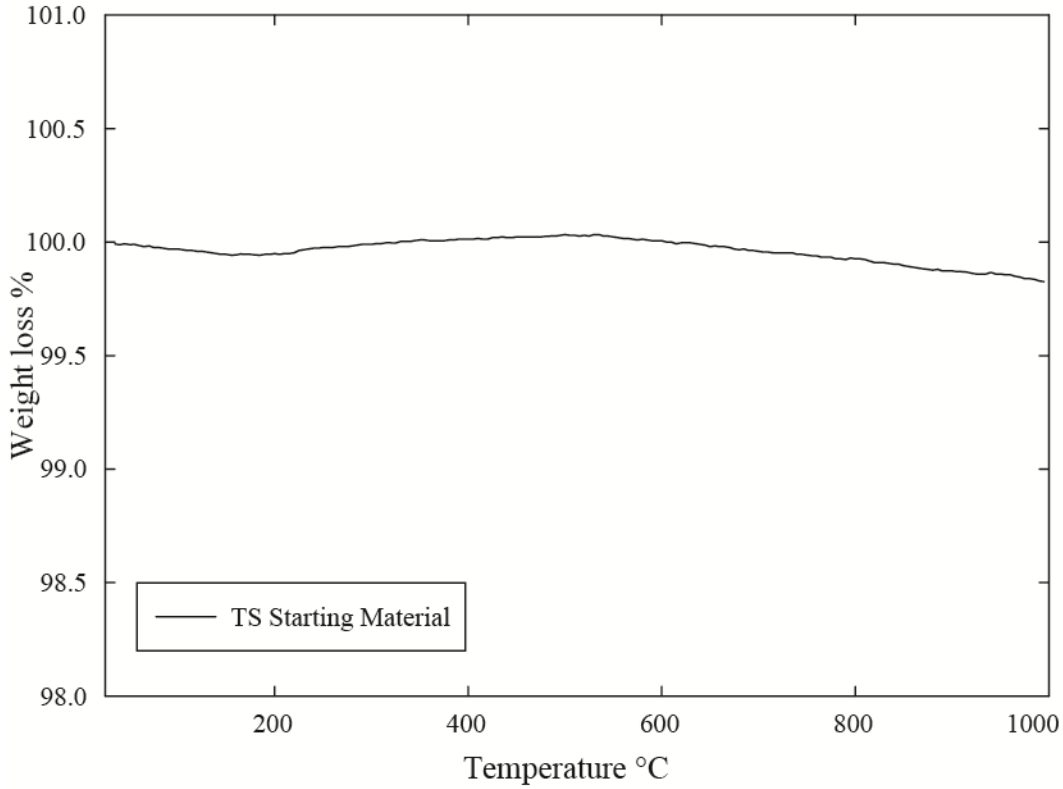

Appendix Figure 1 (Chapter 2): TG profile for Twin Sisters Starting material.

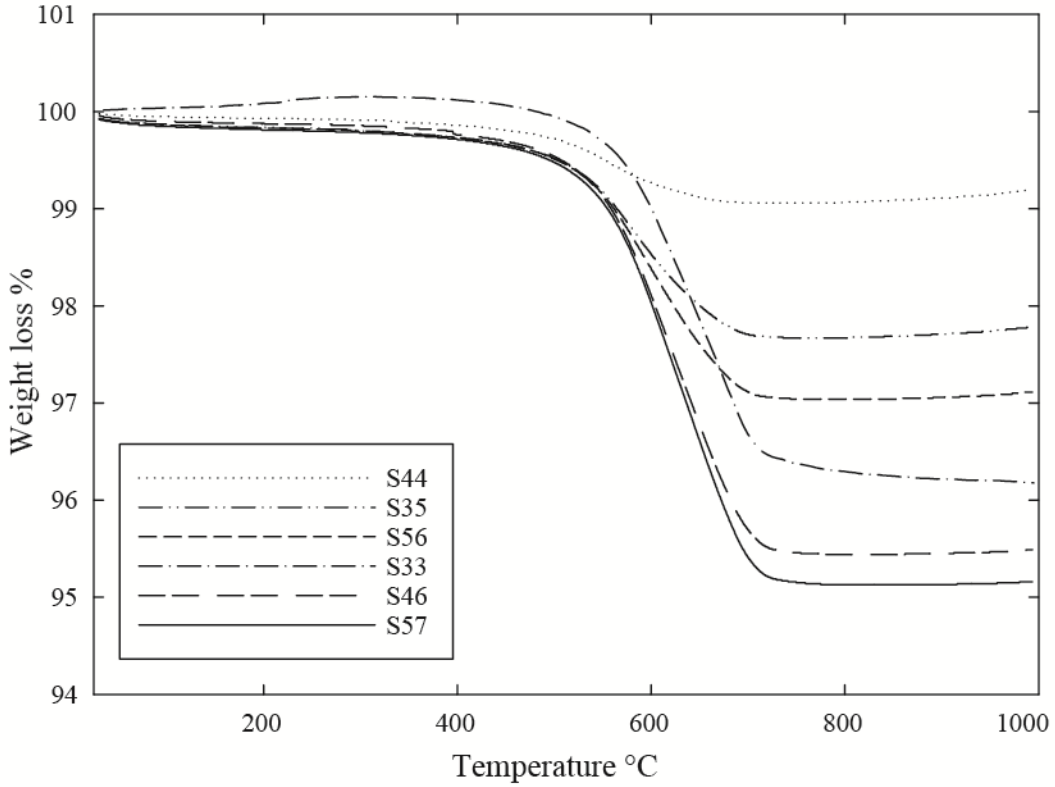

Appendix Figure 2 (Chapter 2): TG profiles for experiments on Twin Sisters harzburgite in NaCl-free fluid.

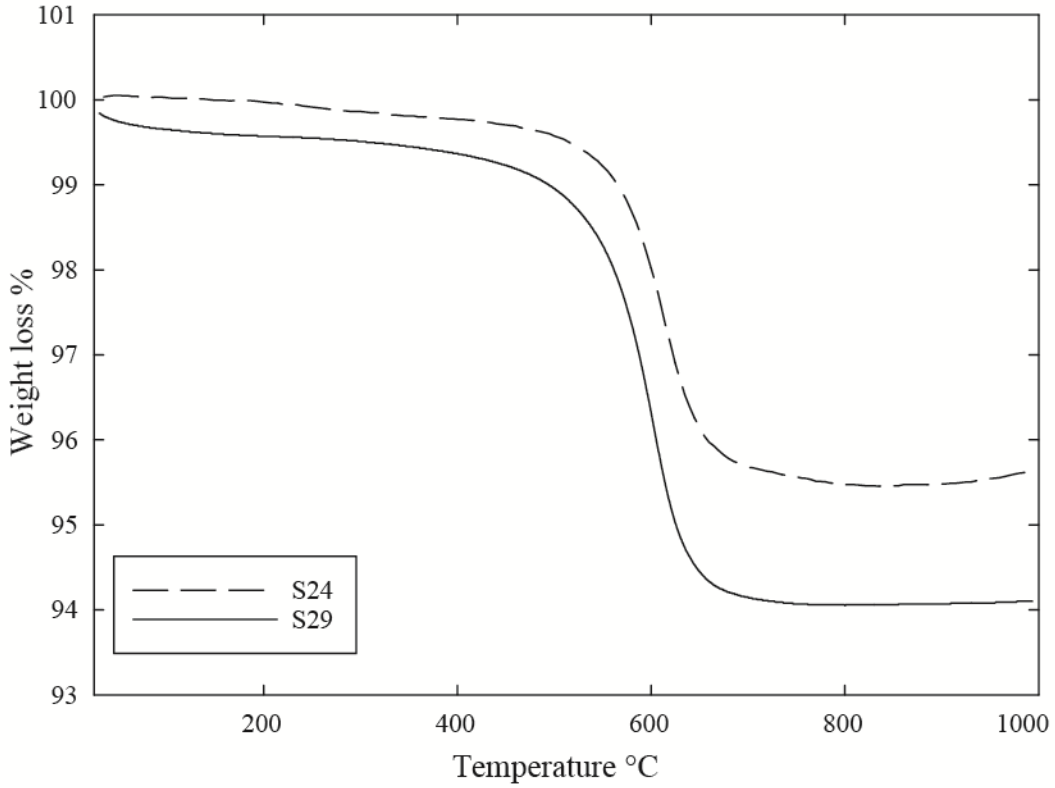

Appendix Figure 3 (Chapter 2): TG profiles for experiments on Twin Sisters harzburgite with 0.3 M NaCl starting solution.

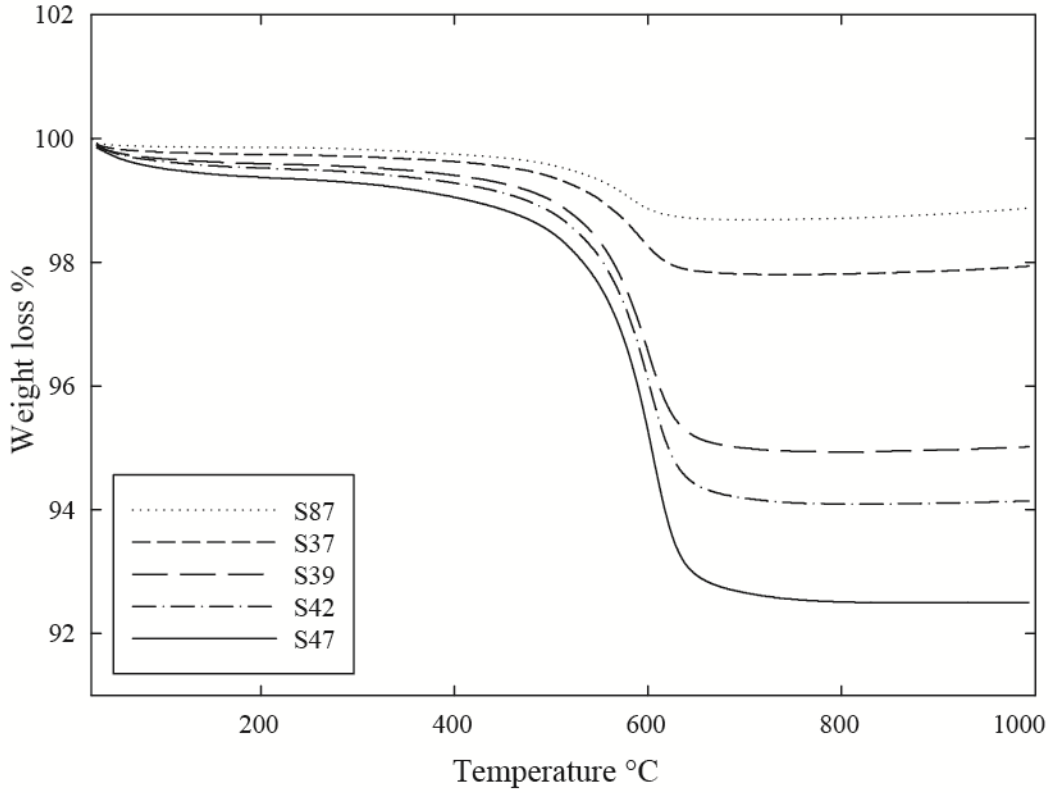

Appendix Figure 4 (Chapter 2): TG profiles for experiments on Twin Sisters harzburgite with 0.6 M NaCl starting solution.

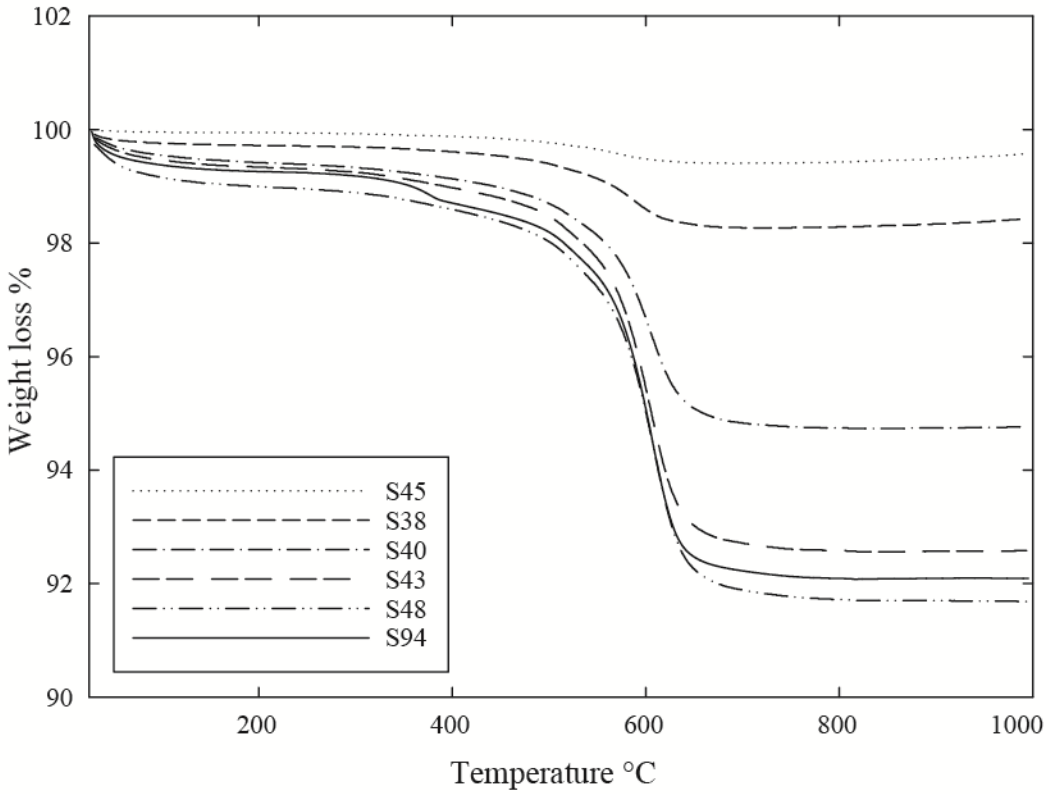

Appendix Figure 5 (Chapter 2): TG profiles for experiments on Twin Sisters harzburgite with 0.6 M NaCl starting solution.

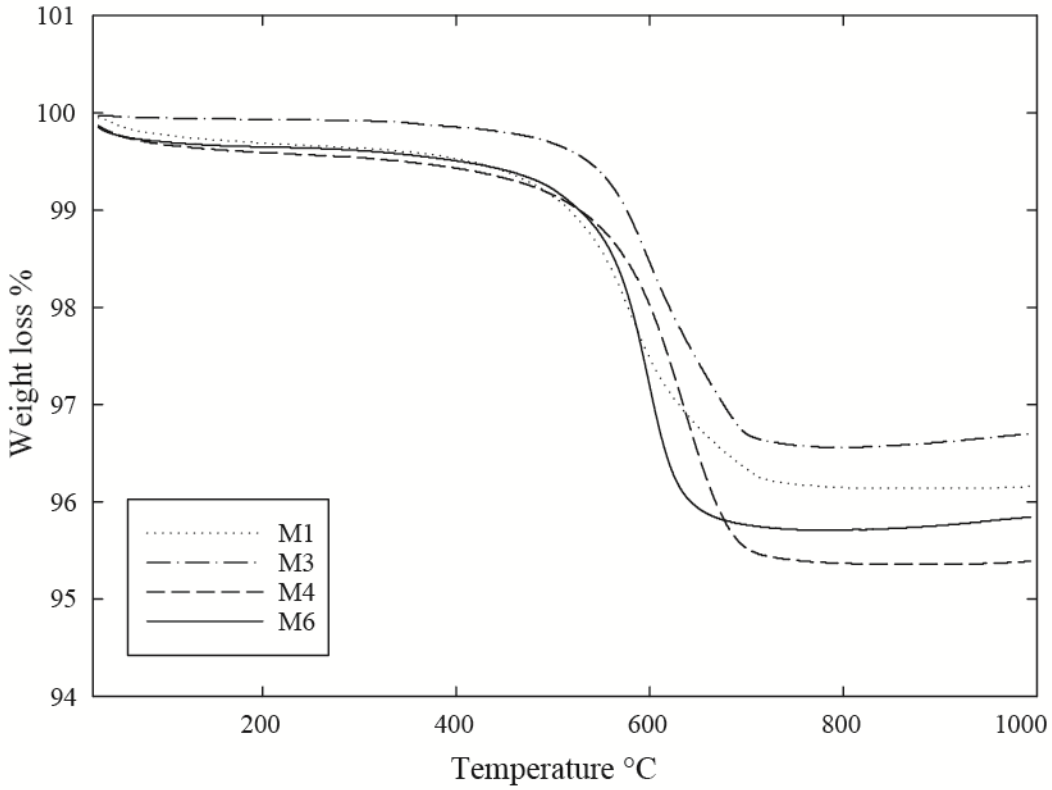

Appendix Figure 6 (Chapter 2): TG profiles for experiments on mixtures of San Carlos olivine and Enstatite (En).

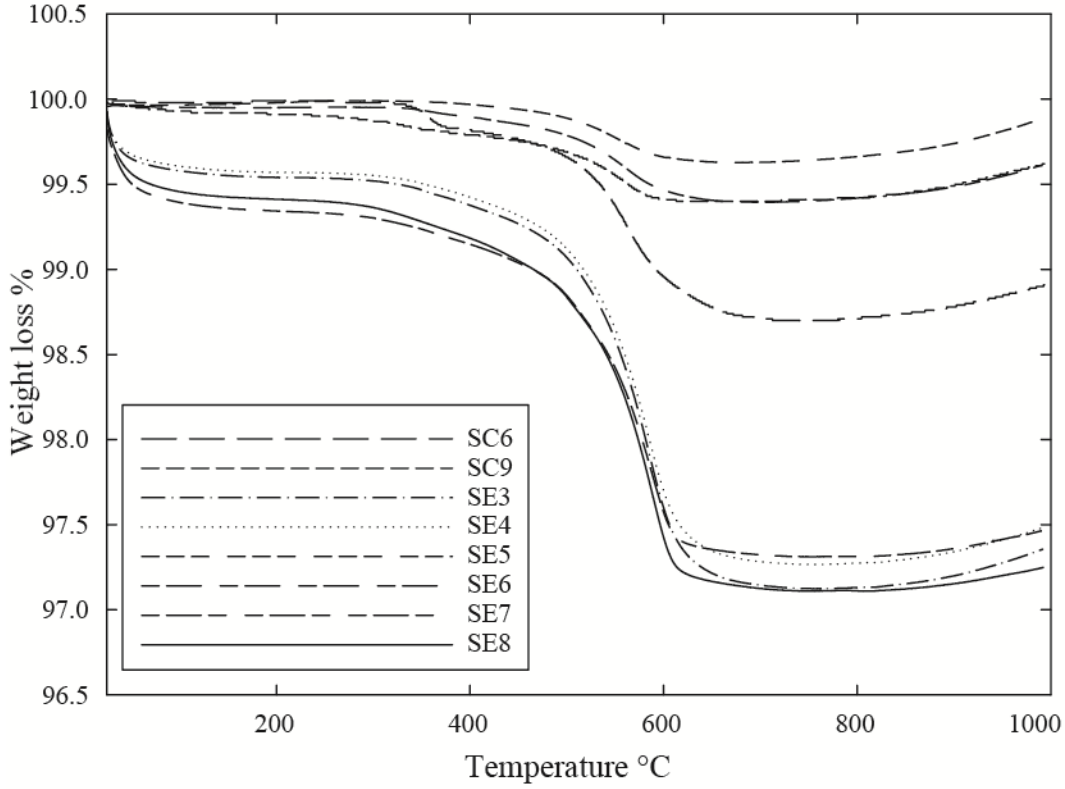

Appendix Figure 7 (Chapter 2): TG profiles for experiments on San Carlos olivine in different solutions.